

# CANADIAN JOURNAL OF RESEARCH

VOLUME 26

JULY, 1948

NUMBER 4

## — SECTION A —

### PHYSICAL SCIENCES

#### *Contents*

	Page
Studies in High Frequency Discharges— <i>J. I. Lodge and R. W. Stewart</i> - - - - -	205
A Method for the Determination of the Index of Refraction of Thin Transparent Films— <i>R. W. Stewart</i> - - - - -	230
A Comparison of the X-ray Diffraction and Nitrogen Adsorption Surface Areas of Carbon Blacks and Charcoals— <i>J. C. Arnell and W. M. Barss</i> - - - - -	236
Measurement of the Energies of $\alpha$ -Particles— <i>T. E. Cranshaw and J. A. Harcey</i> - - - - -	243
Measurement of the Half-period of Polonium 213— <i>J. V. Jelley</i>	255
Heat Transfer with Surface Boiling— <i>J. W. Knowles</i> - - -	268

NATIONAL RESEARCH COUNCIL  
OTTAWA, CANADA

## CANADIAN JOURNAL OF RESEARCH

The *Canadian Journal of Research* is issued in six sections, as follows:

- |                       |                        |
|-----------------------|------------------------|
| A. Physical Sciences  | D. Zoological Sciences |
| B. Chemical Sciences  | E. Medical Sciences    |
| C. Botanical Sciences | F. Technology          |

For the present, Sections A, C, D, and E are to be issued six times annually, and Sections B and F, twelve times annually, each section under separate cover, with separate pagination.

The *Canadian Journal of Research* is published by the National Research Council of Canada under authority of the Chairman of the Committee of the Privy Council on Scientific and Industrial Research. The *Canadian Journal of Research* is edited by a joint Editorial Board consisting of members of the National Research Council of Canada, the Royal Society of Canada, and the Chemical Institute of Canada.

Sections B and F of the *Canadian Journal of Research* have been chosen by the Chemical Institute of Canada as its medium of publication for scientific papers.

### EDITORIAL BOARD

<i>Representing</i>	<i>Representing</i>	
NATIONAL RESEARCH COUNCIL	ROYAL SOCIETY OF CANADA	
DR. A. R. GORDON, ( <i>Chairman</i> ), Head, Department of Chemistry, University of Toronto, Toronto.	DR. A. NORMAN SHAW, Chairman, Department of Physics, McGill University, Montreal.	} Section III
DR. C. H. BEST, The Banting and Best Department of Medical Research, University of Toronto, Toronto.	DR. J. W. T. SPINKS, Department of Chemistry, University of Saskatchewan Saskatoon.	}
DR. ROBERT NEWTON, President, University of Alberta, Edmonton.	DR. H. S. JACKSON, Head, Department of Botany, University of Toronto, Toronto.	} Section V
DR. G. H. HENDERSON, Professor of Mathematical Physics, Dalhousie University, Halifax.	DR. E. HORNE CRAIGIE, Department of Zoology, University of Toronto, Toronto.	}
<i>Ex officio</i>	<i>Representing</i>	
DR. LÉO MARION, Editor-in-Chief, Division of Chemistry, National Research Laboratories, Ottawa.	THE CHEMICAL INSTITUTE OF CANADA DR. R. V. V. NICHOLLS, Associate Professor of Chemistry, McGill University, Montreal.	
DR. H. H. SAUNDERSON, Director, Division of Information Services, National Research Laboratories, Ottawa.		

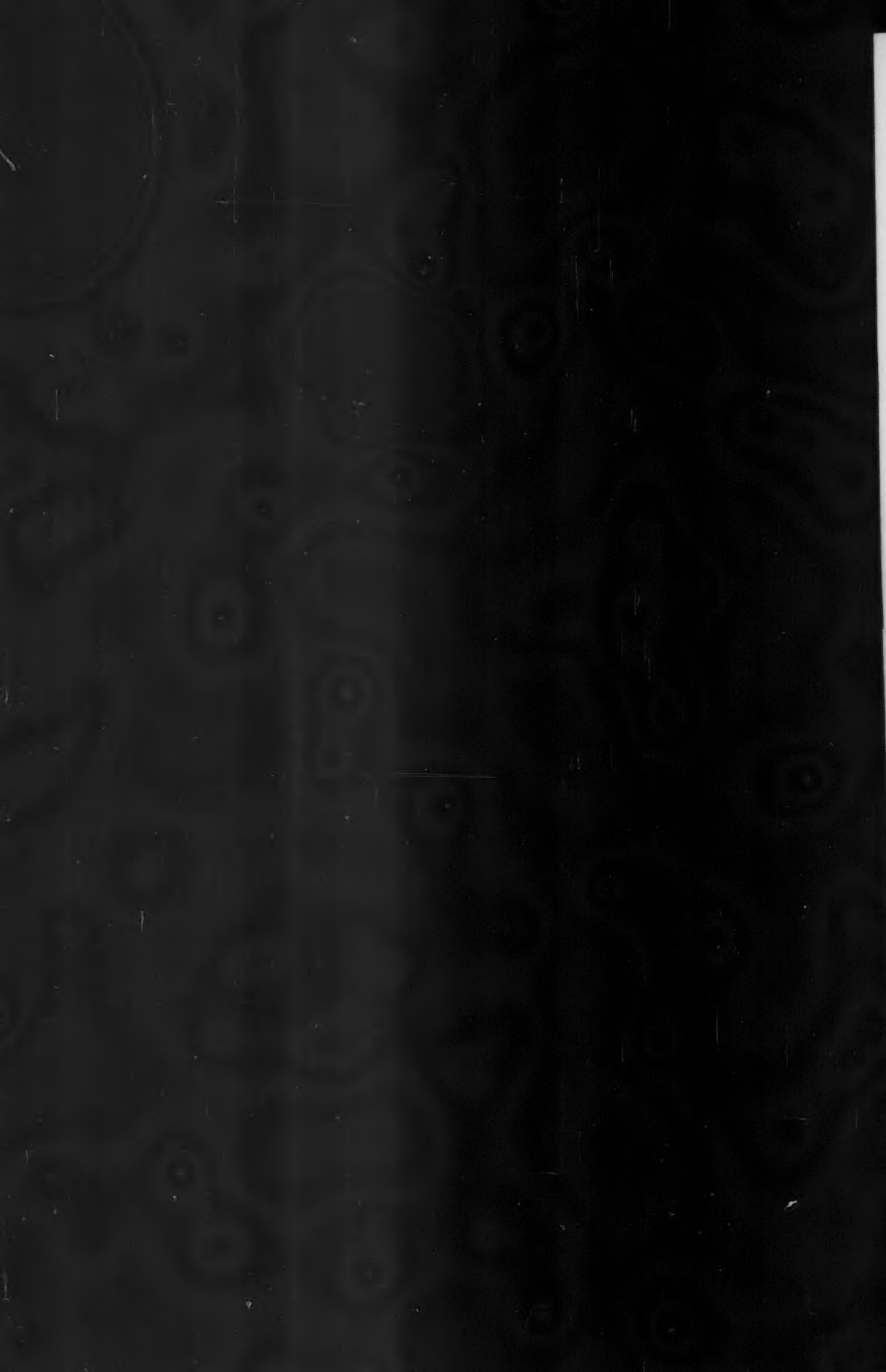
### EDITORIAL COMMITTEE

Editor-in-Chief,	DR. LÉO MARION	Editor, Section D,	DR. E. HORNE CRAIGIE
Editor, Section A,	DR. A. NORMAN SHAW	Editor, Section E,	DR. J. B. COLLIP
Editor, Section B,	DR. J. W. T. SPINKS	Editor, Section F,	DR. J. A. ANDERSON
Editor, Section C,	DR. R. V. V. NICHOLLS		DR. R. V. V. NICHOLLS
	DR. H. S. JACKSON		DR. A. NORMAN SHAW

Manuscripts should be addressed:

*Editor-in-Chief,  
Canadian Journal of Research,  
National Research Council, Ottawa, Canada.*







# Canadian Journal of Research

Issued by THE NATIONAL RESEARCH COUNCIL OF CANADA

VOL. 26, SEC. A.

JULY, 1948

NUMBER 4

## STUDIES IN HIGH FREQUENCY DISCHARGES<sup>1</sup>

BY J. I. LODGE AND R. W. STEWART<sup>2</sup>

### Abstract

A qualitative theory of the nature of high frequency discharges, with special reference to those developed by the use of external sleeve electrodes, is advanced on the assumption that the discharge is largely determined by its d-c. wall and space charges, and that the chief function of the high frequency field is to maintain the electron temperature. This theory leads to the conclusion that there must be a high negative wall charge under the electrodes, and a high radial field tending to drive positive ions to the walls. Thus each electrode has many of the characteristics of a cathode in a d-c. discharge. This conclusion is verified by the appearance of the high frequency discharge and by a careful examination of deposits resulting from the removal; by positive ion bombardment of the tube wall, of thin metallic films and of materials of which the discharge tube itself is composed.

### Introduction

The marked effects of high frequency discharges in rarefied gases on the walls of discharge tubes have been observed by a number of workers. In 1933 Robertson and Clapp (8) discovered that a coating on the tube walls, formed previously by a pure electrodeless discharge (arrangement as in Fig. 1, *a*), was removed by a discharge maintained with external electrodes (as in Fig. 1, *b*), even though the deposit had resisted heat from a gas-oxygen flame. The removal occurred directly under the electrodes, and by moving the electrodes from place to place the entire tube was cleaned. Robertson and Clapp also found that when a clear tube, previously operated with external electrodes, was subsequently silvered by the Brashear process, a pattern in the silver was observable at the places where the electrodes had been.

About the same time, Banerji, Bhattacharya, and Ganguli (1, 2) discovered that various metallic and nonmetallic vapors were deposited by the action of a high frequency discharge with external electrodes, the deposit occurring in distinct regions which they associated with changes in the radial and transverse fields.

In 1938, Hay (4) made an extensive study of the removal and deposit of silver coatings by discharges obtained with external electrodes, using various gases, pressures, and frequencies. He found that the removal was of two types: "electrode effect", a strong removal directly under the electrodes, and

<sup>1</sup> Manuscript received January 28, 1948.

Submitted by Prof. J. K. Robertson, Queen's University, Kingston, Ont.

<sup>2</sup> Holder of a Studentship under the National Research Council of Canada, 1946-47. Now, research student at the Cavendish Laboratory, Cambridge, England.

a "general removal", a much less marked effect opposite the various glows in the discharge. The silver was found to deposit in very sharply defined regions, with the deposits often showing marked fine structure.

Hay ascribed the electrode effect to positive ion bombardment, and gave evidence that the removal was associated with plasmas in the discharge. Since removal by positive ion bombardment suggests that the effect is not unrelated to the phenomenon of sputtering in a d-c. discharge, it was thought desirable to look for further evidence of this relation by extending Hay's work, using metals other than silver. Initially, the work done by one of us (R.W.S.) was undertaken with this object in view.

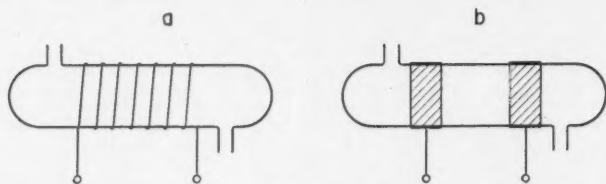


FIG. 1. Two arrangements for exciting high frequency discharges: (a) electrodeless method; (b) external electrodes.

When this work was under way, the other author (J. I. L.) was studying another aspect of the general problem of high frequency discharges. As both these investigations progressed, each of us observed a type of deposit that showed a marked interference pattern. As a careful examination of this deposit seemed likely to reveal interesting information concerning its nature and origin, as well as to shed further light on the complicated question of high frequency discharges, attention was shifted to a somewhat careful examination of this particular phenomenon.

At the same time, each of us, working independently, was able to make a preliminary comparison of conditions near an electrode in a high frequency discharge with those at the cathode in a d-c. discharge.

### Experimental

The discharge was obtained in a tube around which, for the most part, two external electrodes were wrapped, as in Fig. 1, *b*. The high frequency power was developed by a series-fed Hartley oscillator, using an Eimac 250 TH tube supplied by a bridge type power supply, with variac control and with 866A mercury vapor rectifier tubes. The oscillator supplied up to 1000 w. at a frequency of about 6 Mc. per sec. A rotary switch and relay arrangement permitted the oscillator to be run intermittently.

Discharge tubes were mostly of Pyrex glass with an inside diameter of about 2.5 cm., although some tubes of larger diameter were used. Some experiments were conducted using quartz and polystyrene tubing.

In all cases, a Cenco Hyvac pump was employed to evacuate the discharge tube, and the pressure was controlled by means of a needle valve.

Thin glass strips, of dimensions about 15 cm. by 6 mm. by 0.5 mm., were coated by evaporation with semitransparent layers of silver, copper, aluminum, gold, and bismuth. The evaporation was carried out *in vacuo*, using the techniques described by Strong (11) and by Olsen, Smith, and Crittenden (7). A coated strip was placed in the bottom of the tube and an air discharge was then maintained in the tube. In all cases, removal similar to that found by Hay (4) was observed, although with some metals, notably aluminum, the removal was very slow. Fig. 2 is a contact print of a series of gold-coated strips left in the discharge for varying lengths of time. It will be noted that the removal occurs under the electrode and that outside the region of the electrode deposits have formed in sharply defined areas.

It was found that the relative rates of removal of various metals correspond roughly with sputtering rates as recorded in the literature, but since the pressures employed, from 0.05 to 1.5 mm. of mercury, were well above those normally used for sputtering, an exact comparison is hardly justified with the present data. It is hoped to continue this problem in the future.

#### DEPOSITS SHOWING INTERFERENCE PATTERNS

After runs of an hour or more, it was found that a transparent deposit showing thin film interference fringes formed on the part of the strip under an electrode. Fig. 3 is a photograph, taken in reflected sodium light, of such a strip. Close examination of the tube walls revealed that a similar deposit had formed on the inner walls of the tube, just beyond the boundaries of the electrodes. Fig. 4 is a photograph of a well developed deposit on the walls.

In addition to the film giving rise to the interference pattern, a narrow ringlike deposit of a different kind was observed on each side of the electrodes, about 2 mm. from them. This was composed of a grayish-white flaky substance. If an electrode was loose fitting at some point, this deposit and the interference film were formed on the tube walls underneath the loose region.

#### Temperature Control

In order to test whether or not the deposit showing interference fringes was due to evaporation arising from local heating, some observations were made with the electrodes and adjacent parts of the tube packed with dry ice. It was found that, although the interference pattern was not as well developed when dry ice was used as without it, the pattern persisted. Fig. 5 shows the patterns: (a) without dry ice, and (b) with dry ice. It would seem, therefore, that the fundamental cause of the formation of the deposits is not a thermal one, although further work on this point is desirable.

#### Effect of Pressure

The original deposits giving rise to the interference patterns were obtained at pressures of approximately 0.5 mm. In order to investigate the effect of

pressure, glass strips were exposed to the discharge at pressures of about 2 and 0.01 mm. At the higher pressure, the pattern obtained was much the same as that at 0.5 mm., except that it was confined to a smaller region, and the films on the tube walls were deposited a little closer to the electrodes. In the case of the lower pressure, the interference fringes showed an oval pattern for that part of the strip that was under the electrodes, and the deposits on the tube were formed at a greater distance from the electrodes. Fig. 6 is a photograph of the oval interference pattern observed on the strip.

#### *Influence of Carrier Gas*

In order to eliminate the possibility of vapors getting into the discharge from the pump, a tube containing a *clear* glass strip was evacuated to a pressure of about 2 mm. of mercury, and sealed off. As the discharge ran, the pressure gradually dropped, owing to occlusion of the gas, until a discharge could no longer be maintained, but, owing to the initial high pressure, the strip was subjected to the discharge for a time great enough to give a pattern. Similar results were obtained with a sealed-off tube containing helium.

A trickle of hydrogen was allowed to pass into the discharge tube, the pressure being maintained at a constant value by means of a needle valve. In this case, a deposit formed on those portions of the strip under the electrodes, but an interference pattern could not be observed. A second run of much longer duration resulted in a similar deposit, which showed a little color at the edges when viewed with reflected white light. The deposit was quite thin and had a highly reflecting surface. In transmitted light it appeared brown.

#### *Chemical Tests*

An attempt was made to clean one of the Pyrex tubes so that it could be used again. It was first washed out with water. This removed the flaky deposit, which had formed at certain places under the electrodes, and most of the narrow ring-shaped deposit near the electrodes. Hot nitric acid, aqua regia, concentrated sodium hydroxide, and alcohol failed to remove the remainder of the ring-shaped deposit or the interference film.

The deposit obtained with hydrogen was unaffected by any of the above chemicals. Hydrochloric acid, sulphuric acid, and carbon disulphide were also tried, but without effect.

#### *Quartz Tube*

When quartz tubing was used the interference pattern was again formed, but there was no flaky deposit.

#### *Index of Refraction*

Since the deposits showing interference patterns failed to respond to any chemical reagents, the only properties that could be determined positively were optical ones. By means of an indicometer described elsewhere in this

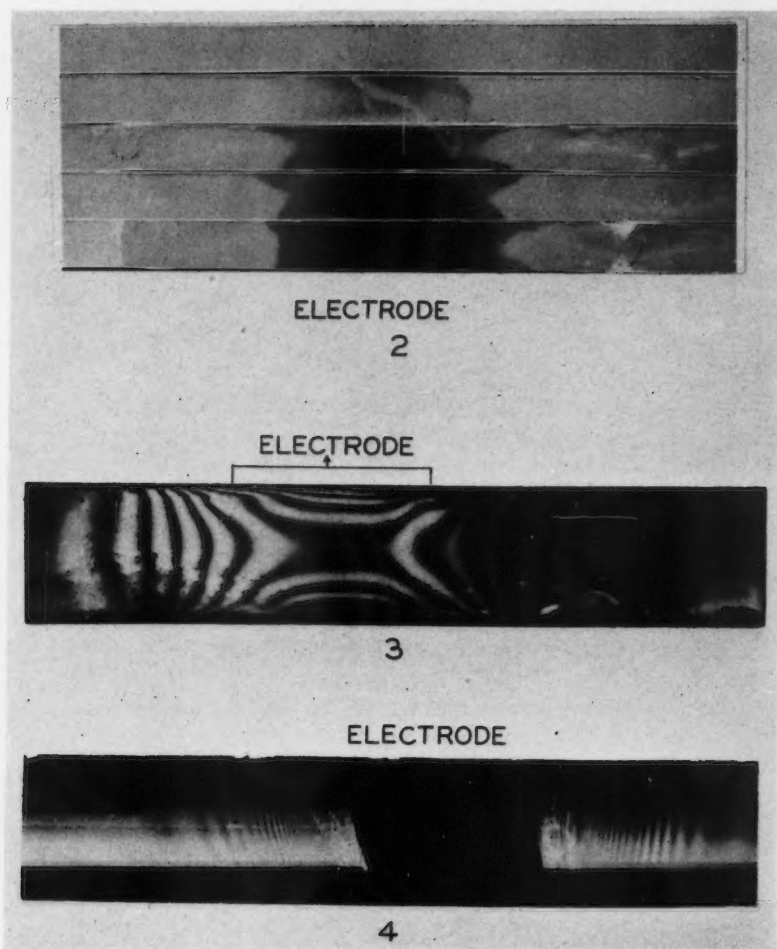


FIG. 2. Contact print of a series of gold-coated strips of glass after being exposed to a high frequency discharge in air for various times: Note removal under electrode.

FIG. 3. Photograph, by reflected sodium light, of deposit showing interference pattern, on glass strip, in region under electrode.

FIG. 4. Photograph of deposit showing interference pattern, on tube walls, on either side of an electrode.

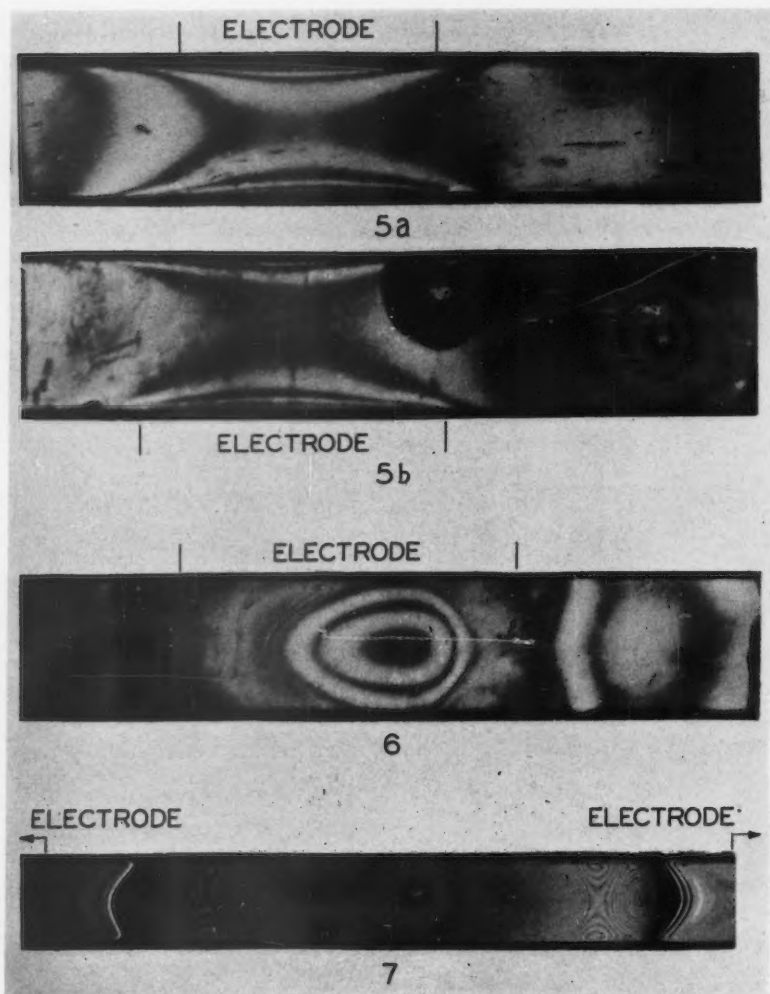


FIG. 5. Interference pattern: (a) with electrodes at room or higher temperature; (b) with electrodes and adjacent parts of discharge tube packed in dry ice.

FIG. 6. Interference pattern under electrode, with discharge at very low pressure.

FIG. 7. Interference pattern on glass strip in polystyrene tube.



issue (10) the index of the deposit was found to be about  $1.497 \pm 0.003$ , the same as that of silica in the form of cristobalite. The value of the index was identical whether the film was formed in Pyrex glass or quartz tubing.

### *Polystyrene Tube*

In an effort to determine the extent to which the above phenomena depend on the silicate nature of the glass and quartz, some experiments were conducted using polystyrene tubing. It was found that a deposit could be quite easily obtained from polystyrene, forming just beyond the electrode region and also in the center of the tube between the electrodes. Little deposit formed on strips under the electrodes, but outside the electrode region the deposit was very marked (Fig. 7). When the tube had been washed out with alcohol, and also when it was allowed to become appreciably hot, a brownish deposit formed. If, however, no alcohol was used and the tube was kept cool, the deposit was quite colorless, although more translucent than transparent. The index of the deposit thus formed proved to be exceptionally low and to be a function of the thickness and of the time, increasing with both (10).

Spectrograms were taken of the light from the discharge in a polystyrene tube. The CO bands with heads at 4835 (0,1), 5198 (0,2), 5610 (0,3); the CO<sup>+</sup> bands at 2198.8 (0,0), 2299 (0,1), 2325 (1,2), 2419 (0,2), 2446 (1,3); the CO<sub>2</sub><sup>+</sup> bands at 2896, 2883, and the carbon line 2478 can be clearly seen in Fig. 8 (a and b). For purposes of comparison a spectrogram of light from a discharge in a Pyrex tube is shown in Fig. 8 c.

### COMPARISON OF D-C. AND A-C. DISCHARGES

Since the removal near the electrode by high frequency discharges seemed to be of the same nature as cathodic sputtering, it was thought advisable to compare the conditions at the electrodes of a high frequency discharge with those at the cathode of a d-c. discharge. With this in view the following observations were made.

#### *Direct Current Discharge with Internal Electrodes*

Disk electrodes of diameter 2.25 cm. were placed 23.5 cm. apart inside a Pyrex glass tube whose internal diameter was about 2.5 cm. A d-c. discharge was operated with a potential difference of 750 v. between the electrodes, and a current of 5 ma. The widths of the cathode glow and cathode dark space were about 0.5 and 1.5 mm. respectively. To ensure cool operation, the rotary switch and the relay were used so that the discharge was on for 17.3 hr. out of a total of 117. At the end of this time, *there was a noticeable deposit on the walls at the cathode end of the tube, but none at the anode end.* Since the surface of the aluminum cathode had been roughened by the discharge, the deposit was assumed to be due to cathodic sputtering. On the walls very near the cathode, there was little, if any, deposit, but, as the distance from this

electrode increased, the deposit was more marked, its thickness reaching a maximum at a distance of about 1.5 to 2 mm., after which it gradually decreased. This maximum is nicely shown in Fig. 9, which also shows how rapidly the maximum thickness is attained on the electrode side.

#### *High Frequency Discharge with Internal Disk Electrodes*

With high frequency excitation, the electrodes used for the d-c. discharge were found to be unsuitable because their diameter was less than that of the tube and, if more than a certain amount of power was supplied, the discharge appeared on both sides of the disks. To prevent this, new electrodes were made that would just fit inside the tube.

At first only one electrode was used, one of the leads from the tank circuit being left unconnected. After a total run of 117 hr., some deposit showing an interference pattern in reflected light was visible near this electrode.

With two electrodes, similar patterns were obtained near each in only 13 hr. In this case, the oscillator could be adjusted to the load, and thus the power provided was much greater than when the single electrode was used. Fig. 10 is a photograph of the interference fringes near one of the electrodes.

#### *External Disk Electrodes*

Two glass windows were fastened to the ends of a short Pyrex glass tube 10 cm. long by means of polystyrene cement, and the two disk electrodes previously used for the d-c. discharges were placed *outside* the tube pressing against the windows. A high frequency discharge was induced in the tube, and after a total time of 89 hr. (net time is about one-seventh of this), interference fringes could be seen near each end of the tube.

#### *Comparison of Appearance of D-C. and High Frequency Discharges*

With internal electrodes and a pressure of the order of 1 mm., a typical direct current discharge in air was obtained. Starting at the cathode, the cathode glow, the Crookes dark space, the blue negative glow, the Faraday dark space, and the pink-red positive column followed in order. At the same pressure, the high frequency discharge had somewhat the same appearance, except that *each of the electrodes seemed to be an effective cathode*. Associated with each was a cathode glow, a Crookes dark space, a blue negative glow, a Faraday dark space, and a pink-red positive column, which was now in the central region. This was true with both internal and external disk electrodes. When external *sleeve* electrodes were used, the cathode glow and the Crookes dark space appeared at the wall parallel to, rather than normal to, the axis of the tube. Inside the Crookes dark space the region surrounded by the electrode was filled with the blue negative glow.

If only one electrode was used, either internally or externally, the discharge was essentially the same, except that the so-called 'positive column' tapered off at the end remote from the electrode, until it disappeared.



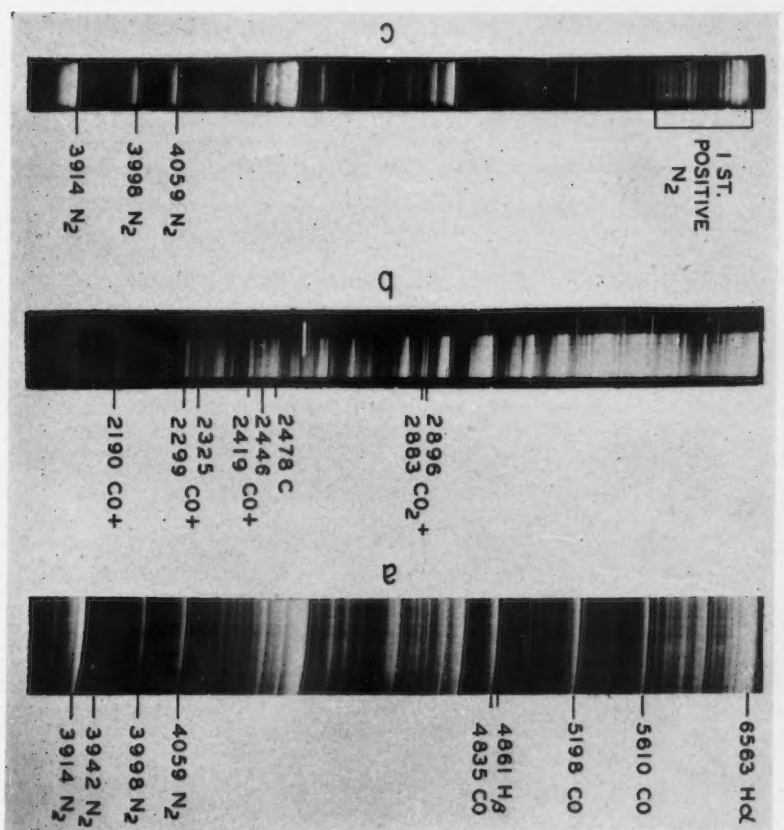


FIG. 8. Spectra of high frequency discharge in air: (a) in polystyrene tube, visible region; (b) in polystyrene tube, ultraviolet region; (c) in Pyrex tube, visible region.

FIG. 9. Deposit showing interference pattern near the cathode, on walls of a tube carrying a d-c. discharge.

FIG. 10. Interference pattern near an internal disk electrode, on the walls of a tube carrying a high frequency discharge.

FIG. 13. Photograph of the pattern on which measurements of thickness were made to obtain the dots plotted in Fig. 12.

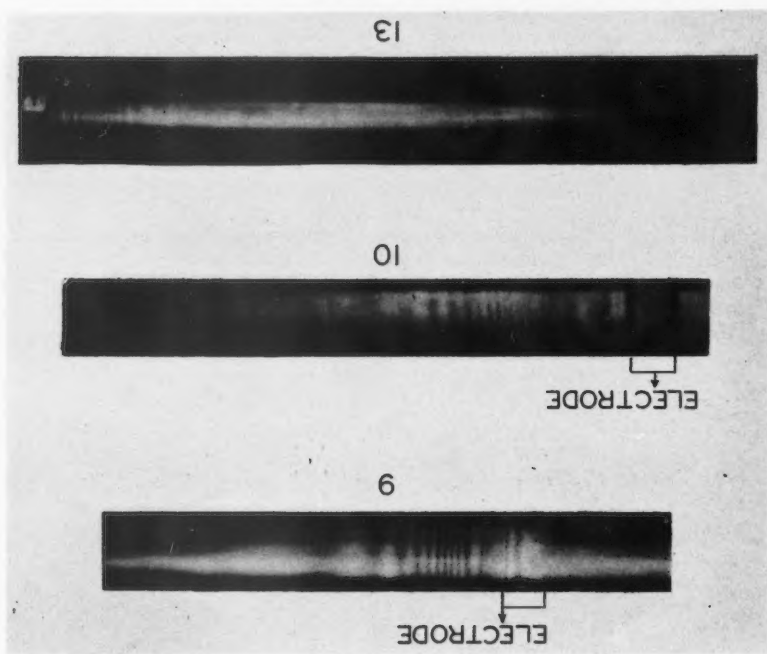


PLATE IV

### Discussion

It is possible to explain many of the above facts by the following hypotheses concerning the mechanism of high frequency discharges.

That there is a similarity between the conditions at each electrode in a high frequency discharge and those at the cathode in a d-c. discharge is evident from the marked similarity in appearance. If this likeness is more than superficial, and if the electrode regions in the high frequency discharge are subject to strong positive ion bombardment, the removal of metals and non-metals in these regions can be considered to be due to a type of sputtering. It is thus worth while examining the conditions within a high frequency discharge tube.

To begin with, it should be noted that there is no justification for considering a high frequency discharge as a d-c. one in which the anode and cathode alternate every half-cycle. If this were true the positive column should be visible in the Faraday dark space, and this is emphatically not the case. On the other hand, as will appear later, it is useful to consider the high frequency discharge as essentially determined by the d-c. wall and space charges, the sole function of the high frequency field being to maintain the 'electron temperature'. Although the external sleeve electrode type of discharge will be considered, the fundamental conceptions are the same for any type of high frequency discharge, using either internal or external electrodes.

For stability, the total quantity of charge that crosses any cross section of the tube, or which reaches any wall in one cycle must be zero.

This means that Boltzmann's equation,

$$n = n_0 e^{\frac{qV}{kT}},$$

where  $n$  is the density of electrons at a point,

$q$  is the electronic charge,

$V$  the potential of the point,

$n_0$  the density corresponding to  $V = 0$ ,

$k$  Boltzmann's constant,

$T$  the absolute temperature,

holds not only radially, as in the case of d-c. discharges, but also axially, subject to the assumptions that high speed electrons, which cannot be said to be diffusing, are negligible in number, and that the net effect of the alternating field is zero over one cycle.

From this equation it can be seen that, in a potential gradient, the density gradient of electrons will be such that they will tend to diffuse against the field. This 'up-hill' diffusion is the key to the stability of the discharge in spite of the presence of d-c. fields.

Where the potential is lowest, not only will the electron density be lowest, but the field will be such as to tend to attract positive ions, so a high positive space charge will develop. In view of this high positive space charge, the only possible cause of the low potential is a high negative wall charge. This wall charge is again maintained by up-hill electron diffusion, this time to the walls. The number of electrons diffusing to the walls must exactly equal the number of positive ions reaching the wall by diffusion and repulsion from the positive space charge, plus the number of secondary electrons emitted.

The existence of a negative space charge is highly improbable. In order to have stability under such conditions, the positive ions, fewer in number than the electrons, would have to diffuse to the walls against the field due to this negative charge as fast as the electrons move under the influence of both field and diffusion. In view of the much greater mobility and coefficient of diffusion of the electrons (Kennard (5, p. 473) places them at many hundred times the values for the positive ions) this seems impossible.

The magnitude of the negative wall charge and positive space charge that can exist in a stable condition is determined by the ability of the electrons to diffuse against a field. This is dependent on the following relation, given by Kennard (5, p. 466), between the coefficient of diffusion and the mobility.

$$\frac{D}{U} = \frac{kT}{q},$$

where  $D$  is the coefficient of diffusion,

$U$  the mobility,

$T$  the absolute temperature,

$k$  Boltzmann's constant,

$q$  the ionic charge.

Thus, the greater the electron temperature, the greater the coefficient of diffusion relative to the mobility, and hence the greater the negative wall charge that can be maintained. The electron temperature will be maintained by the high frequency field, so the more intense that field, the higher the negative wall charge.

This wall charge is the dominant factor in determining the potential at any point, for where the positive space charge is largest, the potential is most negative. Thus, the potential surrounding a wall charge is worth examining in some detail.

#### *Potential Distribution Due to a Wall Charge*

Assume a uniform wall charge  $q/\text{cm}^2$  on the surface of a cylinder of radius  $a$ , the charged portion being  $2b$  cm. long, and consider the potential produced at a distance  $x$  from the median plane of the charged portion, both on the axis and on the wall.

Potential on the axis is given by

$$V = q \int_{x-b}^{x+b} \int_0^{2\pi} \frac{ad\theta dx}{\sqrt{x^2 + a^2}}$$

$$= 2\pi a q \left\{ \sinh \frac{(x+b)}{a} - \sinh \frac{(x-b)}{a} \right\}.$$

Potential on the wall by

$$V = q \int_{x-b}^{x+b} \int_0^{\pi} \frac{2ad\phi dx}{\sqrt{x^2 + (2a \sin \phi)^2}}$$

The evaluation of the latter integral is given in Appendix A.

The results have been plotted in Fig. 11 for different values of  $b/a$ .

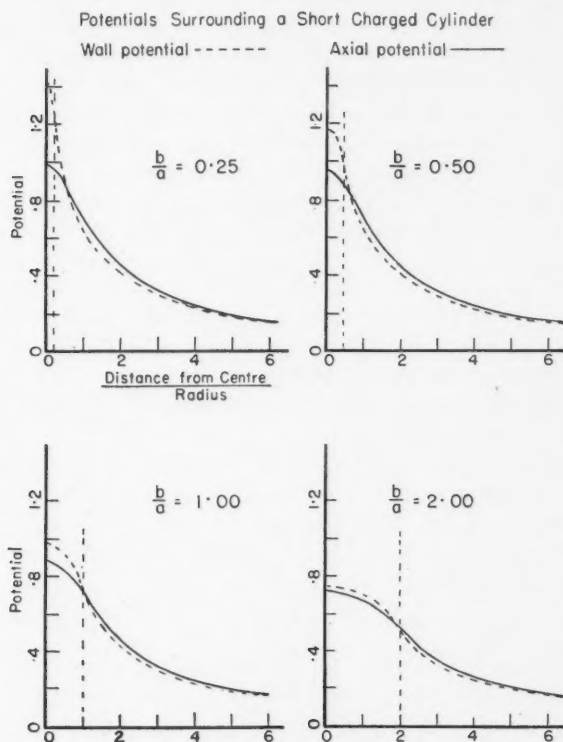


FIG. 11. Graphs showing how potentials, on the tube wall and at axial points, due to a uniform cylindrical wall charge, vary with the distance from the center of the discharge.

From the graphs in Fig. 11 it is seen that the radial field due to a wall charge is very small unless  $b/a$  is small. In general it is seen that there will be no radial field due to the wall charge unless the wall charge is not uniform. Indeed, if there is a high negative wall charge under the electrodes, the radial field between the electrodes *might actually be positive*,\* as can be seen from the graphs. Banerji and Ganguli (2) did observe such a change in sign of the radial field.

#### *Role of High Frequency Field*

The role of the high frequency field may now be examined. The potential distribution due to the charging of the electrodes will be somewhat similar to that of a uniform charge, to which Fig. 11 applies, the chief difference being that with our cylindrical electrodes, the charge tends to concentrate at the edges, the potential of the wall being constant under the electrodes, with a very steep gradient just outside. Since the general solution applicable to a short charged cylindrical conductor such as was actually used failed to respond to any method of attack at the writers' command, the approximation of a uniformly charged cylinder was used. Except right at the edges of the electrodes, the difference is slight.

The displacement of the ions because of this field will alter it somewhat, but that effect may reasonably be considered of second order magnitude compared with the field from the electrodes.

In view of the above, it can be seen from Fig. 11 that the only *radial* high frequency field of any consequence will be that directly under the electrodes. This, coupled with the fact that the greatest *axial* fields occur just outside the electrodes, means that the electrons under the electrodes may be expected to have very high temperatures, with the resulting high negative wall charge. If the alternating field is very intense, it may even make the radial field positive momentarily each cycle, despite the wall charge and positive space charge. Because of the high electronic mobilities this would greatly increase the flow of electrons to the walls.

Apart from the electrode region, the chief function of the high frequency appears to be to maintain the electron temperature. Townsend (12) found that the magnitude of the alternating field in the glows outside the electrode region was identical with that of the d-c. field in the positive column of a corresponding d-c. discharge.

#### *Summary of Hypothesis*

To summarize, a high frequency discharge is regarded as largely determined by the d-c. space and wall charges, notably the high negative wall charge under the electrodes. The function of the high frequency field is considered essentially to be to maintain the electron temperature.

\* Used herein to mean that potential increases as the radius increases.

This hypothesis leads to the following conclusions.

1. There will be a negative radial field everywhere in the tube except possibly for a region a short distance outside the electrodes where the field due to the high wall charge under the electrodes changes sign.

2. This radial field will be very much more intense under the electrodes than elsewhere in the tube. This is in good agreement with the fact noted above, that the removal occurs only under the electrodes.

3. Because the radial field is largely caused by the positive space charge, it will increase as the wall is approached, being a maximum at the wall. (This can be seen from Boltzmann's equation. If there is a radial field, the potential near the wall will be less than on the axis, hence the number of electrons will be less, and since the field will tend to force the positive ions away from the center towards the walls, a positive ion sheath will develop near the walls, and most of the radial field will be in this region.) Confirmation of this conclusion will appear below.

4. No part of the above argument requires two electrodes, and it should hold equally well with only one. As has been pointed out above, a perfectly satisfactory discharge can be set up using only one external electrode.

The high positive ion bombardment resulting from the high radial field under the electrodes accounts for the removal of metals in this region. Sputtering of nonmetals has been shown to occur by Stark and Wendt (9), so the same phenomenon will explain the removal of the constituents of glass and polystyrene from the tube walls, such removal also occurring under the electrodes.

#### EXPLANATION OF DEPOSITS

As noted above, several different types of deposit were obtained, and deposition occurred in different regions.

The deposit showing an interference pattern, which, as already noted, for Pyrex and quartz tubes is probably cristobalite, always has smooth contours and, in general, is thickest near discontinuities. The nature of these deposits, examples of which are given in Figs. 3, 4, 5, and 6, indicates that the material is deposited by diffusion, as is evident from the following discussion. If we assume that the silica can be removed by the high bombardment at the walls under the electrodes, but not by the ions in the less intense fields over strips that are nearer the axis of the tube, the fact that the deposit is heaviest at the edges and corners is explained by the proximity of these regions to the source compared with the central portions. To work out a diffusion function for the inside of a tube containing a strip is extremely difficult, but it is possible to obtain a good approximation for diffusion to the walls outside the electrode region.

Assuming all the silica to originate under the electrodes and to diffuse to the walls, we have Laplace's equation

$$\Delta D = 0$$

within the tube, where  $D$  is the density of material at any point in the tube.

Using as boundary conditions  $D = C$  under the electrodes and  $D = 0$  elsewhere on the wall, we find that:

$$\left. \frac{\partial D}{\partial r} \right|_{r=a} = \frac{2C}{\pi} \left[ \sum_{n=1}^{n=\infty} - \left\{ \left( 1 - \frac{I_1(na)}{I_0(na)} \right) \sin(nb) \sin(nx) \right\} + \cot \left( \frac{x+b}{2} \right) - \cot \left( \frac{x-b}{2} \right) \right].$$

In this expression,

$a$  is the radius,

$2b$  is the length of the electrode,

$x$  is the distance from the center of the electrode to the point under consideration,

$I_0$  and  $I_1$  are modified Bessel's functions of the first kind.

The derivation of the above expression is given in Appendix B.

The rate of flow to the wall at any point will be proportional to  $\left. \frac{\partial D}{\partial r} \right|_{r=a}$  so the thickness of the deposit at that point at any time will also be proportional to this expression.

Fig. 12 shows the comparison of theoretical and experimental results. The curve is the theoretical one, given by the above equation. The points are experimental ones, taken from a photograph of the tube shown in Fig. 13, the fringes being considered as equal vertical interval contour lines. Points have been taken from the fringe patterns near both electrodes. The maximum thickness of the deposit for which the fringes could be separated was about 7 wave lengths (14 fringes), or about  $2.5 \times 10^{-4}$  cm. The thickness became greater than this as the electrode was approached, but the fringes were too close to be separated by the traveling microscope used.

The tube dimensions used in the theoretical calculation were those of the experimental set up. The agreement appears sufficiently satisfactory to support the contention that these deposits are laid down by diffusion to the walls.

#### *Diffusion and Disk Electrodes*

For comparison, the diffusion curves for disk electrodes have been calculated. Two theoretical curves have been plotted. For one, it was assumed that the diameter of the electrode at which the sputtering occurred was equal to the inner diameter of the tube, and that the density of the sputtered particles across the face of the electrode was uniform. Otherwise the boundary conditions were the same as in the case of the external electrodes already given.



The resulting equation is:

$$\left. \frac{\partial D}{\partial r} \right|_{r=a} = -C \sum_{n=1}^{\infty} \frac{2}{a} e^{-\frac{r_n}{a} z},$$

where  $r_n$  is the  $n$ th root of a Bessel function of the first kind of order zero, and the remaining symbols are the same as for the external electrode case.

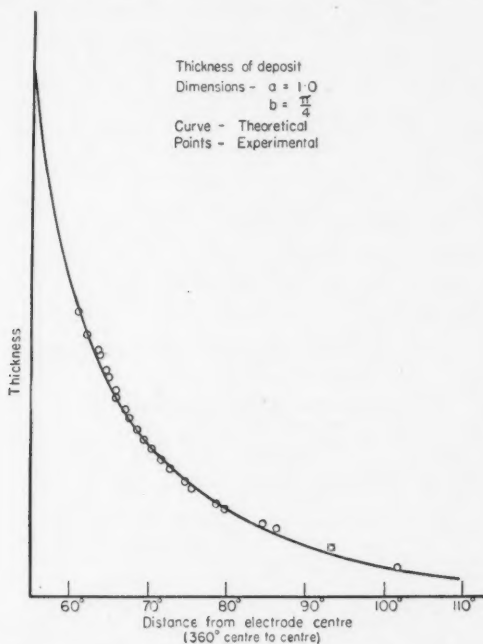


FIG. 12. The curve shows how the thickness of a wall deposit, assumed to result from diffusion, should vary with the distance from the source. The dots are based on measurements of thickness obtained from an actual interference pattern.

This curve is shown in Fig. 14, Graph 1.

For the second theoretical curve, only one boundary condition was changed. It had been observed that, after a high frequency discharge had passed between two polished aluminum disk electrodes for some time, the central part of each electrode had lost its polish but the outer parts had not. It was assumed for this second theoretical case, therefore, that the sputtering took place over an area having a diameter equal to two-thirds that of the tube. The boundary conditions thus are:

$$\begin{aligned} D(r, \infty) &= 0; D(a, x) = 0; D(r, 0) = C, & r < b \\ &= 0, & b < r < a. \end{aligned}$$

In this case  $b = 2/3a$ .

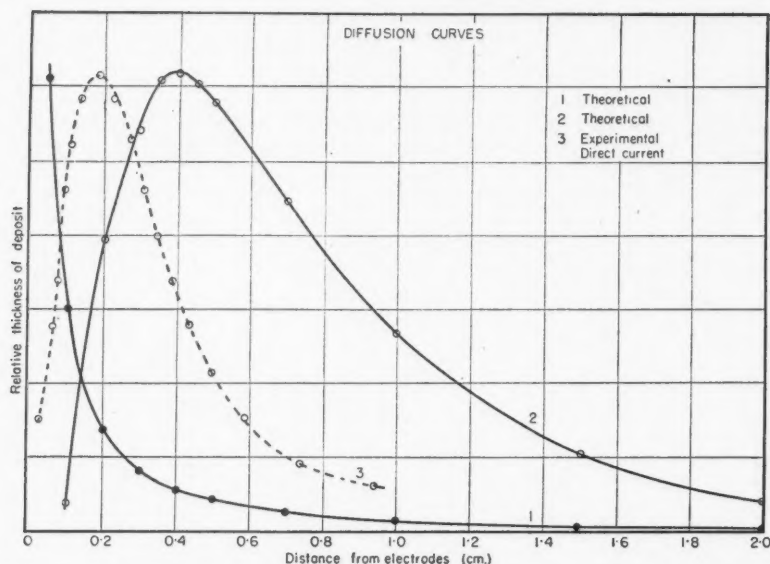


FIG. 14. Graphs showing how the thickness of material deposited on tube walls by diffusion varies with the distance, when the source is a disk electrode. Graph 1 is based on the assumption that material is released from the whole face of the disk; Graph 2, on the assumption that the effective diameter of the disk is two-thirds the diameter of the tube. Graph 3 is based on actual measurements of thickness of the deposit showing fringes, reproduced in Fig. 9.

With these boundary conditions, the solution to Laplace's equation is:

$$D = C \sum_{n=1}^{n=\infty} \frac{4}{3r_n} e^{-\frac{r_n}{a}x} \cdot J_0\left(r_n \frac{r}{a}\right) \cdot \frac{J_1\left(\frac{2r_n}{3}\right)}{\{-J_1(r_n)\}^2}$$

and

$$\left. \frac{\partial D}{\partial r} \right|_{r=a} = -C \sum_{n=1}^{n=\infty} \frac{4}{3a} e^{-\frac{r_n}{a}x} \cdot \frac{J_1\left(\frac{2r_n}{3}\right)}{J_1(r_n)}$$

The values of  $\left. \frac{\partial D}{\partial r} \right|_{r=a}$  are plotted in Graph 2, Fig. 14.

Fig. 14, Graph 3, is an experimental curve taken from the photograph shown in Fig. 9. A comparison of the three curves of Fig. 14 also supports the contention that the mechanism of deposition is one of diffusion. Evidence is also provided that the effective diameter of the electrode is somewhat less than its actual diameter.

#### Deposits at Low Pressure

The nature of the deposit on strips under the electrodes at low pressures, shown in Fig. 6, is probably due to the fact that at lower pressures the ionic free path is greater and hence the positive space charge is farther from the

walls. The edge of the strip is thus outside the space charge and under bombardment, as is the tube wall. The center of the strip is nearer the tube center, and hence under less bombardment. Apparently in this position the rate of deposition is greater than the rate of removal, and hence the deposit. At still lower pressures no deposit at all formed on the strip.

### *Flaky Deposits*

The gray flaky deposits, which are formed in glass tubes but not in quartz ones, are probably constituents of glass other than silica, notably boron trioxide, sodium oxide, and aluminum oxide. The sharp localization of these deposits indicates that the material, rather than diffusing to the walls, is cast down by a field. If the particles generally take a positive charge in the discharge, there will be an excess deposit under or near the electrodes, where the particles will be re-removed, unless they are in some region where the radial field, and hence the positive ion bombardment, is reduced. Thus they will accumulate just outside the electrode region and under loose spots of the electrodes.

A similar explanation probably accounts for the localization of the metallic deposits. In this case the sputtering rate is much greater, and deposit will become greater than removal only at a considerably greater distance from the electrodes than for the flaky deposits.

### *Polystyrene*

The location of the deposits in polystyrene indicates that the particles must pick up a negative charge in the discharge, for deposition occurs in the two places where the radial field is least negative, just outside the electrode region, and in the center of the tube between the electrodes.

The brown deposit observed on the walls of tubes that had either been cleaned with alcohol, or had been allowed to become hot, seems to be very similar to that obtained by Harkins and Gans (3), who found that a reddish brown solid formed very rapidly when a pure electrodeless discharge was run in benzene. They identified this as a complex hydrocarbon of formula  $(CH)_n$ . Carbon was also obtained, and in the presence of oxygen, carbon monoxide and water. In the work reported in this paper spectroscopic evidence has been found of the presence of carbon, carbon monoxide, and carbon dioxide in an air discharge in a polystyrene tube. Considering that benzene would be one of the chief products of the cracking of polystyrene, it is likely that the deposit found in this work is identical with that investigated by Harkins and Gans.

When no alcohol was used, and when the temperature was kept low, the brown deposit could be practically eliminated. The deposit then probably consists of polystyrene molecules, modified only slightly, if at all, by the discharge. It appears that the effect of the alcohol and of the heat is to make the polystyrene more susceptible to cracking in the discharge.

## SPUTTERING

This investigation may cast some light on the general problem of sputtering, for, although the phenomenon has been known for many years, it has not yet been satisfactorily explained. Lewis (6), in her recent monograph, states that it is not known whether the particles emitted are atomic or molecular in size.

The observations on the silica deposits do not solve this problem, as the silicon could be removed as silica and, when the discharge was in air or in helium, could be deposited unchanged, or, with hydrogen the carrier gas, reduced to silicon either before or after deposition. On the other hand, the silicon could be removed in atomic form and oxidized in the discharge if all the oxygen was not removed by the hydrogen carrier gas. In either case we would expect silica to be deposited in air or helium and either silicon or silica in hydrogen. The mirrorlike deposit obtained with hydrogen as carrier gas could not be positively identified, but it was probably silicon.

With polystyrene, however, the evidence is very strong that the particles removed and deposited were fairly large molecules. As is pointed out in the accompanying paper (10), the evidence there presented suggests that the deposit is of polystyrene molecules, cast down into a rather loose mass. This indicates that in some cases at any rate, sputtered particles are at least of molecular size.

## SUMMARY OF CONCLUSIONS

On the basis of the hypothesis that the high frequency discharge is essentially determined by the d-c. wall and space charges, differences in which are caused by differences in the electron temperature maintained by the high frequency field, it has been shown that there is a strong positive ion bombardment of the walls under the electrodes, and that the bombardment is of much lower intensity elsewhere in the discharge tube. This has been verified by a comparison of the nature of d-c. and high frequency discharges and by the fact that both metals and the materials of which the walls are made, whether of silicate or of an organic plastic nature, are removed in the electrode region by a process akin to sputtering. These materials are deposited in regions more or less remote from the electrodes, where the bombardment is reduced.

It is also shown that at least the particles of polystyrene removed by the positive ion bombardment are of molecular dimensions or larger.

## Acknowledgments

The authors wish to express their sincere appreciation to Prof. J. K. Robertson, under whose direction this work has been conducted, for his untiring interest, helpful encouragement, and inspiring confidence; to Dr. R. L. Jeffery for his help in the development and checking of the mathematical aspects;

to Prof. E. F. Burton of the University of Toronto for his kind donation of the helium required for part of this investigation; and to many members of staff of Queen's University for helpful co-operation.

In addition, grateful thanks are due the National Research Council of Canada, whose generous award of a Studentship to one of us (R.W.S.) made this work possible.

### References

1. BANERJI, D. and BHATTACHARYA, D. Phil. Mag. [7] 17 : 313. 1934.
2. BANERJI, D. and GANGULI, R. Phil. Mag. [7] 15 : 676. 1933.
3. HARKINS, W. D. and GANS, D. M. J. Am. Chem. Soc. 52 : 5165. 1930.
4. HAY, R. H. Can. J. Research, A, 16 : 191. 1938.
5. KENNARD, E. H. Kinetic theory of gases. 1st ed. McGraw-Hill Book Company, Inc., New York. 1938.
6. LEWIS, W. Thin films and surfaces. English Universities Press, London. 1946.
7. OLSEN, L. O., SMITH, C. S., and CRITTENDEN, E. C., Jr. J. Applied Phys. 16 : 425. 1945.
8. ROBERTSON, J. K. and CLAPP, C. W. Nature, 132 : 479. 1933.
9. STARK, J. and WENDT, G. Ann. Physik, 38 : 921. 1912.
10. STEWART, R. W. Can. J. Research, A, 26 : 230. 1948.
11. STRONG, J. Procedures in experimental physics. Prentice-Hall Inc., New York. 1938.
12. TOWNSEND, J. S. Phil. Mag. [7] 11 : 1112. 1931.

### APPENDIX A

#### Potential on the Wall of a Tube, a Section of which is Uniformly Charged with a Charge Density $q/\text{cm}^2$

Owing to the law of addition of potentials, this may be obtained from the potential due to a uniform wall charge extending from  $x = 0$  to  $x = x$  ( $x$  being the distance along the wall from the point under consideration) by subtraction.

Let tube radius =  $a$ , and  $\phi$  the angle shown in Fig. 15.

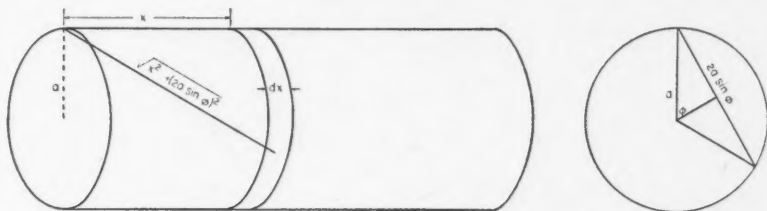


FIG. 15

$$\begin{aligned}
 V &= q \int_0^x \int_0^\pi \frac{2a \, d\phi \, dx}{\sqrt{x^2 + (2a \sin \phi)^2}} = 2aq \int_0^x dx \int_0^\pi \frac{d\phi}{\sqrt{x^2 + 4a^2 \sin^2 \phi}} \\
 &= 2aq \int_0^x dx \int_0^\pi \frac{d\phi}{\sqrt{x^2 + 4a^2 - 4a^2 \cos^2 \phi}}
 \end{aligned}$$

Set  $\theta = \phi - \pi/2$

$$\begin{aligned} V &= 2aq \int_0^x \frac{dx}{\sqrt{x^2 + 4a^2}} \int_{-\pi/2}^{\pi/2} \frac{d\theta}{\sqrt{1 - \frac{4a^2}{x^2 + 4a^2} \sin^2 \theta}} \\ &= 4aq \int_0^x \frac{K\left(\frac{4a^2}{x^2 + 4a^2}\right)^{\frac{1}{2}}}{\sqrt{x^2 + 4a^2}} dx \quad \left(\text{since } \frac{4a^2}{x^2 + 4a^2} < 1 \text{ for } x > 0\right) \end{aligned}$$

where  $K(k)$  is the complete elliptic integral:

$$\begin{aligned} &\int_0^{\pi/2} \frac{d\theta}{\sqrt{1 - k^2 \sin^2 \theta}} \\ K(k) &= \int_0^{\pi/2} \frac{d\theta}{\sqrt{1 - k^2 \sin^2 \theta}} = \int_0^{\pi/2} \left(1 + \frac{k^2 \sin^2 \theta}{2} + \frac{3k^4 \sin^4 \theta}{2.4} \right. \\ &\quad \left. + \frac{1.3.5k^6 \sin^6 \theta}{2.4.6} + \dots\right) d\theta = \frac{\pi}{2} \left\{1 + \left(\frac{1}{2}\right)^2 k^2 \right. \\ &\quad \left. + \left(\frac{1.3}{2.4}\right)^2 k^4 + \left(\frac{1.3.5}{2.4.6}\right)^2 k^6 + \dots\right\}, \end{aligned}$$

which converges if  $k^2 < 1$ .

Therefore:

$$\begin{aligned} \frac{K\left(\frac{4a^2}{x^2 + 4a^2}\right)^{\frac{1}{2}}}{\sqrt{x^2 + 4a^2}} &= \pi/2 \left( \frac{1}{\sqrt{x^2 + 4a^2}} + \left(\frac{1}{2}\right)^2 \frac{4a^2}{(x^2 + 4a^2)^{\frac{3}{2}}} \right. \\ &\quad \left. + \left(\frac{1.3}{2.4}\right)^2 \frac{4a^2}{(x^2 + 4a^2)^{\frac{5}{2}}} + \dots \right). \end{aligned}$$

Integrating term by term with respect to  $x$ ;

$$\begin{aligned} V &= 4aq \int_0^x \frac{K\left(\frac{4a^2}{x^2 + 4a^2}\right)^{\frac{1}{2}}}{\sqrt{x^2 + 4a^2}} dx = 2\pi aq \left[ \ln \frac{(x + \sqrt{x^2 + 4a^2})}{2a} \right. \\ &\quad \left. + \left(\frac{1}{2}\right)^2 \frac{x}{\sqrt{x^2 + 4a^2}} + \left(\frac{1.3}{2.4}\right)^2 \left( \frac{x}{\sqrt{x^2 + 4a^2}} - \frac{x^3}{3(x^2 + 4a^2)^{\frac{3}{2}}} \right) \right. \\ &\quad \left. + \left(\frac{1.3.5}{2.4.6}\right)^2 \left( \frac{x}{\sqrt{x^2 + 4a^2}} - \frac{2x^3}{3(x^2 + 4a^2)^{\frac{3}{2}}} + \frac{x^5}{5(x^2 + 4a^2)^{\frac{5}{2}}} \right) + \dots \right]. \end{aligned}$$

(Integrals of the form  $\int \frac{dx}{(x^2 + a^2)^{\frac{2n+1}{2}}}$  are obtained by the substitution

$$x = a \tan \theta$$

*Convergence*

By Stirling's formula:  $\frac{1.3.5 \dots (2n-1)}{2.4.6 \dots (2n)} = \frac{(2n)!}{(2^n n!)^2}$

$$\approx \frac{\sqrt{4n\pi} \left(\frac{2n}{e}\right)^{2n}}{2n\pi 2^{2n} \left(\frac{n}{e}\right)^{2n}} = \frac{1}{\sqrt{n\pi}}.$$

Hence the term:

$$\frac{1.3.5 \dots (2n-1)}{2.4.6 \dots (2n)} \text{ approaches zero as } \frac{1}{\sqrt{n}} \text{ as } n \rightarrow \infty.$$

Thus in the series for  $V$ , if all the coefficients of  $\frac{x}{\sqrt{x^2 + 4a^2}}$ ,  $\frac{x}{(x^2 + 4a^2)^{\frac{3}{2}}}$  etc. are grouped, the resulting coefficients will be series of the form:  $A \sum_n \frac{1}{n}$ , which diverges.

However, if the series is left grouped as above, it is dominated by the limiting value as  $x \rightarrow \infty$  since each term is positive and increases as  $x$  increases\* which is:

$$\sum_n \left( \frac{1.3.5 \dots (2n+1)}{2.4.6 \dots (2n+2)} \right)^2 \left( 1 - \frac{n}{3} + \frac{\frac{n(n-1)}{2!}}{5} - \dots + \dots + \frac{(-1)^n}{(2n+1)} \right).$$

But:

$$1 - \frac{n}{3} + \frac{\frac{n(n-1)}{2!}}{5} - \dots + \dots + \frac{(-1)^n}{(2n+1)} = \frac{2.4.6 \dots (2n)}{1.3.5 \dots (2n+1)}^{**}$$

Thus each term in the dominating series is of the form:

$$\frac{1.3.5 \dots (2n+1)}{2.4.6 \dots (2n+2)} \cdot \frac{1}{(2n+2)} \approx \sqrt{\frac{1}{(n+1)\pi}} \cdot \frac{1}{(2n+2)} = \frac{1}{(n+1)^{\frac{3}{2}} 2\sqrt{\pi}}.$$

Thus the series converges for all values of  $x > 0$ .

\* The derivative of this series is:

$$\left(\frac{1}{2}\right)^2 \frac{4a^2}{(x^2 + 4a^2)^{\frac{3}{2}}} + \left(\frac{1.3}{2.4}\right)^2 \frac{(4a^2)^2}{(x^2 + 4a^2)^{\frac{5}{2}}} + \dots$$

which is always positive.

\*\* Readily proved by expanding:

$$\frac{2.4.6 \dots (2n)}{(1+x)(3+x) \dots (2n+1+x)} \text{ in the form } \frac{a}{1+x} + \frac{b}{3+x} + \dots + \frac{r}{2n+1+x}$$

and putting  $x = 0$ .

Alternatively, the matrix:

$$\begin{bmatrix} 1 & 0 & 0 & 0 & 0 & . & . \\ -1 & 2 & 0 & 0 & 0 & . & . \\ 0 & -2 & 3 & 0 & 0 & . & . \\ 0 & 0 & -3 & 4 & 0 & . & . \\ 0 & 0 & 0 & -4 & 5 & . & . \\ . & . & . & . & . & . & . \\ . & . & . & . & . & . & . \end{bmatrix}$$

may be used to speed convergence.

If  $u_1 + u_2 + u_3 + \dots + u_n + \dots$  is a converging series in which  $u_1 u_2 u_3 \dots u_{n-1} > u_n > 0$ , and  $S_1, S_2, S_3 \dots S_n \dots$  is a sequence such that

$$S_n = u_1 + u_2 + \dots + u_n,$$

and the  $S_n$  sequence is arranged as a column vector and premultiplied by the above matrix, the product will be a column vector, the terms of which form a sequence  $R_1, R_2, R_3 \dots R_n \dots$ , i.e.:

$$\begin{bmatrix} 1 & 0 & 0 & 0 & 0 & . & . \\ -1 & 2 & 0 & 0 & 0 & . & . \\ 0 & -2 & 3 & 0 & 0 & . & . \\ 0 & 0 & -3 & 4 & 0 & . & . \\ 0 & 0 & 0 & -4 & 5 & . & . \\ . & . & . & . & . & . & . \\ . & . & . & . & . & . & . \end{bmatrix} \begin{bmatrix} S_1 \\ S_2 \\ S_3 \\ S_4 \\ S_5 \\ . \\ . \end{bmatrix} = \begin{bmatrix} R_1 \\ R_2 \\ R_3 \\ R_4 \\ R_5 \\ . \\ . \end{bmatrix}$$

where

$$\begin{aligned} R_n &= nS_n - (n-1)S_{n-1} \\ &= S_n + (n-1)(S_n - S_{n-1}) \\ &= S_n + (n-1)u_n. \end{aligned}$$

But since  $u_1 + u_2 + u_3 \dots$  is a converging series of positive terms,  $(n-1)u_n \rightarrow 0$  as  $n \rightarrow \infty$ .

Thus  $R_n$  approaches the same limit as does  $S_n$  as  $n \rightarrow \infty$ .

In some cases, as for example the above series for  $V$ ,  $R_n$  converges more rapidly than  $S_n$ , and so the transformation is of considerable value in summing the series.

For small values of  $x$ , i.e. values of  $x < 2a$ , a different approximation for  $V$  is of value, as the convergence of the above series is extremely slow.

$$V = 4aq \int_0^x \frac{K\left(\frac{4a^2}{x^2 + 4a^2}\right)^{\frac{1}{2}}}{\sqrt{x^2 + 4a^2}} dx$$



$$k = \sqrt{\frac{4a^2}{x^2 + 4a^2}}, \text{ therefore: } k' = \sqrt{\frac{x^2}{x^2 + 4a^2}}.$$

From *Tables of Functions* (Jahnke and Emde) we have:

$$K(k) = L + \frac{L-1}{4} k'^2 + \frac{9}{64} \left(L - \frac{7}{6}\right) k'^4 + \dots, \quad ,$$

where

$$L = \ln \frac{4}{k'} = \ln \frac{4\sqrt{x^2 + 4a^2}}{x}.$$

Assume  $x \ll 2a$ , so neglect all terms in  $k'^n$  where  $n > 3$ . Approximate signs will not be used.

$$\frac{K}{\sqrt{x^2 + 4a^2}} = \frac{K}{2a} \left(1 - \frac{x^2}{8a^2}\right)$$

$$K = L \left(1 + \frac{k'^2}{4}\right) - \frac{1}{4} k'^2.$$

Therefore:

$$\begin{aligned} \frac{K}{\sqrt{x^2 + 4a^2}} &= \frac{1}{2a} \left[ \ln \frac{4\sqrt{x^2 + 4a^2}}{x} \left\{ 1 + \frac{x^2}{4(x^2 + 4a^2)} \right\} \cdot \left\{ 1 - \frac{x^2}{8a^2} \right\} - \right. \\ &\quad \left. \frac{1}{4} \frac{x^2}{x^2 + 4a^2} \cdot \left\{ 1 - \frac{x^2}{8a^2} \right\} \right] \\ &= \frac{1}{2a} \left\{ \ln 8a \left(1 - \frac{x^2}{16a^2}\right) + \frac{x^2}{8a^2} - \ln x \left(1 - \frac{x^2}{16a^2}\right) - \frac{x^2}{16a^2} \right\}. \end{aligned}$$

and thus:

$$V = 4aq \int_0^x \frac{K}{\sqrt{x^2 + 4a^2}} dx = 2q \left\{ \left( \ln \frac{8a}{x} \right) \left( x - \frac{x^3}{48a^2} \right) + x + \frac{1}{72} \frac{x^3}{a^2} \right\}.$$

## APPENDIX B

### Diffusion of Material from under the Electrodes to the Walls

Assumptions:

1. That the situation between two electrodes when there are only two differs slightly from the situation with an infinite number of evenly spaced electrodes.
2. That the density of material just inside the walls under the electrodes is constant. This is at best a rough approximation, particularly towards the edges of the electrodes. However, at any appreciable distance from the electrodes the error should be slight.
3. The density of material just inside the walls outside the electrode regions is zero. This should be true if there is no appreciable sputtering except under the electrodes.

Choose as origin the center of an electrode region.

Choose unit length so that the distance center to center between electrodes  $= 2\pi$ , as shown in Fig. 16.

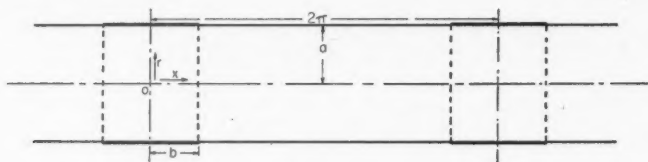


FIG. 16

In these units:

$$\text{Radius} = a$$

$$\text{Electrode length} = 2b$$

Laplace's equation in cylindrical co-ordinates:

$$\frac{\partial^2 D}{\partial x^2} + \frac{1}{r} \frac{\partial D}{\partial r} + \frac{\partial^2 D}{\partial r^2} = 0,$$

where  $D$  is the density of material at any point.

Then: for  $-\pi < x < \pi$  the boundary conditions are:

$$D = C \quad |x| < b \quad (\text{Assumption 2})$$

$$D = 0 \quad |x| > b \quad (\text{Assumption 3})$$

$D$  is periodic in  $x$ , with a period of  $2\pi$  (Assumption 1).

To solve:

$$\frac{\partial^2 D}{\partial x^2} + \frac{1}{r} \frac{\partial D}{\partial r} + \frac{\partial^2 D}{\partial r^2} = 0$$

set

$$D = X(x) R(r).$$

Thus:

$$R \frac{d^2 X}{dx^2} + \frac{X}{r} \frac{dR}{dr} + X \frac{d^2 R}{dr^2} = 0$$

or:

$$\frac{1}{X} \frac{d^2 X}{dx^2} + \frac{1}{rR} \frac{dR}{dr} + \frac{1}{R} \frac{d^2 R}{dr^2} = 0.$$

Therefore:

$$\frac{d^2 R}{dr^2} + \frac{1}{r} \frac{dR}{dr} - n^2 R = 0 \quad (n \text{ arbitrary})$$

and:

$$\frac{d^2 X}{dx^2} + n^2 X = 0.$$

(1)

$$\frac{d^2 X}{dx^2} + n^2 X = 0.$$

Therefore:

$$X = A_n \cos nx + B_n \sin nx \quad n \neq 0$$

$$X = A_0 + B_0 x \quad n = 0$$

Because of the choice of co-ordinates, and Assumption 1,  $X$  must be an even function.

Therefore:

$$B_0 = B_n = 0$$

and:

$$X = A_n \cos nx.$$

$$(2) \quad \frac{d^2 R}{dr^2} + \frac{1}{r} \frac{dR}{dr} - n^2 R = 0.$$

Solution for  $n \neq 0$ :

$$R = E_n I_0(nr) + F_n K_0(nr) \quad (E_n, F_n \text{ const.})$$

where:

$I_0$  is a modified Bessel's function of the first kind.

$K_0$  is a Bessel's function of the second kind.

Solution for  $n = 0$ :

$$R = F_0 \ln(r) + E_0.$$

However  $R$  does not become infinite as  $r \rightarrow 0$ , therefore:

$$F_n = F_0 = 0$$

and:

$$R = E_n I_0(nr) \quad n \neq 0$$

$$R = E_0 \quad n = 0$$

Therefore the desired solution to Laplace's equation is:

$$D = A_0 E_0 + \sum_{n=1}^{\infty} A_n E_n I_0(nr) \cos(nx).$$

At the wall:

$$D|_{r=a} = A_0 E_0 + \sum_{n=1}^{\infty} A_n E_n I_0(na) \cos(nx).$$

$$= C \quad |x| < b$$

$$= 0 \quad |x| > b$$

Thus for this series:

$$A_0 E_0 = \frac{1}{2\pi} \int_{-b}^b C dx = \frac{bC}{\pi},$$

and:

$$A_n E_n I_o(na) = \frac{1}{\pi} \int_{-b}^b C \cos(nx) dx = \frac{2C}{\pi} \frac{\sin(nb)}{n}$$

or

$$A_n E_n = \frac{2C}{\pi} \frac{\sin(nb)}{n I_o(na)}.$$

Therefore:

$$D = \frac{bC}{\pi} + \frac{2C}{\pi} \sum_{n=1}^{\infty} \frac{\sin(nb)}{n I_o(na)} I_o(nr) \cos(nx).$$

The amount of material going to the walls and being deposited is proportional to:  $\left. \frac{\partial D}{\partial r} \right|_{r=a}$ .

Hence the amount deposited in any finite region between  $x = x_1$  and  $x = x$  is proportional to:

$$\int_{x_1}^x \left. \frac{\partial D}{\partial r} \right|_{r=a} dx = \frac{2C}{\pi} \sum_{n=1}^{\infty} \frac{\sin(nb) \sin(nx)}{n I_o(na)} I_1(na) + \text{const. (if } x_1 \text{ and } x > b).$$

(This device is employed to avoid having to deal with a series without the factor of convergence  $1/n$ .)

$$\lim_{n \rightarrow \infty} \frac{I_1(na)}{I_o(na)} = 1.$$

Now:

$$\frac{\sin(nb) \sin(nx)}{n} = \frac{\cos n(x-b)}{n} - \frac{\cos n(x+b)}{n}$$

and

$$\sum_{n=1}^{\infty} \frac{\cos(ny)}{n} = -\ln(2 \sin y/2)^*.$$

Differentiating, we get:

$$-\left. \frac{\partial D}{\partial r} \right|_{r=a} = \frac{2C}{\pi} \left[ \sum_{n=1}^{\infty} \left\{ 1 - \frac{I_1(na)}{I_o(na)} \sin(nb) \cos(nx) \right\} + \cot \frac{(x-b)}{2} - \cot \frac{(x+b)}{2} \right]$$

The convergence is supplied by the fact that:

$$\left\{ 1 - \frac{I_1(na)}{I_o(na)} \right\} \rightarrow 0 \text{ as } n \rightarrow \infty$$

as about  $\frac{1}{2n}$ , and the factor  $\sin(nb) \cos(nx)$  alternates in groups of terms, the sum of the terms in each group being nearly equal. The number of terms in each group depends on  $x$ .

\* Carslaw—*Fourier's Series and Integrals*, 3rd ed., p. 241. MacMillan and Co. 1930.

The Cesàro triangular matrix:

$$\begin{array}{ccccccc}
 1 & & & & & & \\
 1/2 & 1/2 & & & & & \\
 1/3 & 1/3 & 1/3 & & & & \\
 1/4 & 1/4 & 1/4 & 1/4 & & & \\
 & \cdot & \cdot & \cdot & \cdot & \cdot & \\
 & \cdot & \cdot & \cdot & \cdot & \cdot & \cdot \\
 & \cdot & \cdot & \cdot & \cdot & \cdot & \cdot
 \end{array}$$

was used to obtain a more rapidly converging series.

## A METHOD FOR THE DETERMINATION OF THE INDEX OF REFRACTION OF THIN TRANSPARENT FILMS<sup>1</sup>

BY R. W. STEWART<sup>2</sup>

### Abstract

The index of refraction of thin films deposited on an optical flat is obtained by comparison of the fringe system set up in the film with that in the air gap between the film and another optical flat. The use of the method is illustrated by application to films produced in high frequency discharge tubes. Films produced in Pyrex glass and quartz tubes are shown to be silica in the form of cristobalite. Films produced in polystyrene tubes prove to have an index of refraction that is very low and is a function of the thickness.

### Introduction

During the progress of an investigation of the effect of high frequency discharges on tube walls, reported elsewhere in this journal (2), a thin deposit of transparent material was obtained after a run of an hour or more. This deposit, which shows typical thin film interference fringes, formed both on the tube walls outside the electrode region and on thin strips of glass placed within the tube and under the electrode. It proved to be both mechanically hard and chemically inert. Films deposited on top of metallic coatings resisted concentrated nitric acid and strong bases, although prolonged immersion resulted in the dissolving of the underlying metal so that the material could then be rubbed off. The deposit itself, however, could be rubbed vigorously without damage.

Since the total quantity of material in these films was very small ( $2 \times 10^{-5}$  cc. spread over  $2 \text{ cm.}^2$  would be a large deposit) and the maximum thickness observed was about  $3 \times 10^{-4} \text{ cm.}$ , analysis by ordinary methods would be very difficult, particularly in view of the chemical inertness of the films. It was thus thought advisable to get some indication of the nature of this deposit by determining its index of refraction by a method suggested by the recent work of Tolansky (6) on the optical determination of the irregularities of crystal surfaces. A preliminary note regarding the method has been published (3).

In addition to the films obtained in Pyrex glass tubes, deposits were obtained in tubes made of polystyrene. For this plastic the index was found to vary with thickness. Most methods of determining the index of refraction of small samples of transparent materials are based on the fact that when two trans-

<sup>1</sup> Manuscript received January 28, 1948.

Submitted by Prof. J. K. Robertson, Department of Physics, Queen's University, Kingston, Ont.

<sup>2</sup> Holder of a studentship under the National Research Council of Canada, 1946-47. Now, Research Student at the Cavendish Laboratory, Cambridge, England.

parent media are in contact the boundary surface will reflect light unless the indices are identical. The index found is thus essentially a surface one and is valid only for homogeneous materials. The method described in this paper has the peculiar characteristic of measuring the index of *whatever is changing in thickness*, and is thus particularly useful in cases where the index is a function of the thickness.

### Apparatus and Procedure

An optically plane glass plate of dimensions about 15 by 20 by 5 mm. was covered by evaporation with a mirrorlike metallic coat whose coefficient of reflection was about 0.6. The plate was then placed in a discharge tube so that one end protruded about 3 mm. outside the region surrounded by one of two external electrodes. The tube was then operated for about 10 hr., so that a considerable deposit was laid down on top of the metal. Fig. 1, Plate I, photographed by reflected sodium light, shows the resulting pattern. Another similar semitransparent metallic coat was then formed by evaporation on top of the deposit, and also on top of a second optical flat of the same dimensions as the first. The two plates were placed with their coated faces together in a device designated herein as an *indicometer*, which could be accurately adjusted until the plates were less than 0.1 mm. apart, and sufficiently parallel to give observable interference fringes in the air gap. Adjustment was fine enough that the number and direction of the fringes could be controlled to give any desired set of conditions.

If the indicometer was then viewed in reflected or transmitted monochromatic light, two sets of superimposed multiple reflection fringes were visible, one in the deposit and the other in the air gap. In Fig. 2, Plate I, an enlarged photograph taken in transmitted sodium light, the points A and B are on the same fringe in each set. Thus they are points at which both the thickness of the air gap and of the film, and therefore the distances between the two glass surfaces, are equal. Since both the glass surfaces are optically plane, the distance between them is constant along the line AB, and is also constant along any line parallel to AB.

If the number of fringes due to reflection within the medium showing the original interference pattern is  $a$  in any line segment parallel to AB, and the number due to reflection in the air gap is  $b$  in the same line segment, the index of refraction of the medium is  $a/b$ , since along the line segment the change in thickness of the air gap is entirely due to the change in thickness of the film. This method is independent of any sudden phase changes at the boundary, as this change would cause only a fringe shift, not a change in the number of fringes between two points. Similarly it is independent of the thickness of the metal mirrors or of any other uniform layer, as long as this thickness is uniform.

The indicometer is shown in Fig. 3. The screws on the sides clamp the glass plates in place, while the plate, *A*, is held to the frame only by the three screws in the face. By adjusting these screws, which have a very fine pitch,

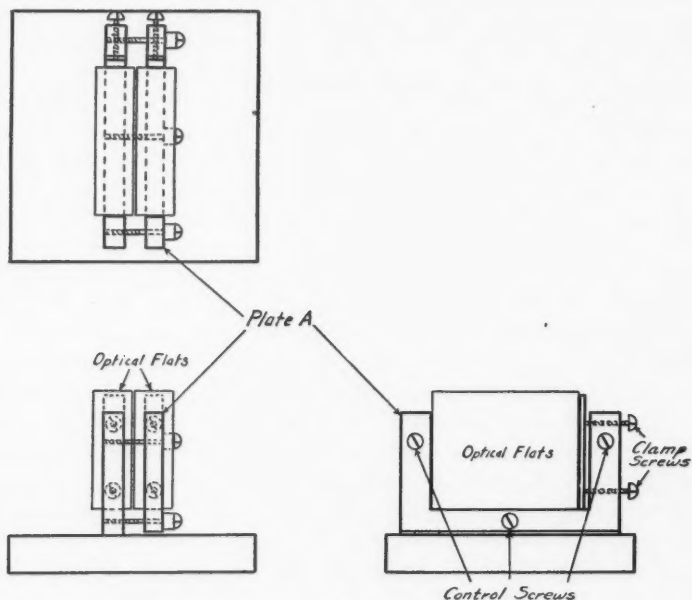


FIG. 3. Diagrams showing the mechanical arrangement for mounting and adjusting the optical flats in the indicometer.

any desired alignment can be attained. The number of fringes in the surface can be controlled within one, and the direction within a few degrees. In practice it was found advisable to have the two sets of fringes meet as nearly at right angles as possible.

### Observations

#### *Pyrex Glass and Quartz Tubes*

Films were obtained in Pyrex glass tubes with the plate originally coated with half-mirror surfaces of silver, magnesium and aluminum. The gas was air at a pressure of about 1 mm. of mercury.

The indices observed, for sodium light, were:

On silver	$1.489 \pm 0.012$
On magnesium	$1.488 \pm 0.008$
On aluminum	$1.484 \pm 0.006$

The estimates of precision were computed by Goodwin's method (1).



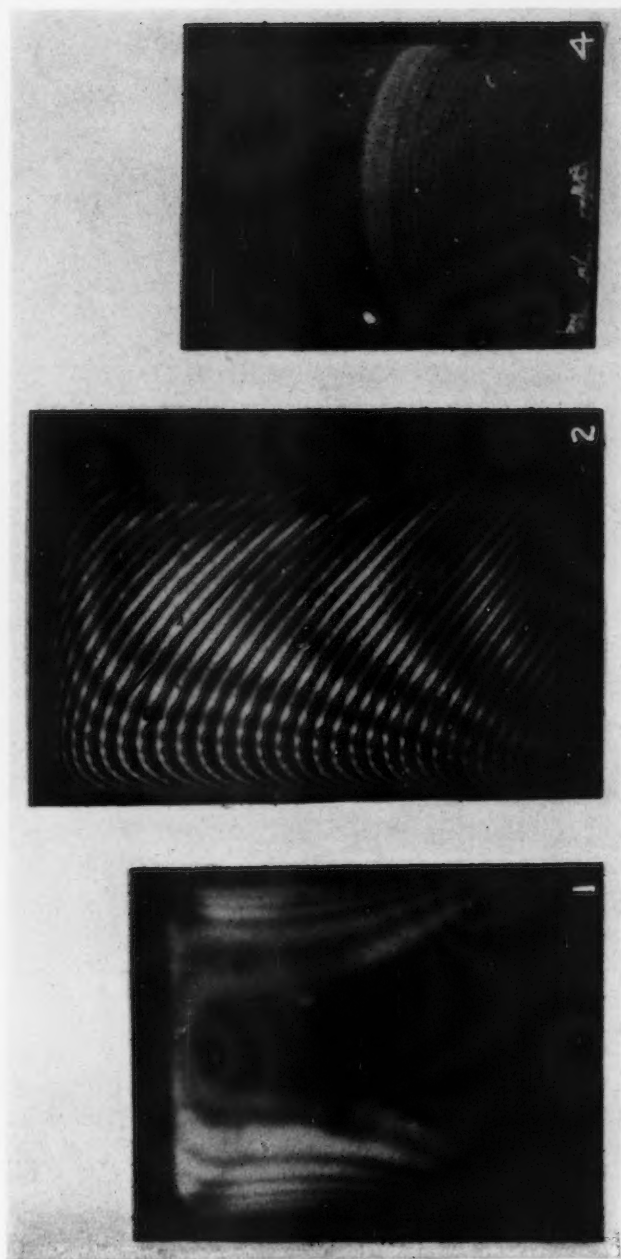
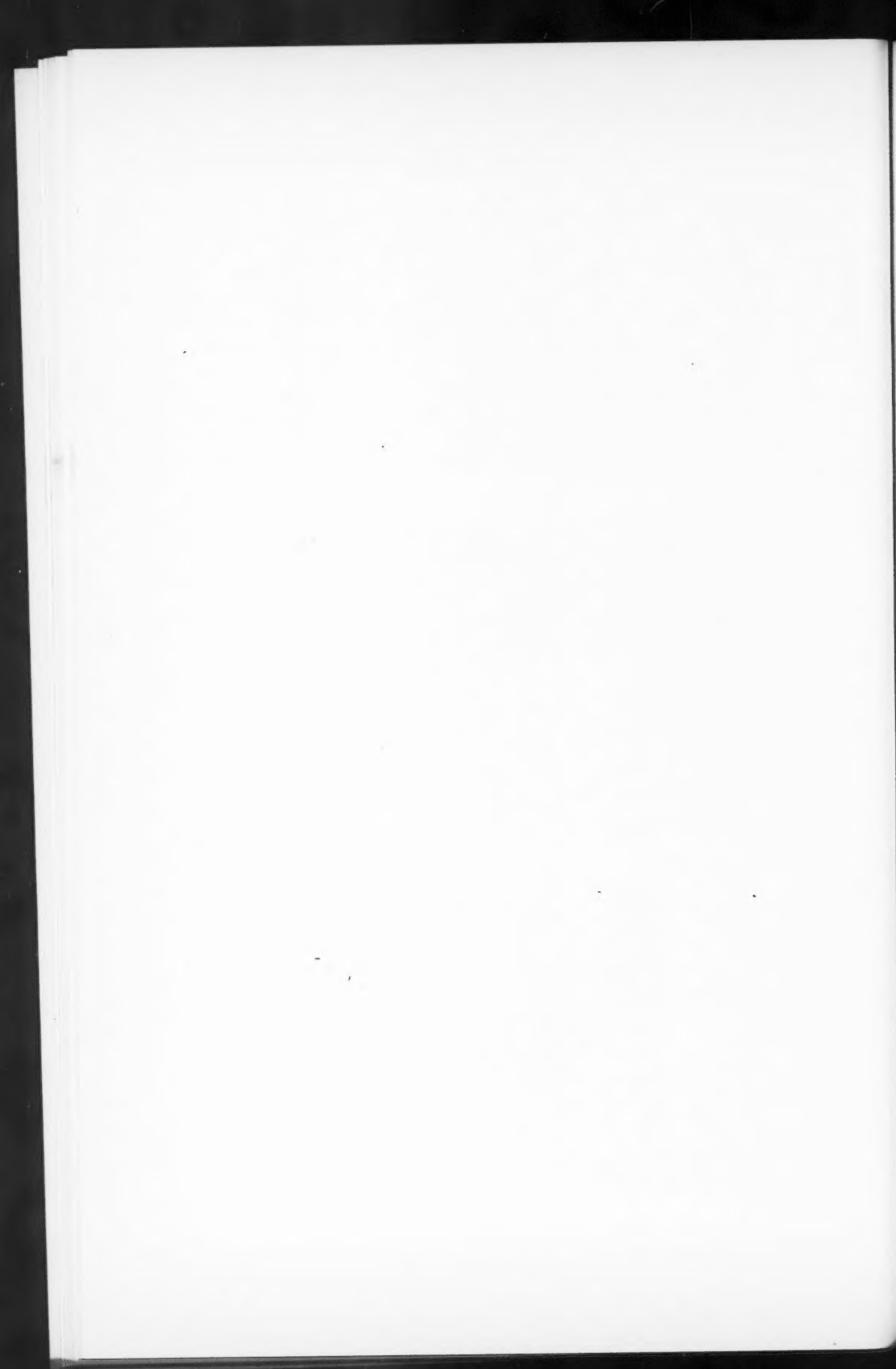


FIG. 1. Interference pattern observed, by reflected sodium light, on an optical flat originally placed near an electrode inside a tube carrying a high frequency discharge. FIG. 2. Photograph by transmitted sodium light showing two sets of fringes: (a) due to the original deposit on an optical flat; (b) due to multiple reflections in the narrow air gap between this flat and a second silvered flat nearly parallel. FIG. 4. Photograph of an interference pattern obtained by an air discharge in a polystyrene tube.



A typical set of values, taken for a film deposited on magnesium, is as follows:

<i>a</i>	<i>b</i>	Index = <i>a</i> / <i>b</i>	Deviation from mean
4.0	2.65	1.51	0.023
3.5	2.2	1.59	0.103
3.5	2.4	1.46	0.027
3.0	2.05	1.46	0.027
3.0	2.0	1.50	0.013
3.0	2.15	1.40	0.087
3.0	2.1	1.43	0.057
3.0	2.0	1.50	0.013
2.0	1.35	1.48	0.007
3.0	1.95	1.54	0.053
		Mean: 1.487	Meandev.: 0.041

Therefore, reliability of mean:  $\frac{0.041}{\sqrt{10}} = 0.013$

Index of refraction:  $1.487 \pm 0.013$ .

A series of three such groups of 10 readings was taken in each case, each group from a different photograph with the fringes at a different angle. These three figures were then averaged to give the final recorded value.

The index was also measured for a film obtained by running a discharge in a quartz tube, the value being  $1.487 \pm 0.006$ .

#### *Polystyrene Tubes*

With the deposit obtained in the polystyrene tube, such as is shown in Fig. 4, the index appeared to be abnormally low and a function of the thickness. A deposit of this type was left to stand for some four months, and the index again measured. Although the number of fringes due to reflection in the deposit was nearly the same before and after this period, the deposit shrank appreciably in volume, so that the index, while still a function of the thickness, was considerably greater than before shrinkage. The graph in Fig. 5 shows the index plotted as a function of the thickness before shrinkage.

A deposit was also obtained in a tube made from the new plastic 'Textolite'.<sup>\*</sup> In this case the index was also found to be very low (of the order of 1.37), but it has not yet been determined with sufficient accuracy to prove whether or not it is a function of thickness.

<sup>\*</sup> Trade name of a plastic manufactured by the General Electric Company, Plastics Division, Pittsfield, Mass.

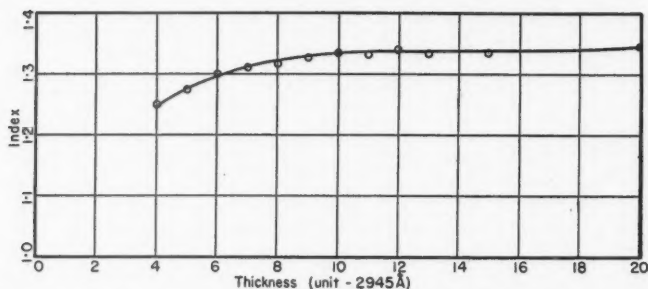


FIG. 5. Graph showing the variation of the index of refraction with thickness for a deposit formed in a polystyrene tube.

### Conclusions

The indices of refraction of deposits obtained in Pyrex glass and quartz tubes are identical, within experimental error, averaging about 1.487 for sodium light. This fact, coupled with its transparency and chemical inertness, strongly indicates that the deposit is silica in some form.

The *Handbook of Chemistry and Physics* gives the following forms of silica with the corresponding indices of refraction.

Cristobalite	1.487, 1.484
Lechatelierite	1.46
Quartz	1.544, 1.553
Tridymite	1.469, 1.470, 1.471
Amorphous, opal	1.41 - 1.46

The only index that falls within the limits of experimental error is that of cristobalite, which is almost exactly equal to the average value found in these experiments. It is not to be expected that the slight degree of anisotropism would be observable. Cristobalite is the form taken by silica crystallized at high temperatures. Sosman (4, p. 110) states that silica depositing from the gaseous state must be either micro-amorphous or cristobalite. The evidence is therefore strong that these deposits are silica in the form of cristobalite.

No such definite conclusion can be drawn as to the nature of the deposit formed in the polystyrene tube. That a new transparent organic solid could be created in the discharge is not probable, and we are forced to consider the deposit as basically polystyrene. Since, on the whole, hydrocarbons become more and more volatile as their molecules become less and less complex, the fact that this deposit withstood the high vacuum of the evaporating apparatus indicates that its molecules must be quite large.

Massive polystyrene, however, has an index of refraction of about 1.60, whereas, even after standing for four months, the maximum index of the deposit did not exceed 1.45. The shape of the curve in Fig. 5 indicates a sort of packing down process. It is explained most easily by considering the top layer of the deposit to be more open in structure, with index about 1.25, the

deposit becoming more compact with additional deposition until the index reaches about 1.35. With the passage of time the molecules gradually rearrange themselves into a more compact mass, so that the index increases. (Note that the indicometer does not measure average index. As has been pointed out above, the index that is measured is that of the material which varies in thickness. If, as is logical, the surface layer in the polystyrene deposit is uniform, the index that was measured is that of the *bottom* of the deposit.)

To get a tentative explanation of the very low index found, lower than that of any organic compound of which the writer has knowledge, it is necessary to examine the nature of the polystyrene polymer itself. The polystyrene molecules are very long and thin, and ordinarily these molecules are aligned. According to Staudinger (5) this alignment exists even in the amorphous state. Now if the individual polystyrene molecules, instead of being crystallized out of a solution, were thrown down at random like a handful of sticks, there would be a large number of open spaces in the material, and the index would be expected to be low. This hypothesis also makes probable the packing down action, suggested above.

On the basis of this hypothesis, the amount of open space in the deposit would be:

$$\frac{1.60 - 1.25}{1.60 - 1.00} = 58\% \text{ at the top,}$$

$$\frac{1.60 - 1.35}{1.60 - 1.00} = 42\% \text{ at the bottom before shrinkage, and}$$

$$\frac{1.60 - 1.45}{1.60 - 1.00} = 25\% \text{ at the bottom after shrinkage.}$$

These figures neither help, nor detract from, the hypothesis.

#### Acknowledgments

The writer wishes to thank Prof. J. K. Robertson, Head of the Department of Physics at Queen's University, at whose suggestion and under whose direction this problem was undertaken, and Mr. R. D. Bradfield who is responsible for the final design and construction of the indicometer. Thanks are also due to the National Research Council of Canada, whose generous award of a Studentship made the work possible.

#### References

1. GOODWIN, H. M. Elements of the precision of measurements. Geo. H. Ellis Co., Boston. 1905.
2. LODGE, J. I. and STEWART, R. W. Can. J. Research, A., 26 : 205. 1948.
3. ROBERTSON, J. K., STEWART, R. W., and LODGE, J. I. Nature, 158 : 703. 1946.
4. SOSMAN, R. B. The properties of silica. Chemical Catalogue Company, Inc., New York. 1927.
5. STAUDINGER, H. Ber. 62 : 2893. 1929.
6. TOLANSKY, S. Proc. Roy. Soc. London, A, 184 : 41. 1945.

## A COMPARISON OF THE X-RAY DIFFRACTION AND NITROGEN ADSORPTION SURFACE AREAS OF CARBON BLACKS AND CHARCOALS<sup>1</sup>

By J. C. ARNELL AND W. M. BARSS

### Abstract

The surface areas, as determined from X-ray diffraction and low temperature nitrogen adsorption data, were compared for a number of carbon blacks and activated charcoals. Comparative data were also obtained on samples of charcoal at various stages of activation and after calcination. The X-ray diffraction data indicated that all the samples examined were composed of small graphitelike crystallites of the same order of magnitude, which had specific surfaces of about 2500 to 3000 sq. m. per cc. The nitrogen adsorption surface of a highly activated charcoal was found to be about equal to the X-ray surface. It is suggested that the crystallite surface represents the potential adsorption surface of a carbonaceous material and, providing that crystal growth does not occur during activation, the activation process makes these surfaces available to external adsorbate.

### Introduction

The determination of the surface areas of activated charcoals and carbon blacks from nitrogen adsorption isotherms measured at the temperature of liquid air has been well tested (4; 5, pp. 1-36). A method of determining the ultimate particle (crystallite) size, and consequently the maximum surface area, of the same materials from X-ray powder photographs has been developed by Warren (8), based on the original formula of Scherrer (7). There have been, however, very few comparative measurements between the two methods.

During the recent war a few isolated results obtained in the United States indicated that the nitrogen adsorption surface of a highly activated charcoal was of the same order of magnitude as the surface calculated from X-ray diffraction data. More recently, Zettlemoyer and Walker (9) have found fairly good agreement between the two methods for active magnesia having a surface of 300 sq. m. per gm., but found that the nitrogen surface deviated below the X-ray surface in a regular manner as the surface decreased.

Considerable data are available for various types of carbonaceous materials ranging from carbon blacks (2) to coals and chars from various wood components (3, pp. 176-231; 6). These materials all appear to be made up of small graphitelike crystallites, characterized by a random layer lattice. In each crystallite the carbon atoms form two-dimensional plane hexagonal nets separated by essentially the same spacing as in graphite, but with random orientation about a normal to the layers. The carbon-carbon distances within

<sup>1</sup> Manuscript received March 13, 1948.

Joint contribution of the Defence Research Chemical Laboratories, Ottawa, and Physics Division, National Research Council, Ottawa, Canada. Published as D.R.C.L. No. 17 and N.R.C. No. 1777

the nets and between layers are remarkably constant for the many different kinds of carbonaceous materials studied and the same is also generally true for the crystallite dimensions.

Comparative data are presented here for a number of carbon blacks and activated charcoals, both in their original states and after heat treatment.

### Theoretical

As the individual crystallites of a substance become smaller than 1000 Å, the diffraction lines in its X-ray powder photograph progressively broaden. Scherrer proposed the following formula for calculating the average dimensions of simple cubic crystals (7):

$$L_c = \frac{0.94\lambda}{B \cos \theta}, \quad (1)$$

where  $L_c$  = average crystallite dimensions, perpendicular to the particular set of diffracting planes in the lattice, in Ångström units,

$\lambda$  = wave length of the X-radiation in Ångström units,

$B$  = angular width of the line at half its maximum intensity in radians, and

$\theta$  = Bragg angle of the diffraction maximum in degrees.

$B$  must be corrected for the instrument width, that is, the width of the half-maximum of the intensity curve for very large particles. This correction is usually applied in the following form:

$$B^2 = B'^2 - b'^2, \quad (2)$$

where  $B'$  = measured width of the half-maximum in radians, and

$b'$  = correction for instrument width in radians.

Other formulae have been derived by other workers, but all are of the same form as Equation (1), except that the numerical constant has varied from 0.89 to 1.0.

In identifying the diffraction maxima from carbonaceous materials, it is customary to use the Miller indices for a hexagonal system, such as are used for graphite, even though only limited types of reflection are possible because of the random orientation of the parallel hexagonal nets in the nongraphitized materials. The unit cell parameter,  $a$ , is the separation of the adjacent carbon atoms in a net and the parameter,  $c$ , is twice the separation of the parallel nets. Thus, the (00.2) diffraction halo is a normal three-dimensional effect to which the ordinary Scherrer formula applies, although Warren (8) recommends 0.89 as the best value for the constant. On the other hand, the (10) halo arises from the diffraction of the X-ray beam by the two-dimensional arrays of atoms in the hexagonal nets and is displaced in the direction of



smaller Bragg angles from the position of the three-dimensional (10.0) diffraction line of graphite. Warren has considered the case of such cross lattice lines and has derived the following formula in which the constant of the Scherrer equation becomes 1.84:

$$L_a = \frac{1.84\lambda}{B \cos \theta} \quad (3)$$

where  $L_a$  = average crystallite dimension across the plane of the hexagonal rings in Ångström units.

From the original Scherrer equation (with the constant equal to 0.89), the average crystallite dimension normal to the carbon layers,  $L_c$ , can be determined. From the  $\theta$  value corresponding to the position of the (00.2) halo, the distance between layers (i.e.,  $c/2$  = half the  $c$  axis of the unit cell) within the crystallite can be calculated from the Bragg equation.

$$\lambda = 2d_{c/2} \sin \theta, \quad (4)$$

where  $d_{c/2}$  = distance between layers within the crystallite.

The average crystallite dimension across the layers of carbon atoms,  $L_a$ , can be obtained from Equation (3). From the  $\theta$  value corresponding to the observed (10) halo may be subtracted a correction factor (8):

$$\Delta(\sin \theta) = 0.16\lambda/L_a, \quad (5)$$

which will give the  $\theta$  value corresponding to the (10.0) line of graphite. From this, in turn, the length of the  $a$  axis of the graphite unit cell can be calculated.

If the graphitelike crystallites are assumed to be cylinders having a diameter of  $L_a$  and a height of  $L_c$ , it is possible to calculate the specific surface of a collection of such cylinders. The specific surface is given by:

$$S_{p(X\text{-ray})} = \frac{2L_a + 4L_c}{L_a L_c} \times 10^4, \quad (6)$$

where  $S_{p(X\text{-ray})}$  = specific surface of the assumed cylindrical crystallites in square meters per cubic centimeter.

The procedures for determining the areas by nitrogen adsorption have been described many times recently (4; 5, pp. 1-36) and will not be repeated here. Nitrogen isotherms were obtained on evacuated samples at liquid air temperatures. The areas of the carbon blacks were calculated from BET plots (4, p. 153), while those of the charcoal samples were calculated from Langmuir plots (4, p. 71) as the isotherms showed no indications of multilayer formation. The surface area values were converted from area per unit weight to area per unit volume, by multiplying by the density as determined by X-ray diffraction.

## Results

The specific surfaces of a number of carbon blacks had been previously measured by three different methods (1): low temperature nitrogen adsorption, gas permeability measurements, and electron microscopy, and this study was

extended to include X-ray measurements. The new data are presented in Table I, along with the nitrogen surfaces.

TABLE I  
SPECIFIC SURFACES OF CARBON BLACKS

Carbon black	Spacings		Dimensions		Specific surface	
	$c/2$ , Å	$a_0$ , Å	$L_c$ , Å	$L_a$ , Å	X-ray, sq.m./cc.	Nitrogen, sq.m./cc.
Thermax	3.54	2.43	16.2	42.5	2350	14
Kosmos 20	3.53	2.40	15.0	37	2410	46
Kosmos 40	3.57	2.41	15.0	32	2580	80
Statex B	3.55	2.41	14.8	32.0	2600	93
Shawinigan	3.47	2.43	22.2	54.8	1630	94
Statex A	3.57	2.43	14.8	35.8	2470	145
Kosmobile 77	3.54	2.45	13.7	30.5	2770	200
Spheron 9	3.56	2.40	14.5	32.5	2610	225
Dixiedensed HM	3.57	2.40	14.9	29.6	2700	250
Kosmobile S	3.54	2.43	14.3	33.4	2580	290
Voltex	3.66	2.43	12.4	37	2700	1150
Neo Spectra Mk. II	3.52	2.41	16.0	42	2200	1650

In order to investigate the effect of heating on the crystallite size, samples of the Neo Spectra Mk. II carbon black were studied after heating for various periods of time in an evacuated quartz tube. The results are listed in Table II.

TABLE II  
SPECIFIC SURFACES OF NEO SPECTRA MK. II CARBON BLACK AFTER CALCINATION

Treatment	Spacings		Dimensions		Specific surface	
	$c/2$ , Å	$a_0$ , Å	$L_c$ , Å	$L_a$ , Å	X-ray, sq.m./cc.	Nitrogen, sq.m./cc.
None	3.52	2.41	16.0	42	2200	1650
3 hr. at 1200° C.	3.61	2.45	13.9	43.2	2370	1600
6 hr. at 1200° C.	3.65	2.44	14.3	49.1	2070	730
16 hr. at 1200° C.	3.68	2.41	—	—	—	710

This study was extended to include a number of activated charcoals. A commercial coconut charcoal was examined after various periods of steam activation and then the final charcoal sample (after eight days' steaming) was heated for various periods of time in an evacuated quartz tube before study. The results are given in Table III, together with similar data on calcined samples of two zinc chloride activated wood charcoals.

TABLE III

SPECIFIC SURFACES OF ACTIVATED CHARCOALS AT VARIOUS STAGES OF ACTIVATION AND AFTER CALCINATION

Treatment	Spacings		Dimensions		Specific surface	
	$c/2$ , Å	$a_0$ , Å	$L_c$ , Å	$L_a$ , Å	X-ray, sq.m./cc.	Nitrogen, sq.m./cc.
<i>Coconut shell charcoal (commercial samples)</i>						
After 1 day's steaming	3.64	2.43	12.6	40.3	2580	1120
After 3 days' steaming	3.72	2.45	11.1	43.8	2720	1550
After 5 days' steaming	3.67	2.44	11.5	51.4	2520	1820
After 7 days' steaming	3.68	2.44	10.9	45.6	2700	2210
After 8 days' steaming	3.79	2.44	10.4	49.0	2740	2750
2 hr. at 1000° C.	3.70	2.44	10.5	47.3	2750	2830
2 hr. at 1200° C.	3.71	2.44	10.5	50.9	2690	2320
6 hr. at 1200° C.	3.78	2.44	10.2	47.2	2810	2250
<i>ZnCl<sub>2</sub>-activated maple flour charcoal (laboratory sample)</i>						
None	3.74	2.45	10.7	26.8	3360	—
2 hr. at 1000° C.	3.70	2.43	10.8	27.2	3320	3150
2 hr. at 1200° C.	3.68	2.41	11.1	38.3	2870	3210
6 hr. at 1200° C.	3.78	2.45	9.9	48.9	2840	2950
<i>ZnCl<sub>2</sub>-activated wood charcoal (commercial sample)</i>						
None	3.70	2.44	11.8	42.7	2630	2400
3 hr. at 1200° C.	3.63	2.39	11.8	42.8	2630	2600
6 hr. at 1200° C.	3.58	2.41	11.4	42.1	2700	2500

### Discussion

All of the samples listed above show the same general values for the spacings between the carbon atoms in adjacent planes ( $c/2$ ) and in the hexagons ( $a_0$ ) and are in agreement with previously reported values (2; 3, pp. 176-231).

The carbon blacks and the activated charcoals all have very similar crystallite dimensions and, in consequence, the specific surfaces calculated for the crystallites are all of the same order. As there is fairly good agreement between the specific surfaces of highly activated charcoals, determined by low temperature nitrogen adsorption and from X-ray diffraction (Table III), it seems probable that the potential adsorbing surface of an activated carbon is the external surface of the small graphitelike crystallites, which apparently form the basis of all carbonized materials.

The samples of coconut shell charcoal at various stages of activation (Table III) all show the same X-ray specific surface, while the nitrogen adsorption surface increases as the activation proceeds. It is therefore possible to visualize the activation process as one that opens up the charcoal structure by the

PLATE I

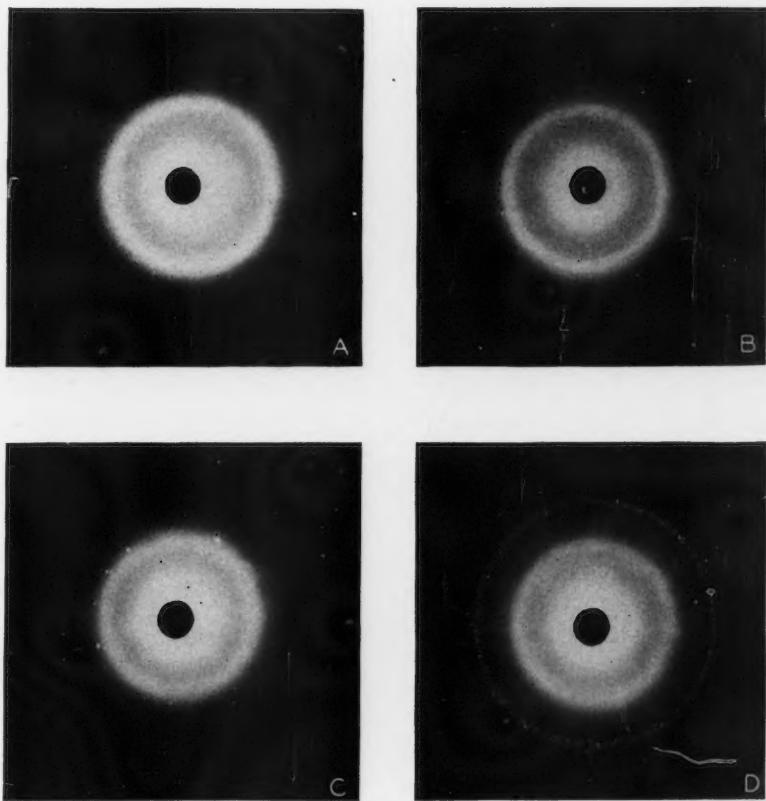
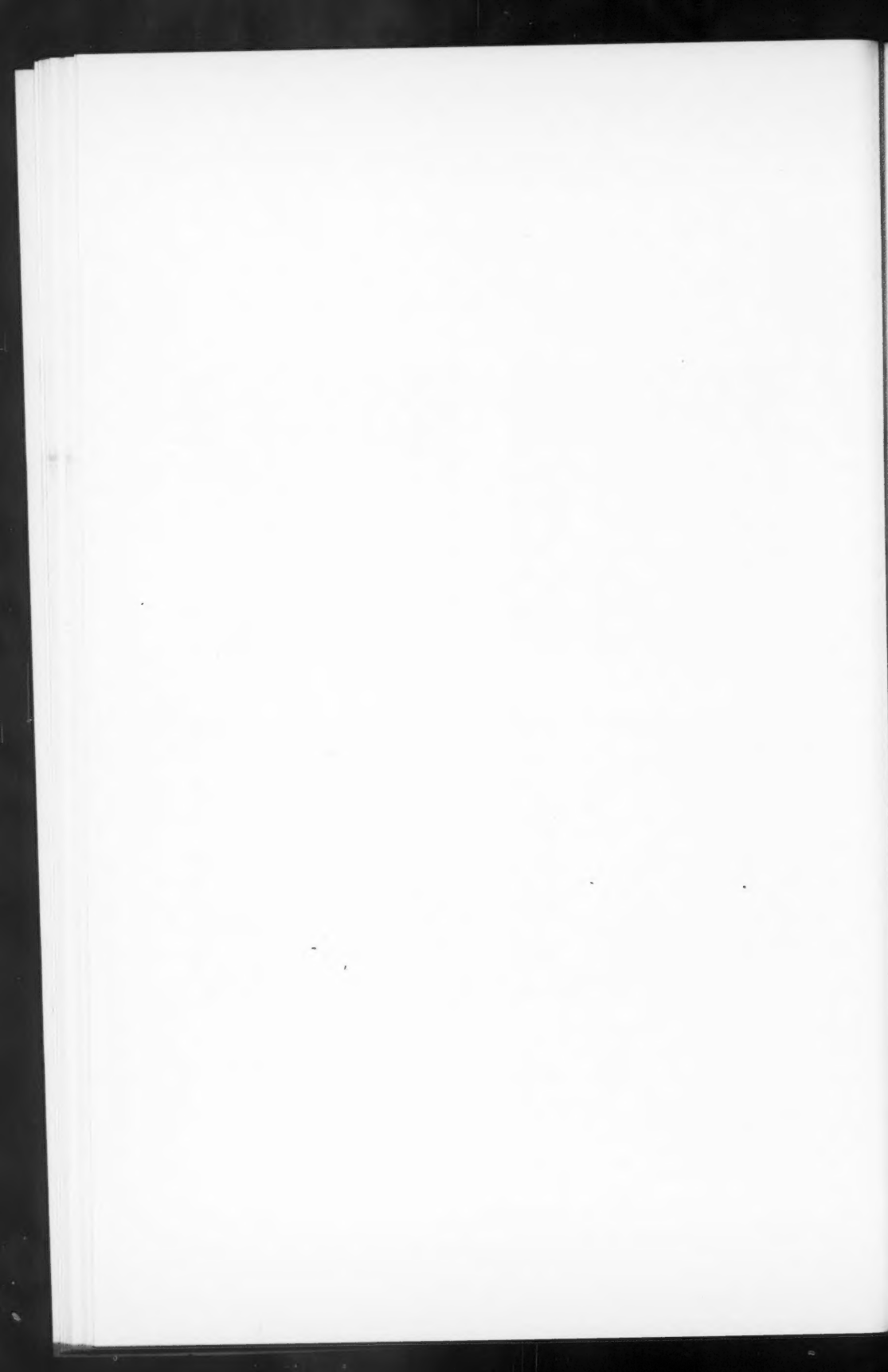


FIG. 1. X-ray diffraction photographs of Neo Spectra Mk. II carbon black. A. Original sample. B. Heated for three hours at 1200° C. C. Heated for six hours at 1200° C. D. Heated for 16 hr. at 1200° C.



removal of amorphous carbon from between the crystallites or by the separation of the crystallites due to thermal expansion during the heating process, followed by a subsequent contraction of the crystallites. Either process would allow the molecules of the adsorbate to reach the crystallite surfaces where adsorption takes place, without any necessity for change in the crystallite dimensions.

If this is the case, then it would appear that it should be possible to activate by heating with or without the use of a gas almost any material that consists essentially of carbon. Such activation, however, is not possible if the material tends to exhibit crystal growth under normal activating conditions. Biscoe and Warren (2) studied the effect of calcination on a sample of Spheron Grade 6 carbon black, and their results, which are reproduced in Table IV, show crystallite growth very clearly.

TABLE IV

EFFECT OF CALCINATION ON THE CRYSTALLITE DIMENSIONS OF SPHERON GRADE 6 CARBON BLACK

(After Biscoe and Warren (2))

Treatment	Spacings		Dimensions		Specific surface, sq.m./cc.
	$c/2$ , Å	$a_0$ , Å	$L_c$ , Å	$L_a$ , Å	
None	3.55	2.45	12.7	20.0	3570
2 hr. at 760° C.	3.52	2.42	14.4	22.6	3160
2 hr. at 1040° C.	3.47	2.46	14.9	28.0	2770
28 hr. at 1040° C.	3.55	2.43	14.9	29.8	2690
2 hr. at 1500° C.	3.48	2.44	24.9	44.2	1710
2 hr. at 2000° C.	3.46	2.44	32.3	55.8	1340
10 hr. at 2000° C.	3.47	2.43	35.5	60.5	1220
2 hr. at 2800° C.	3.45	2.46	40.0	65.2	1110

Neo Spectra Mk. II carbon black shows another example of crystal growth as a result of calcination. While the data in Table II show little change in the crystallite dimensions following the heating, which is more or less in line with the data in Table IV for the heating of Spheron Grade 6 carbon black at 1040° C., crystal growth does occur, however, as the nitrogen surfaces in Table II indicate, and is shown in the X-ray diffraction photographs of the four samples of Neo Spectra Mk. II carbon black, reproduced in Fig. 1. It can be seen in the photographs, that while little change occurs in the diffuse diffraction ring, discrete spots indicating macrocrystals are apparent in the photograph of the sample heated for six hours at 1200° C., and after 16 hr. heating at 1200° C., a sufficient number of macrocrystals have been formed to give the outlines of a new ring. The fact that this new ring is spotty, while the diffuse rings remain diffuse, suggests that crystal growth takes place at a relatively small number of 'centers' rather than throughout the aggregate.

On the other hand, the three activated charcoals show little change in either the crystallite dimensions or the nitrogen adsorption surface as a result of six hours' heating at 1200° C. The nitrogen adsorption surface of the coconut shell charcoal shows a slight decrease after calcination. This may or may not be significant.

### Conclusions

From the broad X-ray diffraction bands obtained on a number of activated charcoal samples, the crystallite dimensions of the graphitelike ultimate particles of the structure could be estimated. The specific surfaces, calculated from the crystallite dimensions, showed good agreement with the low temperature nitrogen adsorption surface for highly activated charcoals.

It is suggested that these crystallites form the adsorption surface of an activated carbon, and the activation process, by the removal of some of the material, opens the structure sufficiently for the adsorbate to diffuse to the crystallite surfaces.

As all carbonized materials show crystallites of similar dimensions, all might be considered as capable of activation. However, many substances, such as carbon blacks, exhibit marked crystallite growth under normal activation conditions and, in consequence, the potential adsorption surface disappears while the structure is being opened to make it accessible.

Activated charcoals show little crystallite growth on calcination and it would appear that resistance to such growth is the first requirement of a carbonized material suitable for high temperature activation.

### Acknowledgments

The authors would like to express their thanks to Dr. W. H. Barnes, Physics Division, National Research Council of Canada, for his helpful criticism and continued interest during the writing of this paper; to Miss Helen Jago for assisting in the X-ray diffraction work; and to Mr. G. O. Henneberry for his assistance in the determination of the nitrogen adsorption isotherms.

### References

1. ARNELL, J. C. and HENNEBERRY, G. O. *Can. J. Research, A*, 26 : 29. 1948.
2. BISCOE, J. and WARREN, B. E. *J. Applied Phys.* 13 : 364. 1942.
3. BLAYDEN, H. E., GIBSON, J., and RILEY, H. L. The ultrafine structure of coals and cokes. The British Coal Utilization Research Association, London. 1944.
4. BRUNAUER, S. The adsorption of gases and vapors. Princeton Univ. Press, Princeton, N.J. 1943.
5. EMMETT, P. H. *In Advances in colloid science*. Vol. 1. Edited by E. O. Kraemer. Interscience Publishers, Inc., New York. 1942.
6. RILEY, H. L. *Quarterly Revs. (Chem. Soc., London)* 1 : 59. 1947.
7. SCHERRER, P. *Nachr. Ges. Wiss. Göttingen*, 96. 1918. *Abstracted in Chem. Abstracts*, 13 : 2624. 1919.
8. WARREN, B. E. *Phys. Rev.* 59 : 693. 1941.
9. ZETTMEOYER, A. C. and WALKER, W. C. *J. Phys. Coll. Chem.* 51 : 763. 1947.

# MEASUREMENT OF THE ENERGIES OF $\alpha$ -PARTICLES<sup>1</sup>

BY T. E. CRANSHAW<sup>2</sup> AND J. A. HARVEY<sup>3</sup>

## Abstract

The energies of the  $\alpha$ -particles from weak preparations of several new radioactive substances were measured in a grid ionization chamber filled with argon. The accurately known energies of  $\alpha$ -particles from several well known sources were used for calibration. The voltage pulses produced by electron collection from the tracks were amplified in a linear amplifier of high stability and converted into flat-topped pulses. An accurately known voltage was subtracted, and the small residual pulses were further amplified. The frequency distribution of pulse sizes was recorded on an electronic pulse analyzer.

The final values of the energies are as follows:

$^{92}\text{U}^{233}$ ,  $4.823 \pm 0.003$ ;  $^{89}\text{Ac}^{225}$ ,  $5.801 \pm 0.010$ ;  $^{87}\text{Fr}^{221}$ ,  $6.298 \pm 0.010$ ;  $^{85}\text{At}^{217}$ ,  $7.023 \pm 0.010$ ;  $^{84}\text{Po}^{213}$ ,  $8.336 \pm 0.005$ ; and  $^{84}\text{Pu}^{239}$ ,  $5.159 \pm 0.005$  Mev.

The ionization-energy curve in argon was found to be linear within experimental error for  $\alpha$ -particles of energy 5 to 9 Mev. Extrapolation of this line determines an intercept of 85 kev. at zero ionization.

## Introduction

This paper describes a rather powerful method of measuring the energies of  $\alpha$ -particles from weak sources and its application to several new radioactive substances. Absolute measurements were derived with the aid of  $\alpha$ -particles of accurately known energies. The principles involved are (1) that the total ionization produced in a gas by an  $\alpha$ -particle is very nearly proportional to its initial energy, and (2) that the electron pulse from the ionization in an argon-filled grid chamber is nearly proportional to that ionization. The principal advantage over other methods of measuring the energies of  $\alpha$ -particles is that a large surface area (several square centimeters) of source and a large solid angle for  $\alpha$ -particle emission can be used. The method adopted here is therefore particularly suitable for long-lived elements, which have low specific activities.

The resolving powers of the various methods for measuring the energies of  $\alpha$ -particles differ considerably. The highest resolution is obtained in the magnetic spectrograph, such as that used by Chang (3), where the width of the line at half-maximum was about 10 kev. On the other hand, only one  $\alpha$ -particle in about 5000 reaches the detector, and the source is limited to a small area. Usually, some of this resolution is sacrificed for greater utilization of the source, and the width at half-maximum may then reach 30 kev. With the grid chamber used in the present work and a source of polonium 210, the width of the line at half-maximum was ultimately reduced to 50 kev. (1).

<sup>1</sup> Manuscript received March 6, 1948.

Contribution from the Nuclear Physics Branch, Montreal Laboratory, Atomic Energy Division of the National Research Council of Canada. Issued as N.R.C. No. 1776. This work was done in 1945 and the essential results listed in Report CRC-269 of the National Research Council.

<sup>2</sup> United Kingdom Staff; now at the Cavendish Laboratory, Cambridge University, Cambridge, England.

<sup>3</sup> Now at the Massachusetts Institute of Technology, Cambridge, Mass.



### Ionization Chamber

The ionization chamber contained two plane parallel electrodes, 10 cm. square and 6 cm. apart, with a grid of parallel wires placed 1.4 cm. from the electron-collecting electrode. The wires in the grid were 0.10 mm. in diameter (No. 38 gauge) spaced 2 mm. apart. In another paper (1) it will be shown that this grid is adequate for shielding the electron-collecting electrode from the induced effect of the slowly moving, positive ion component of the ionization. A negative potential of 1200 v. was applied to the high tension electrode, which produced a field sufficient to collect all the electrons from the track of an  $\alpha$ -particle. The potential of the grid was chosen so that it did not collect electrons (1). The chamber could be filled with argon (99.8% pure) to a pressure of 3 atm.

A small hinged platinum plate was attached to the negative electrode. The source of  $\alpha$ -particles whose energy was to be measured was mounted on one side of the plate, and the two standard sources of  $\alpha$ -particles chosen for comparison were mounted on the other side. By rotating the chamber the hinged plate could fall over and take up either of two positions close to the negative electrode. Thus the  $\alpha$ -particles from the 'unknown' source and the standards could be analyzed alternately under identical conditions.

The source on each side of the hinged plate was covered with a simple collimator, which was a sheet of 1/32 in. aluminum drilled with 1/8 in. holes. Without the collimator the distribution of pulse sizes was not symmetrical about the maximum but had a tail on the low energy side. These small pulses may have been caused by  $\alpha$ -particles that had lost an appreciable amount of energy in the source and those scattered backwards from the support with energy loss.

### Electronic Equipment

The voltage pulses produced on the collector were amplified in a linear amplifier of high stability to a level of about 50 v. and converted into flat-topped pulses. An accurately known voltage was then subtracted, and the small residual pulses underwent further amplification. A distribution of frequency of occurrence against size was then obtained using a pulse analyzer ('kicksorter') (6).

#### (a) Linear Amplifier

In order to obtain a high signal-to-noise ratio the head amplifier was mounted directly on to the ionization chamber. This amplifier is shown in Fig. 1. It consists of a high-gain low noise triode that feeds through a cathode-follower, the cathode load of which is mounted inside the main amplifier and used as a stepped gain-control. The triode operates with feedback through the grid-anode capacity and this gives a stabilized gain of about 10 times.

The main amplifier, shown in Fig. 2, is made up of two similar stages; each a three-tube ring circuit with a gain of 200. The very large negative feedback round the ring ensures high gain-stability and accurately linear amplification.



The pulse at the output of the linear amplifier (a cathode-follower) has, then, an exponential rise and fall adjustable by the bandwidth control. In this experiment the time constants used were respectively 5 and 25  $\mu\text{sec}$ .

(b) *Cutoff Amplifier*

It has previously been remarked that the spread in amplitude of the pulses produced was only about 1%. To obtain an accurate value for the mean pulse height it is clearly desirable to extend this spread over a considerable part of the working range of the pulse analyzer (50 to 150 v.).

A simple biased amplifier that amplifies the difference between the pulses at the output of the linear amplifier (say 49 to 51 v.) and a bias level of 48 v. would not, however, be satisfactory. The residual pulses undergoing amplification would clearly be very short, necessitating a very wide-band amplifier. Furthermore, the length of a residual pulse would vary rapidly with the amplitude of its parent pulse. With any reasonably attainable bandwidth (and the already relatively fast pulses at the amplifier output) there would be in consequence an appreciable non-linearity, the smaller, shorter residual pulses being amplified less than the larger, longer ones.

This difficulty is removed if the parent pulses are rectangular in shape—the residual pulses are then of equal length independent of their amplitude, and the effect of a finite amplifier bandwidth is the same on all.

This shaping is accomplished by the first part of the cutoff amplifier circuit shown in Fig. 3. A cathode-coupled Kipp relay  $V_1$ ,  $V_2$  produces a square wave of amplitude 100 v. and adjustable duration (40 to 2000  $\mu\text{sec}$ .) from any input pulse of amplitude greater than about 13 v. This positive square wave is applied to the grid of the cathode-follower  $V_4$  and cuts off the diode  $D_4$ . This allows the condenser  $C$  to charge through the diode  $D_3$  to the peak amplitude of the input pulse, which is applied to  $D_3$  through a cathode-follower  $V_3$ .

The condenser  $C$  retains this charge until the recovery of the Kipp relay swings  $V_4$  cathode to earth potential and discharges  $C$  through  $D_4$ . A very small fraction of the charge on  $C$  leaks away through  $R$ , but the fall in potential during the length of the square wave required is negligible.

The detailed behavior of the diode condenser-charging circuit is somewhat involved. Owing to the imperfect cutoff characteristics of diodes the exact level to which the cathode rises depends on the input pulse shape and the size of the reservoir condenser used. A small hump is produced owing to the diode self-capacity. Provided that  $C$  is small enough to avoid saturation of  $D_3$  or  $V_3$ , these are second-order effects and reduce to two terms—a constant and a term proportional to the input pulse; that is, a small 'zero-error' plus a small change in the gain. (The latter is still independent of pulse amplitude.) The 'zero error' and gain were determined experimentally (see below) using pulses of exactly similar shape.

Tube  $V_5$  is merely a buffer stage to isolate  $C$  and  $R$ . The bias voltage is subtracted from the now square pulse on the grid of  $V_6$ . The diode  $D_5$  passes only that part of the pulse above earth potential, that is, the difference between

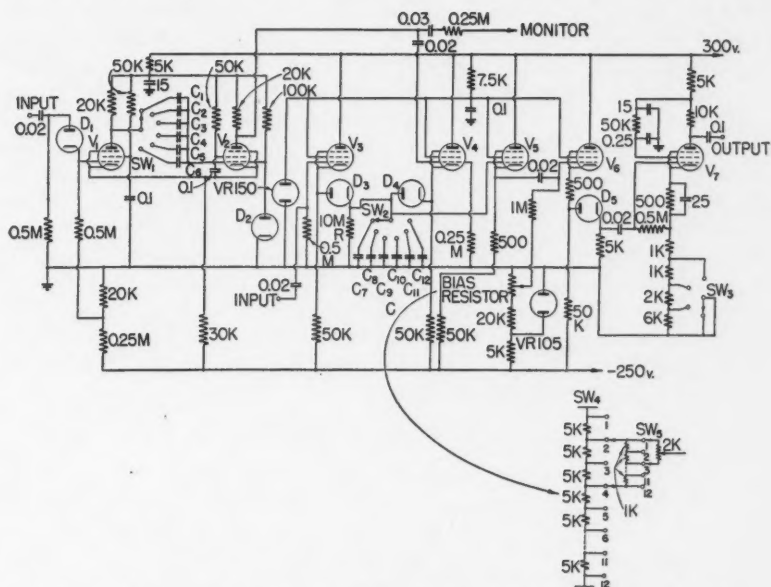


FIG. 3. Cutoff amplifier. Tubes  $V_1$  to  $V_7$  are 6AC7's;  $D_1$  to  $D_5$  EA 50's. Resistances are shown in ohms, capacities in microfarads. Further components are as follows:  $C_1$ , 0.005;  $C_2$ , 0.002;  $C_3$ , 0.001  $\mu$ f.;  $C_4$ , 500;  $C_5$ , 200;  $C_6$ , 100  $\mu$ f.;  $C_7$ , 0.01;  $C_8$ , 0.005;  $C_9$ , 0.002;  $C_{10}$ , 0.001  $\mu$ f.;  $C_{11}$ , 500;  $C_{12}$ , 200  $\mu$ f.

the input pulse amplitude and the bias voltage, plus a 'zero-error' due to the grid bases of the cathode-follower tubes. The numerical value of this is reduced by the insertion of a 500-ohm resistor in the cathode circuit of  $V_6$ . The diode  $D_5$  operates linearly at outputs greater than about  $\frac{1}{3}$  v.

The bias voltage is obtained from a potentiometer chain consisting of 11 selected 5K wire-wound resistors, not differing by more than one ohm, connected in series. To equalize these to an accuracy of better than 1/100% they are shunted by selected resistors of nominal value 2 Megohms. Eleven selected 1K wire-wound resistors are connected in series, and by means of a switch can be connected across any two consecutive 5K resistors. Similarly a 2K wire-wound potentiometer can be connected across any two consecutive 1K resistors. With this bias arrangement it is possible to obtain bias voltages whose relative values are accurate to 1/100%.

$V_7$  is simply an output tube stabilized by negative feedback. Its gain can be adjusted in four convenient steps. It feeds directly into the pulse analyzer. A description of this instrument has been published (6).

### Sources

The activity of the sources was of the order of a few hundred counts per minute. They were prepared by evaporating drops of the active substances in solution on to gold or platinum foils. The energies of the  $\alpha$ -particles used for calibration were taken from Seaborg's Table (12) and are listed in Table I. The energies of the  $\alpha$ -particles from four members of the  $(4n + 1)$ -series\* were known to be about 5.8, 6.3, 7.0, and 8.3 Mev. from earlier work in this laboratory. For their precise measurement, sources of thorium active deposit and polonium 210 were used to give reference energies. The energy of the  $\alpha$ -particles from uranium 233 (13) was measured by comparison with the  $\alpha$ -particles from radium 226 and polonium 210. For plutonium 239 the standards were radium 226 and radon 222. The ionization-energy curve was determined with the  $\alpha$ -particles from three sources—radium 226 and its products, thorium active deposit, and polonium 210. In this case the thorium active deposit and polonium were mounted on one side of the hinged plate, and the radium source on the other side. This arrangement prevented overlap of the pulse distributions due to  $\alpha$ -particles at 5.998 and 6.054 Mev., also at 5.298 and 5.486 Mev. (Table I).

TABLE I  
ENERGIES OF  $\alpha$ -PARTICLES USED FOR CALIBRATION

Element	Mass number	Energy of $\alpha$ -particle, Mev.
Radium	226	4.791
Polonium	210	5.298
Radon	222	5.486
Radium A	218	5.998
Thorium C	212	6.054
Radium C'	214	7.680
Thorium C'	212	8.776

### Experimental Procedure

#### (a) Method 1

In the first method the gain and bias on the cutoff amplifier were chosen so that the pulses from the two standard sources, bracketing the 'unknown' source, were counted on the pulse analyzer in two groups of channels close to the ends of the bank of 20 channels. For instance, when the energy of the  $\alpha$ -particles from uranium 233 (known to be about 4.8 Mev.) was to be measured, radium 226 and polonium 210 were used as standards. The middles of the pulse distributions for radium and polonium  $\alpha$ -particles occurred at channels Nos. 5 and 17 respectively. By inverting the ionization chamber,

\* The chain of decay products of uranium 233, which form part of the new  $(4n + 1)$  radioactive series, was discovered independently by English et al. (4, 5) of the Montreal Laboratory and Hagemann et al. (10) of the Argonne Laboratory. The present paper contains a detailed portion of this work at the Montreal Laboratory, which was summarized in a brief publication (5).

alternate runs could be taken on the  $\alpha$ -particles from uranium 233. By linear interpolation the energy of these  $\alpha$ -particles was derived. The results of a typical run are plotted in Fig. 4.

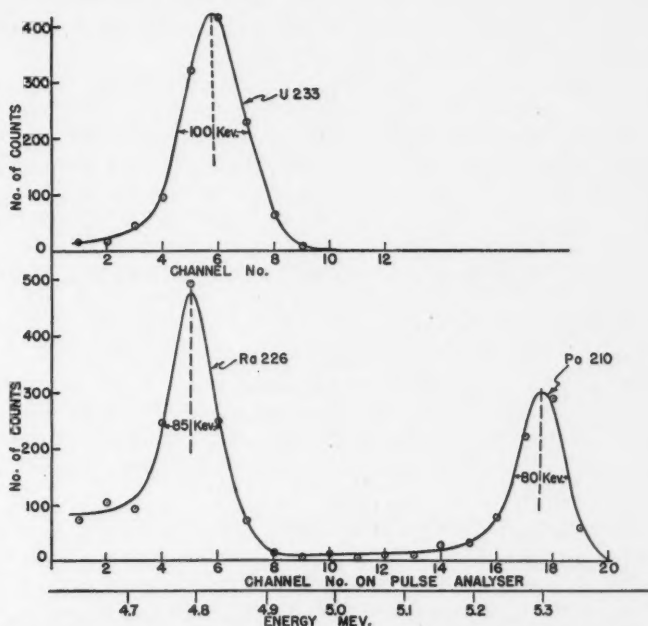


FIG. 4. Typical distributions on pulse analyzer, taken in Method 1. The dotted lines are the loci of the mid-points of the diameters. Upper curve:  $\alpha$ -particles from uranium 233, peak at channel 5.75. Lower curves:  $\alpha$ -particles from radium 226 and polonium 210, peaks at channels 5.0 and 17.6. Energy of uranium 233  $\alpha$ -particle =  $4.791 + (5.298 - 4.791) 0.75/12.6 = 4.821$  Mev.

The linearity of response of the equipment was checked by feeding into the head amplifier 20 different-sized groups of artificial pulses. However, since each distribution of  $\alpha$ -particle pulses covers only two or three channels, a small error in the threshold of one of the relevant channels would make a large error in judging the position of the middle of the distribution. For accurate work this method was therefore abandoned. It should be noted, however, that the method is useful when the  $\alpha$ -particle spectrum is almost unknown, for a wide range of energy can be quickly scanned. It is also convenient for identifying several peaks of  $\alpha$ -particles through a study of their decay with time.

#### (b) Method 2

In the second method the gain of the amplifiers was held fixed as in Method 1, but the bias voltage of the cutoff amplifier was varied to bring each distribution of  $\alpha$ -particle pulses to the central position on the pulse analyzer (see below).



The gain of the cutoff amplifier could be chosen five times that used in Method 1. Consequently, the distributions covered more channels of the analyzer, and errors due to imperfections in the settings of the channels were correspondingly reduced. Moreover, since there were about eight points on each distribution curve, drifts in individual channels were revealed by irregularities showing in the curve.

The relation between the bias of the cutoff amplifier and the energy of the  $\alpha$ -particles chosen as standards was investigated. Small deviations of the peaks from the chosen channel of the analyzer were measured, and corrections were applied to the bias reading. In order to make these corrections the relation between bias voltage and position of the distribution for input pulses of constant size was required. This was determined by feeding in uniform pulses from a generator and locating the positions of the distribution on the pulse analyzer for different bias settings. The number of the channel was plotted against the bias to give a straight line of required slope. The linear relation between bias and energy of  $\alpha$ -particles was then used to determine the energy of the  $\alpha$ -particles from the substance under investigation.

In order to find the position of most probable size in the distribution of  $\alpha$ -particle pulses, the method of diameters was used. The distribution curve was drawn, and the point at which the locus of the mid-points of diameters intersected this curve was taken as the most probable size. An example is shown in Fig. 5.

In the investigation of the ionization-energy curve it was necessary to determine the bias threshold, i.e., the value of the bias that corresponds to zero pulse size. Ten groups of artificial pulses, whose amplitudes were in the ratio 1 : 2 : 3 : . . . 10, were fed through a small condenser to the input grid of the head amplifier. The bias necessary to bring each group in turn to the level of the standard channel was measured. The straight line plot of the bias against pulse size was extrapolated to zero size to yield the zero of the bias system.

### Experimental Results

The experimental runs were usually 5 or 10 minutes each, and about 1000  $\alpha$ -particles were counted in each distribution. In the measurements with uranium 233, twenty-five runs were taken on both standards and 'unknown'. For the other members of the  $(4n + 1)$ -series, six runs each, and for plutonium 239, ten runs were taken. The final energies of the  $\alpha$ -particles with the probable errors of the means are given in Table II.

Since these measurements were made, the signal-to-noise ratio was increased by a factor of nearly three, and the width of the polonium 210 line at half-maximum reduced to 50 kev. (1). About 40 kev. of this spread is due to noise and about 35 kev. due to thickness of source and straggling of ionization. With a new chamber of lower capacity and optimum selection of tubes the spread due to noise could likely be further reduced by the factor 2. Moreover,

thinner and more uniform sources and perhaps a more suitable gas could be used. With these improvements the width of a line such as that of polonium 210 could possibly be reduced to 30 kev. at half-maximum.

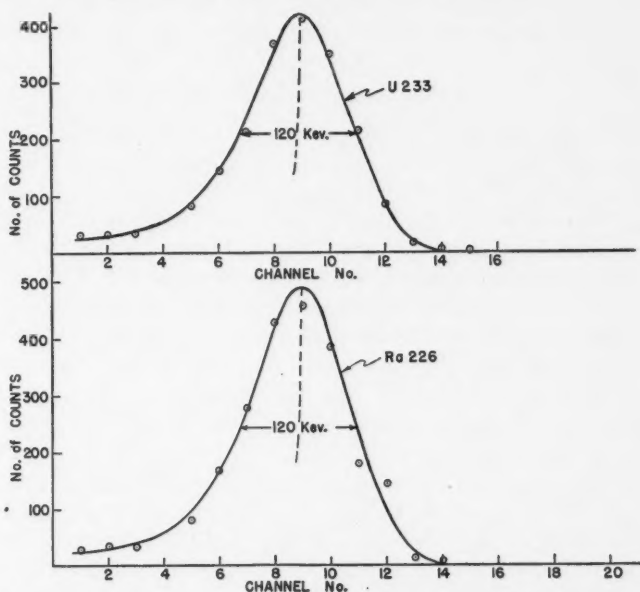


FIG. 5. Typical distributions on pulse analyzer, taken in Method 2. The dotted lines are the loci of the mid-points of the diameters. Upper curve:  $\alpha$ -particles from uranium 233, peak at channel 9.0, bias 8,075. Lower curve:  $\alpha$ -particles from radium 226, peak at channel 9.0, bias 8,015. The peak of the distribution of  $\alpha$ -particles from polonium 210 is at channel 9.0 when the bias is 8,960. A shift of 1 channel is caused by 54 bias units or 29 kev. in  $\alpha$ -particle energy. Energy of uranium 233  $\alpha$ -particle =  $4.791 + (5.298 - 4.791) 60/945 = 4.823$  Mev. (10,000 bias units correspond to 50 K, the maximum available in the bias resistor, or to  $\frac{50}{70} \times 105$  v. = 75 v.)

TABLE II  
DERIVED ENERGIES OF  $\alpha$ -PARTICLES

Substance	Energy, Mev.	Substance	Energy, Mev.
$^{92}\text{U}^{233}$	$4.823 \pm 0.003$	$^{85}\text{At}^{217}$	$7.023 \pm 0.010$
$^{89}\text{Ac}^{225}$	$5.801 \pm 0.010$	$^{84}\text{Po}^{213}$	$8.336 \pm 0.005$
$^{87}\text{Fr}^{221}$	$6.298 \pm 0.010$	$^{94}\text{Pu}^{239}$	$5.159 \pm 0.005$

The energy of the  $\alpha$ -particles of plutonium 239, measured in the present experiment, may be compared with that derived from their mean range in air, measured by Chamberlain, Gofman, Segrè, and Wahl (2). This is 3.675



cm. relative to a mean range of 3.842 cm. for the  $\alpha$ -particles from polonium 210. Stout and Jones (15) have derived 5.144 Mev. for the energy of the plutonium  $\alpha$ -particle from these ranges and the range-energy relation of Holloway and Livingston (11). This value is in reasonable agreement with  $5.159 \pm 0.005$  Mev. found in the present experiment.

### Ionization-Energy Curve

The ionization pulse sizes were measured for the  $\alpha$ -particles from the seven radioactive substances given in Table I, which cover the energy range 5 to 9 Mev. The pulse size was found to vary linearly to 0.1% with the energy of the  $\alpha$ -particles, using the method of least squares. Artificial pulses of 10 different amplitudes in the ratio 1 : 2 : 3 : . . . . 10 were fed into the amplifier and their output size against input size was linear to 0.1%. From these two straight lines the ionization-energy line was drawn, which extrapolates to the energy axis with an intercept of 85 kev. in argon. This value was the mean of three separate experiments, each with two determinations of pulse size, and its probable error is 10 kev. The intercept on the energy axis is taken as an indication that the ionization-energy relation is curved for low values of the  $\alpha$ -particle energy.

The average energy  $W$  in electron volts spent in producing an ion pair in a gas traversed by an  $\alpha$ -particle has been the subject of numerous investigations. L. H. Gray (8) has summarized the work up to 1942. He has, in effect, interpolated for  $W$  for various initial energies of the  $\alpha$ -particle in air on the basis of a modified Gerbes formula. Gerbes (7) measured the total ionization produced in air by initially monokinetic electrons over the range 300 to 60,000 ev. He observed a progressive increase in  $W$  with decreasing energy of the electrons that is well represented by the formula:

$$W = 31.62 + \frac{5.27}{\sqrt{E - E_i}} \pm 0.08 \text{ ev. per ion pair,} \quad (1)$$

where  $E$  is the initial energy of the electron in kev. and  $E_i$  is the ionization potential ( $1.7 \times 10^{-2}$ ) in kev. Gray calculated the total ionization produced by an  $\alpha$ -particle of given initial energy on the assumptions that both the primary ionization and the secondary  $\delta$ -ray ionization are represented by a formula of the Gerbes type. Best agreement with experiment was obtained by changing the second constant of Equation (1) from 5.27 to 2.6.

We find that Gray's adjusted data for the average energy loss  $W$  per ion pair produced in air by an  $\alpha$ -particle of initial energy  $E$  in Mev. can be satisfactorily represented by the formula:

$$W = 32.75 + \frac{6.5}{\sqrt{E}}. \quad (2)$$

This formula is particularly applicable in the region 2 to 8 Mev. It gives 35.1 and 35.6 ev. per ion pair for the  $\alpha$ -particles of radium C' (7.680 Mev.) and polonium (5.298 Mev.) respectively. These are in good agreement with the measurements prior to 1943 reviewed by Gray, and with the measurements from Stetter's laboratory (14). From the latter work  $W = 7.680 \times 10^6 / 220,300 = 34.9$  and  $W = 5.298 \times 10^6 / 148,200 = 35.7$  ev. per ion pair for these  $\alpha$ -particles.

A formula of the type shown by Equation (2),

$$W = A + \frac{B}{\sqrt{E}}, \quad (3)$$

can be tried for the ionization of an  $\alpha$ -particle of initial energy  $E$  in argon. Suitable values of the constants  $A$  and  $B$  have to be determined. Let  $I_1$  and  $I_2$  represent respectively the total number of ion pairs produced in argon by  $\alpha$ -particles of initial energies  $E_1$  and  $E_2$ . The average energy losses per ion pair are given by

$$W_1 = \frac{E_1}{I_1} \quad \text{and} \quad W_2 = \frac{E_2}{I_2}. \quad (4)$$

Choosing  $E_1 = 5$  Mev. and  $E_2 = 8$  Mev. and noting the linear relation found in the present experiments,

$$\frac{I_2}{I_1} = \frac{8.00 - 0.085}{5.00 - 0.085} = 1.6104.$$

From these relations

$$\frac{W_1}{W_2} = 1.0065 \quad \text{and} \quad \frac{A}{B} = 14.1.$$

Stetter (14) quotes 186,200 and 148,200 for the numbers of ion pairs produced in argon and air respectively by a polonium  $\alpha$ -particle. The former leads to  $W = 28.5$  ev. per ion pair, while the ratio is 1.256. Using Equation (2) as a good representation of Gray's adjusted data for air and this ratio, it follows that  $W = 28.3$  ev. per ion pair for a polonium  $\alpha$ -particle traversing argon. Adopting the latter value of  $W$  at  $E = 5.298$  Mev., the best values of the constants for argon that can be derived from the present experiments are

$$A = 27.5 \quad \text{and} \quad B = 1.9, \\ \text{or } W = 27.5 + \frac{1.9}{\sqrt{E}}. \quad (5)$$

The agreement of our results with the classical measurements of Gurney (9) appears reasonably close. There is some uncertainty about the exact energies of the  $\alpha$ -particles in Gurney's experiments, and these were concerned with  $\alpha$ -particles of lower energy than in our experiments. The ratio of the ioniza-

tion in argon to that in air, measured by Gurney, is about 3 to 4% higher than the ratio predicted by Equations (2), (4), and (5) over the range of energy he observed.

### Acknowledgments

The authors wish to thank Mr. A. C. English for preparing the radioactive sources, and Dr. B. W. Sargent and Mr. G. C. Hanna for assistance in preparing this paper for publication.

### References

1. BUNEMANN, O., CRANSHAW, T. E., and HARVEY, J. A. Unpublished report, CRP-247. The use of grid chambers for  $\alpha$ -ray analysis. National Research Council of Canada. 1946. (Report to be published.)
2. CHAMBERLAIN, O., GOFMAN, J. W., SEGRÈ, E., and WAHL, A. C. Phys. Rev. 71 : 529. 1947.
3. CHANG, W. Y. Phys. Rev. 69 : 60. 1946.
4. ENGLISH, A. C. Unpublished report, MC-145. The  $(4n + 1)$  radioactive series. National Research Council of Canada. 1945.
5. ENGLISH, A. C., CRANSHAW, T. E., DEMERS, P., HARVEY, J. A., HINCKS, E. P., JELLEY, J. V., and MAY, A. N. Phys. Rev. 72 : 253. 1947.
6. FREUNDLICH, H. F., HINCKS, E. P., and OZEROFF, W. J. Rev. Sci. Instruments, 18 : 90. 1947.
7. GERBES, W. Ann. Physik, 23 : 648. 1935.
8. GRAY, L. H. Proc. Cambridge Phil. Soc. 40 : 72. 1944.
9. GURNEY, R. W. Proc. Roy. Soc. London, A, 107 : 332. 1925.
10. HAGEMANN, F., KATZIN, L. I., STUDIER, M. H., GHIORSO, A., and SEABORG, G. T. Phys. Rev. 72 : 252. 1947.
11. HOLLOWAY, M. G. and LIVINGSTON, M. S. Phys. Rev. 54 : 18. 1938.
12. SEABORG, G. T. Rev. Modern Phys. 16 : 1. 1944.
13. SEABORG, G. T., GOFMAN, J. W., and STOUGHTON, R. W. Phys. Rev. 71 : 378. 1947.
14. STETTER, G. Z. Physik, 120 : 639. 1943.
15. STOUT, J. W. and JONES, W. M. Phys. Rev. 71 : 582. 1947.

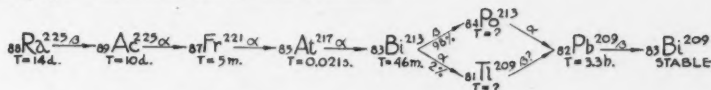
MEASUREMENT OF THE HALF-PERIOD OF POLONIUM 213<sup>1</sup>BY J. V. JELLEY<sup>2</sup>

## Abstract

In the recently discovered  $(4n + 1)$  radioactive series, bismuth 213 transforms to polonium 213 by  $\beta$ -emission. The latter rapidly transforms by  $\alpha$ -emission to lead 209. The present paper describes a measurement of the half-period of polonium 213. A preparation of radium 225 was placed between two Geiger-Müller counters. One detected  $\beta$ -particles while the other detected  $\alpha$  and  $\beta$ -particles. Coincidences were counted with a modified Rossi circuit. The pulse-width on the grid of one of the tubes of the coincidence unit was made variable, while the pulse-width on the other remained fixed. The pulse-width associated with the counter that responded only to  $\beta$ -particles was chosen to be variable. Coincidences were counted as a function of the pulse-width. Corrections were made for accidental coincidences and exact coincidences arising from other causes. The final value for the half-period  $T$  of polonium 213 is  $T = 4.2 \pm 0.8 \mu\text{sec}$ . A subsidiary experiment to determine the half-period of thorium C' gave the value  $T = 0.34 \pm 0.06 \mu\text{sec}$ , in reasonable agreement with measurements by other workers.

## Introduction

In the recently discovered  $(4n + 1)$  radioactive series (7, 8, 9) there occurs a short-lived  $\alpha$ -active body that occupies a position in the series similar to those of radium C', thorium C' and actinium C' in the other three radioactive series. This body is polonium 213, which is produced by the  $\beta$ -decay of bismuth 213 and transforms by  $\alpha$ -decay to lead 209. The relevant portion of the series proceeds as shown in Fig. 1 (7). It was clearly of interest to measure the half-period of polonium 213 and to see whether it shows a departure from the Geiger-Nuttall relation similar to those for the C' bodies. This paper describes such a measurement.

FIG. 1. Part of the  $(4n + 1)$  radioactive series.

From the known energy of the  $\alpha$ -particles (3, 8) and the Geiger-Nuttall relation, the half-period was estimated to lie in the region of microseconds or milliseconds. The coincidence method of measuring short periods could therefore be readily applied (5, 11). Two Geiger-Müller counters were used to detect the  $\beta$ -particles from bismuth 213 and the  $\alpha$ -particles from polonium 213. The pulses from the counters were applied to a coincidence amplifier with a variable resolving time. The coincidence counting rate was measured as a

<sup>1</sup> Manuscript received March 6, 1948.

Contribution from the Nuclear Physics Branch, Montreal Laboratory, Division of Atomic Energy of the National Research Council of Canada. Issued as N.R.C. No. 1775. This work was done in 1945 as part of the investigations on the  $(4n + 1)$  radioactive series, and was described in Report PD-165, dated December 10, 1945.

<sup>2</sup> United Kingdom Staff; now at the Cavendish Laboratory, Cambridge University, Cambridge, England.

function of the resolving time. Corrections were applied for (1) the accidental coincidence rate, and (2) exact coincidences arising from other causes.

### Geiger-Müller Counters

A Geiger-Müller counter was used for the detection of the  $\alpha$ -particles since a grid-ionization chamber utilizing electron collection and an associated fast amplifier were not available. If an ionization chamber having slow pulses and an associated amplifier had been adopted, time delays between genuine coincidences from the two detectors, of the same order of magnitude as those under investigation, would have been introduced. A compensating delay-circuit introduced into one of the two channels of the coincidence unit would have added considerable complications. Recently, systems working with delayed coincidences have, however, been successfully used (4).

Two mica window Geiger-Müller counters were mounted horizontally to reduce the cosmic ray coincidence rate to a minimum. These are shown in Fig. 2. In order to obtain best counting geometry the spacing between the

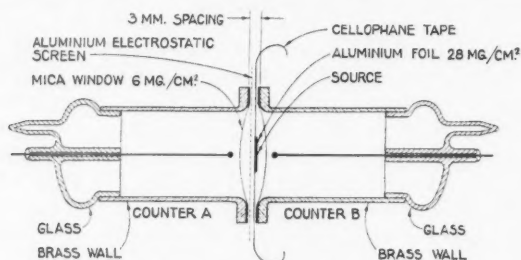


FIG. 2. Geiger-Müller counters arranged to detect  $\beta - \alpha$  coincidences. Counter A detects  $\beta$ -particles, while counter B detects  $\alpha$  and  $\beta$ -particles.

ends of the counters was reduced to a practical minimum—about 3 mm. The source was deposited over an area of about 12 mm.<sup>2</sup> on a thin aluminum foil weighing 28 mgm. per cm.<sup>2</sup> This was in turn mounted on a strip of cellophane tape, which was stretched across the window of one of the counters, the deposit being on the side of the foil opposite that to which the tape was attached. The counters and their cathode-followers were entirely surrounded by a lead housing. This expedient, although it increased the cosmic ray coincidence rate, was necessary to shield against  $\gamma$ -rays from neighboring sources in the laboratory.

The half-period of thorium C' was measured as well as that of polonium 213. The measured value of the former, standing in reasonable agreement with previous measurements, was taken as evidence that the equipment was working satisfactorily for the determination of half-periods of the order of microseconds. In both experiments the thickness of the aluminum foil was sufficient to stop the  $\alpha$ -particles of maximum range. In both cases, however,

the  $\alpha$ -particles could penetrate the mica window of one counter, which weighed 6 mgm. per cm.<sup>2</sup>. The energy of the  $\alpha$ -particles of polonium 213 is 8.336 Mev. (3, 8), which corresponds to a mean range of 7.89 cm. in air at 15° C. and 760 mm. pressure or 11.4 mgm. per cm.<sup>2</sup> in mica. The  $\alpha$ -particles of thorium C' have an energy of 8.776 Mev., a mean range of 8.56 cm. in air and 12.3 mgm. per cm.<sup>2</sup> in mica.

In the experimental arrangement counter *A* is actuated by  $\beta$ -particles and counter *B* by  $\alpha$  and  $\beta$ -particles. Both counters also respond, though at lower efficiency, to  $\gamma$ -rays.

### Electronic Equipment

A schematic arrangement of the electrical equipment is shown in Fig. 3. Steps were taken to reduce circuit delays to a minimum, to obviate the necessity of amplifiers as usually used by others in this field (1), and to produce pulses with steep and sharply defined 'front edges'. Two cathode-followers

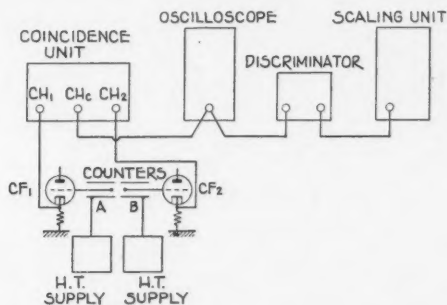


FIG. 3. Schematic diagram of experimental arrangement.

$CF_1$  and  $CF_2$  were mounted close to the counters. RCA 6AK5 miniature pentodes were used for this purpose. The negative pulses, about 50 v. in amplitude, were taken from these by screened cables to the inputs  $CH_1$  and  $CH_2$  of the two channels of a Rossi coincidence unit. The circuit was arranged so that the pulse-width or time-gate on the grid of one of the tubes of the coincidence unit was made variable, while the pulse-width on the other remained fixed. In both experiments—with thorium C' and polonium 213—the  $\alpha$ -particle is emitted *after* the  $\beta$ -particle. Thus, the time-gate  $\tau_1$  associated with counter *A*, the one responding only to  $\beta$ -particles, is chosen to have the variable width. This is shown in Fig. 4, for the case in which an  $\alpha$ -particle pulse has arrived in channel  $CH_2$  within the time interval  $\tau_1$  after the arrival of a  $\beta$ -particle in channel  $CH_1$  and for which a coincidence is recorded. The time-gate was varied by altering the time constant in the grid circuit of one tube of the Rossi circuit (switch *S* in Fig. 5).

The output pulses appearing at  $CH_c$  in Fig. 3 were taken through a discriminator to a scaling unit. An oscilloscope was also included for monitoring

purposes. The individual counting rates at  $CH_1$  or  $CH_2$  could be similarly determined.

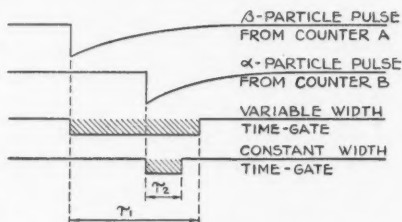


FIG. 4. Illustrating a coincidence between a  $\beta$ -particle detected in counter A and an  $\alpha$ -particle in counter B.

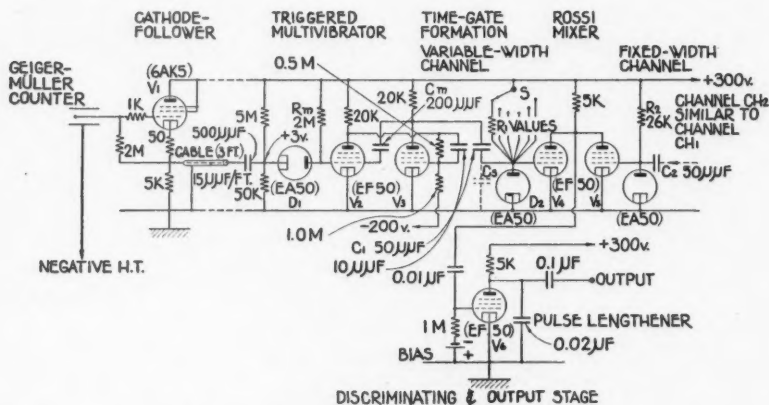


FIG. 5. Detailed diagram of electronic circuit.

The coincidence unit is shown in detail in Fig. 5 and the wave-forms in Fig. 6. Tube  $V_1$  is the cathode-follower. Tubes  $V_2$  and  $V_3$  form a Kipp relay, which produces a negative square-wave of fixed amplitude and duration on the anode of  $V_3$  when triggered by a negative pulse on the grid of  $V_2$ . The duration is set by the components  $R_m$  and  $C_m$  to be longer than the maximum value of the delay-time determined by  $R_1$  and  $C_1$ , but not so long as to produce appreciable counting losses due to pulses overlapping. Diode  $D_1$  serves two purposes, (1) as a fixed-bias discriminator and (2) as a 'buffer' stage to prevent interaction of  $V_1$  and  $V_2 - V_3$  when the multivibrator has been 'fired'. The wave-form on the anode of  $V_3$  is utilized to form the time-gate  $\tau_1$  on the grid of one of the Rossi tubes,  $V_4$ . Tube  $V_6$  performs the function of a discriminating and pulse-lengthening stage.

The circuit is symmetrical in both channels except that in the channel of variable time-gate, shown in Fig. 5, the resistance  $R_1$  is selected by means of the switch  $S$  over a range from 26K to 10M ohms in 10 stages.



Two factors that represent developments of the earlier circuits employed in the coincidence technique (1, 11) are (1) the introduction of the cathode-followers close to the Geiger-Müller counters, and (2) a modification in the

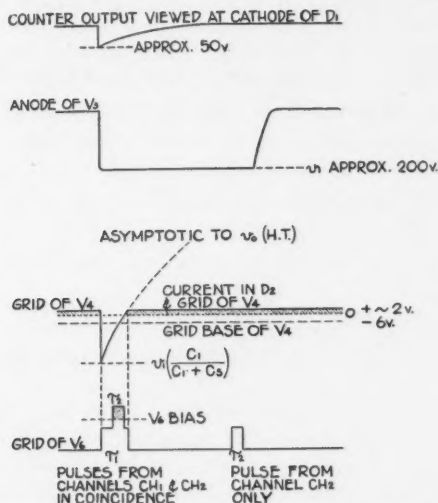


FIG. 6. Wave-forms to illustrate the operation of the coincidence circuit.

method of pulse differentiation at the grids of the Rossi tubes. The latter enables pulses of rather shorter duration (for given circuit components) and with steeper 'back edges' to be produced. The normal grid-leak  $R_1$  is taken to the positive H.T. line instead of to earth, and tube  $V_4$  operates normally at zero or with slightly positive voltage on the grid. Diode  $D_2$  is introduced to ensure that the grid potential of  $V_4$  is definite (approximately +1 v.) and to protect the grid of  $V_4$  against excessive grid current.

If  $v_0$  denotes the voltage of the positive H.T. line and  $v_1$  the amplitude of the wave-form present on the anode of  $V_3$ , the amplitude of the wave-form on the grid of the Rossi tube  $V_4$  is given by

$$v_1 \left( \frac{C_1}{C_1 + C_s} \right), \quad (1)$$

where  $C_1$  is the capacity of the coupling condenser and  $C_s$  is the sum of the stray capacities of the grid-circuit of  $V_4$  and the diode  $D_2$ . It will then be seen that the width of the time-gate  $\tau_1$  as the wave-form crosses the grid-base of  $V_4$  is related to the time-constant of the circuit  $R_1 C_1$  by the equation:

$$v_0 = \left[ v_0 + v_1 \left( \frac{C_1}{C_1 + C_s} \right) \right] e^{-\tau_1 / R_1 (C_1 + C_s)}. \quad (2)$$



A similar equation holds for the time-gate  $\tau_2$  of the other channel. With the values of the voltages and components met with in practice,  $\tau_1$  is considerably less than  $R_1C_1$ .

### Determination of Resolving Times

The following symbols are defined:

$N_1$  = Counting rate for the channel counting  $\beta$ -particles;

$N_2$  = Counting rate for the channel counting  $(\alpha + \beta)$ -particles;

$\tau_1$  = Duration of the time-gate on the variable-width or  $\beta$ -counting channel of the coincidence unit;

$\tau_2$  = Duration of the fixed time-gate on the  $(\alpha + \beta)$ -counting channel,

$\tau = \tau_1 + \tau_2$ ;

$S_1, S_2, \dots, S_{10}$  = Switch positions selecting  $R_1$  (Fig. 5) and thus altering  $\tau_1$ ;

$N_A$  = Counting rate of accidental coincidences.

(Counting rates are expressed as counts per minute, time intervals in micro-seconds.)

The determination of the resolving times for the various switch positions  $S_1, S_2, \dots, S_{10}$  was carried out by measuring the accidental coincidence rate  $N_A$  when the two counters were actuated by two independent sources of  $\beta$ -radiation. During this experiment the two counters were separated by approximately 6 ft. and enclosed in separate lead housings.

The equation

$$N_A = \frac{N_1 N_2 \tau}{60} \times 10^{-6} \quad (3)$$

was used to determine  $\tau$  from the measured values  $N_1$ ,  $N_2$  and  $N_A$ . The cosmic ray coincidence rate with this arrangement was negligible.

Table I gives the results of these measurements, and the calculated values of  $\tau$ , including standard errors, for the various switch positions.

TABLE I  
DETERMINATION OF RESOLVING TIMES

Switch S position	$R_1$ , ohms	$N_1$	$N_2$	$N_A$	$\tau$ , $\mu$ sec.
1	26K	4915	4922	$0.41 \pm 0.03$	$1.02 \pm 0.08$
2	42K	4925	5085	$0.70 \pm 0.04$	$1.68 \pm 0.10$
3	54K	5345	4895	$0.77 \pm 0.03$	$1.77 \pm 0.07$
4	67K	5475	4960	$1.00 \pm 0.06$	$2.21 \pm 0.13$
5	70K	5540	4975	$1.39 \pm 0.08$	$3.03 \pm 0.18$
6	103K	5585	5115	$1.90 \pm 0.13$	$3.99 \pm 0.27$
7	262K	5360	4670	$4.83 \pm 0.32$	$11.6 \pm 0.8$
8	520K	5425	4335	$8.32 \pm 0.48$	$21.2 \pm 1.2$
9	2M	5445	4125	$28.0 \pm 0.7$	$74.8 \pm 1.9$
10	10M	5430	3900	$85.0 \pm 2.0$	$241 \pm 6$

### Test of Coincidence Unit with Exact Coincidences

In order to test whether there were any measurable differential delays between the two channels, either in the counters or circuits, coincidence measurements were made with the normal experimental arrangement (Fig. 2) and a source that emits a large percentage of 'exactly' coincident particles. Protactinium 233 was chosen for the purpose. The  $\beta$ -emission is followed by  $\gamma$ -rays that are highly internally converted (6). The delay between the primary  $\beta$ -particle and the conversion electron is probably of the order of  $10^{-13}$  sec.

Let  $N'_C$  = measured coincidence rate.

If the coincidence apparatus is behaving properly, the quantity  $N'_C - N_A$  should be independent of the resolving time of the apparatus.

The results of this experiment are given in Table II. The values of  $N'_C - N_A$  in Column 6 are reasonably constant. This proves that differential delays between the two channels are negligible over the range of values of  $\tau$  permitted by the circuit constants.

TABLE II

TEST OF COINCIDENCE UNIT WITH EXACT  $\beta - \beta$  COINCIDENCES

(The cosmic ray coincidence rate was about one count per minute.)

Switch S position	$N_1$ ( $\pm 48$ )	$N_2$ ( $\pm 63$ )	$N'_C$	$N_A$ (calc.)	$N'_C - N_A$
1	2340	3930	$183 \pm 3.5$	0.2	$183 \pm 3.5$
2	2270	3840	$189 \pm 3.6$	0.3	$189 \pm 3.6$
3	2240	3910	$186 \pm 3.5$	0.3	$186 \pm 3.5$
4	2240	4030	$193 \pm 3.6$	0.3	$193 \pm 3.6$
5	2270	3970	$187 \pm 3.5$	0.5	$187 \pm 3.5$
6	2240	3970	$185 \pm 2.0$	0.6	$184 \pm 2.0$
7	2270	3910	$193 \pm 3.5$	1.7	$191 \pm 3.5$
8	2305	3930	$187 \pm 3.5$	3.2	$184 \pm 3.5$
9	2305	3930	$197 \pm 4.0$	11.3	$186 \pm 4.0$
10	2145	3930	$224 \pm 4.0$	34	$190 \pm 4.0$
				Average	187

### Method of Analyzing Coincidence Measurements to Determine Short Half-Periods

The measured coincidence rate is made up of the following contributions:

- (1) 'Exact' coincidences arising from cosmic rays;
- (2) 'Exact' coincidences arising from other background effects, for instance a  $\beta$ -particle passing through both counters in succession;

(3) 'Exact' coincidences caused by radiations from the radioactive source, such as  $\beta - \gamma$  coincidences if the  $\beta$ -decay has associated  $\gamma$ -rays, or  $\gamma - \gamma$  coincidences if  $\gamma$ -rays are emitted in cascade by the source;

(4) 'Accidental' coincidences, which arise from two unrelated events causing counts in the two counters of such a time correlation that they record as a coincidence;

(5) 'Delayed' coincidences of the  $\beta - \alpha$  type, arising from the short half-period under investigation.

It should be noted that 'exact' coincidences of Types 1 and 2 form a constant background. On the other hand, 'exact' coincidences of Type 3 will vary with the source strength. In the case of a source containing two or more radioactive bodies, the counting rate of Type 3 coincidences will vary with time in a manner determined by the amount of each radioactive body present and the contribution to the coincidence rate arising from the disintegration of each body.

The 'accidental' coincidence rate, Type 4 coincidences, has been determined in the usual way from the product of the counting rates in the two counters and the resolving time. Since, in some instances, as many as 10% of the counts in one counter are time correlated with the counts in the other counter, the above procedure used to calculate the 'accidental' coincidence rate is only approximate (Equation (3)). However, the 'accidental' coincidence rate is in most cases negligible, and an accurate calculation would have little influence on the analysis of the results.

The following additional symbols are defined:

$N'_C$  = Measured coincidence rate;

$N_A$  = Counting rate of accidental coincidences (Type 4);

$N_B$  = Counting rate of 'exact' coincidences that form a background independent of the source (Types 1 and 2);

$N_C$  =  $N'_C - N_A - N_B$ ;

$N_D$  = Delayed coincidence rate of the  $\beta - \alpha$  type, arising from the short half-period under investigation;

$N_{D0}$  = Asymptotic value of  $N_D$  when  $\tau_1$  is very large compared with the half-period for  $\alpha$ -decay;

$N_E$  = 'exact' coincidence rate arising from activities in the source (Type 3);

$N_{CO} = N_E + N_{D0}$ .

(Counting rates are expressed in counts per minute. A bar over the symbol, e.g.,  $\bar{N}_D$ , is used to denote a counting rate which has been corrected for source decay to a constant source strength.)

From the previous discussion it is seen that

$$N_C = N_D + N_E \quad (4)$$

$$\text{and } N_D = N_{D0}(1 - e^{-\lambda\tau_1}), \quad (5)$$

where  $\lambda$  is the transformation constant of the  $\alpha$ -active body, and

$$N_A = \frac{N_1 N_2 \tau}{60} \times 10^{-6}. \quad (3)$$

In analyzing the data for the half-period of the short-lived radioactive body, the following procedure was used.

- (a) Calculate  $N_A$  from the relevant values of  $N_1$ ,  $N_2$  and  $\tau$ ;
- (b) Evaluate  $N_C = N'_C - N_A - N_B$ . (The value of  $N_B$  throughout these experiments was taken to be about 1.0 count per minute, which is, strictly speaking, only the cosmic ray portion.);
- (c) Correct the values of  $N_C$  for readings taken during the decay of the source to a constant source strength, obtaining  $\bar{N}_C$  for the various values of  $\tau$ ;
- (d) From an inspection of the values of  $\bar{N}_C$  for values of  $\tau$  very large compared with the half-period for  $\alpha$ -decay verify that  $\bar{N}_C$  is constant within the experimental error of these readings and then choose the average value as  $\bar{N}_{CO}$ ;

(e) Since

$$\begin{aligned} \bar{N}_C &= \bar{N}_B + \bar{N}_{DO}(1 - e^{-\lambda\tau_1}) \\ &= \bar{N}_{CO} - \bar{N}_{DO} e^{-\lambda\tau_1}, \end{aligned} \quad (6)$$

it follows that

$$\bar{N}_{CO} - \bar{N}_C = \bar{N}_{DO} e^{\lambda\tau_1} e^{-\lambda\tau} = \text{constant } e^{-\lambda\tau}. \quad (7)$$

Consequently, the desired transformation constant,  $\lambda$ , can be found from the slope of the line in the semilogarithmic plot of

$$\bar{N}_{CO} - \bar{N}_C \text{ against } \tau.$$

### Measurement of the Half-Period of Thorium C'

As a preliminary experiment to the measurement of the half-period of polonium 213, it was thought desirable to test the apparatus on thorium C', whose period had previously been measured by other experimenters (2, 5). Thorium active deposit on an aluminum foil was used as the source. Thorium B is collected in the emanation, and it transforms successively to thorium C, thorium C', and thorium D. The results of the experiment are shown in Table III and Fig. 7.

The elapsed times  $t$  to the mid-points of the measured coincidence runs are given with reference to the first. These are used to correct  $N_C$  for decay of the source, yielding  $\bar{N}_C$ . The amounts of thorium B and thorium C present depend on the duration of collection of the active deposit and the elapsed time from the end of collection to the mid-point of the coincidence measurement. Unfortunately these times were not recorded. The best that can be done now is to fit the measured rates  $N_C = N'_C - N_A - N_B$  at the various times  $t$  tabulated for switch positions 10 to 5 inclusive. The associated times  $\tau$  are so long that the rates  $N_D$  due to  $\beta - \alpha$  coincidences only have their asymptotic

TABLE III  
MEASUREMENTS TO DETERMINE HALF-PERIOD OF THORIUM C'

Switch S position	$t$ , hr.	$N_1$ ( $\pm 47$ )*	$N_2$ ( $\pm 75$ )*	$N'_C$	$N_A$ (calc.)	$N_C$ ( $N_B=1$ )	$\bar{N}_C$	$\bar{N}_{Co} - \bar{N}_C$ ( $\bar{N}_{Co}=353 \pm 2$ )
10	0	2240	5600	$401 \pm 7$	50	350	350	$(+3 \pm 8)$
9	0.15	2335	5600	$364 \pm 7$	16	347	347	$(+6 \pm 8)$
8	0.45	2270	5500	$359 \pm 4$	4	354	355	$(-2 \pm 8)$
7	0.70	2340	5440	$357 \pm 7$	2	354	357	$(-4 \pm 8)$
6	1.13	2270	5440	$353 \pm 5$	1	351	359	$(-6 \pm 6)$
5	1.61	2310	5310	$339 \pm 4$	1	337	351	$(+2 \pm 5)$
4	2.06	2270	5150	$330 \pm 5$	1	328	349	$(+4 \pm 6)$
3	2.45	2175	4980	$307 \pm 4$	0	306	332	$21 \pm 5$
2	3.03	2175	4980	$281 \pm 3$	0	280	313	$40 \pm 4$
1	3.56	2045	4860	$203 \pm 4$	0	202	233	$120 \pm 5$

\* Standard errors for  $N_1$  and  $N_2$ ; each reading represents a count for one minute only.

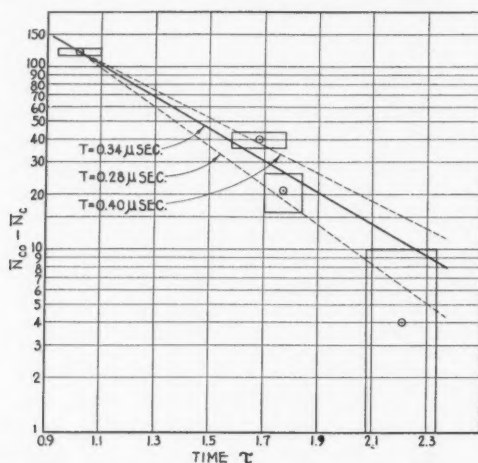


FIG. 7. Measurements to determine the half-period of thorium C'. The coincidence rates in counts per minute are plotted semilogarithmically against the resolving times  $\tau$  in microseconds.

values  $N_{Do}$  (independent of the half-period of thorium C' and of  $\tau$ ), and  $N_C$  has the asymptotic value  $N_{Co} (= N_{Do} + N_E)$ .

The value of  $N_{Do}$  depends only on the number of atoms of thorium C that disintegrate per minute. The 'exact' coincidence rate  $N_E$  depends jointly on the numbers of atoms of thorium B and thorium C that disintegrate per minute. From the Rutherford-Soddy theory of successive transformations one expects that  $N_{Co} (= N_{Do} + N_E)$  would vary with the time  $t$  from the end of the collection time in the emanation according to

$$Ae^{-\lambda_1 t} - Be^{-\lambda_2 t},$$

where  $\lambda_1$  and  $\lambda_2$  are the well known transformation constants of thorium B and thorium C respectively and  $A$  and  $B$  are constants. It is found that the measured coincidence rates  $N_{CO}$  for switch positions 10 to 5 inclusive are well represented by

$$N_{CO} = 390.5 e^{-\lambda_1 t} - 37.2 e^{-\lambda_2 t}, \quad (8)$$

where  $t$  takes the values in Column 2 of Table III. It is then necessary to assume that the subsequent decay, for switch positions 4 to 1 inclusive, follows

$$N_C = 390.5 e^{-\lambda_1 t} - 37.2 e^{-\lambda_2 t}. \quad (9)$$

The values of  $N_C$  were accordingly corrected for decay to zero time (Column 8).

The value chosen for  $\bar{N}_{CO}$  is  $353 \pm 2$  counts per minute. As shown in the previous section (Equation (7)), the logarithms of  $\bar{N}_{CO} - \bar{N}_C$  are plotted against  $\tau$  (Table I), and the required half-period of thorium C' is derived from the slope of the straight line (Fig. 7). The final result for the half-period is

$$T = 0.34 \pm 0.06 \mu\text{sec.}$$

The spacing of the values of  $\tau$  at the consecutive switch positions is rather wide for the measurement of such a short half-period. However, the derived value is in reasonable agreement with other measurements:  $0.3 \pm 0.1 \mu\text{sec.}$  (Dunworth (5)),  $0.26 \pm 0.04 \mu\text{sec.}$  (Bradt and Scherrer (2)), and  $0.30 \pm 0.015 \mu\text{sec.}$  (Hill (10)).

### Measurement of the Half-Period of Polonium 213

A sample of radium 225 was prepared as a source of polonium 213. From the portion of the  $(4n + 1)$ -series shown in Fig. 1 it is seen that the amount of polonium 213 follows the decay of the actinium 225 rather closely. The radium 225 was used in this experiment 21 days after its preparation. The reduction in the disintegration rate of actinium 225 over one day, the duration of each run, is estimated at 1.2% from the Rutherford-Soddy theory of successive transformations. It is therefore unnecessary to correct for the decay of the source. Two independent runs were made on two successive days. The measurements are shown in Table IV and Fig. 8. The final value of the half-period is

$$T = 4.2 \pm 0.8 \mu\text{sec.}$$

Unfortunately, the values of  $\tau$  chosen for the circuit are not spaced in the optimum manner for accuracy of the half-period. However, a stronger source would have been necessary to make better use of larger and better spaced values of  $\tau$ , and this was not available.

The result of this experiment was included in the brief communication published last year (8). The half-period of polonium 213 given in the present paper supersedes that listed ( $4.4 \mu\text{sec.}$ ) in reference (8).

When the Geiger-Nuttall plot is made for the  $(4n + 1)$ -series, it is seen that polonium 213 shows a deviation in the same sense as the C'-bodies in the other radioactive series.

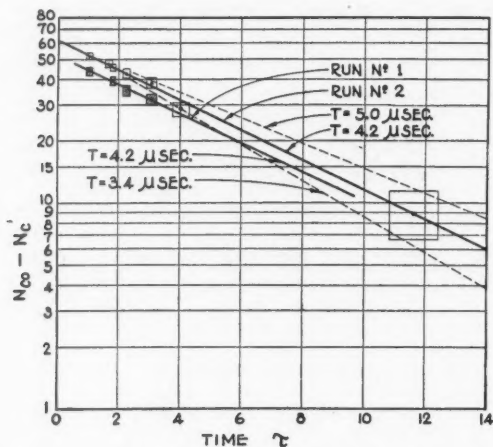
TABLE IV

MEASUREMENTS TO DETERMINE HALF-PERIOD OF POLONIUM 213

Switch S position	$N_1$ ( $\pm 30$ )*	$N_2$ ( $\pm 53$ )*	$N'_G$	$N_A$ (calc.)	$N_C$ ( $N_B = 1.1$ )	$N_{CO} - N_C$
First run						$N_{CO} = 75.5 \pm 1.5$
10	842	2702	$84.8 \pm 1.9$	9.1	74.6	$(+0.9 \pm 2.4)$
9	917	2834	$80.6 \pm 2.1$	3.2	76.3	$(-0.8 \pm 2.6)$
8	917	2887	$77.5 \pm 2.1$	0.9	75.5	$(0.0 \pm 2.6)$
5	908	2784	$44.7 \pm 1.5$	0.1	43.5	$32.0 \pm 2.1$
4	906	2923	$41.2 \pm 1.5$	0.1	40.0	$35.5 \pm 2.1$
3	926	2857	$37.2 \pm 1.4$	0.1	36.0	$39.5 \pm 2.1$
2	901	2826	$(48.6 \pm 1.7)^\dagger$	0.1	(47.4)	$(28.1)^\dagger$
1	886	2844	$32.4 \pm 1.2$	0	31.3	$44.2 \pm 1.9$
Second run						$N_{CO} = 79.7 \pm 1.5$
10	924	2944	$92.5 \pm 1.9$	11.0	80.4	$(-0.7 \pm 2.4)$
9	942	2784	$83.4 \pm 1.5$	3.3	79.0	$(+0.7 \pm 1.9)$
8	924	2999	$79.2 \pm 2.0$	0.9	77.2	$(+2.5 \pm 2.5)$
7	861	2960	$72.2 \pm 1.9$	0.5	70.6	$9.1 \pm 2.4$
6	893	2897	$52.3 \pm 1.6$	0.2	51.0	$28.7 \pm 2.2$
5	937	2890	$42.6 \pm 1.5$	0.1	41.4	$38.3 \pm 2.1$
4	829	2925	$38.3 \pm 1.1$	0.1	37.1	$42.6 \pm 1.9$
3	811	2967	$35.2 \pm 1.3$	0.1	34.0	$45.7 \pm 2.0$
2	887	2817	$33.2 \pm 1.3$	0.1	32.0	$47.7 \pm 2.0$
1	832	2816	$28.6 \pm 1.2$	0	27.5	$52.2 \pm 1.9$

\* Standard errors for  $N_1$  and  $N_2$ ; each reading represents a count for one minute only.

† Rejected; perhaps vitiated by electrical interference.

FIG. 8. Measurements to determine the half-period of polonium 213. The coincidence rates in counts per minute are plotted semilogarithmically against the resolving time  $\tau$  in microseconds.



### Acknowledgments

The author wishes to thank Dr. A. N. May and Mr. A. G. Ward for their interest and valuable advice during the experiment, and Mr. A. C. English and Dr. L. G. Elliott for preparing the radioactive sources. Dr. B. W. Sargent and Mr. A. G. Ward have generously assisted in preparing this paper for publication.

### References

1. BRADT, H. and SCHERRER, P. *Helv. Phys. Acta*, 16 : 251. 1943.
2. BRADT, H. and SCHERRER, P. *Helv. Phys. Acta*, 16 : 259. 1943.
3. CRANSHAW, T. E. and HARVEY, J. A. *Can. J. Research, A*, 26 : 243. 1948.
4. DE BENEDETTI, S. and MCGOWAN, F. K. *Phys. Rev.* 70 : 569. 1946.
5. DUNWORTH, J. V. *Nature*, 144 : 152. 1939.
6. ELLIOTT, L. G. Private communication. 1945.
7. ENGLISH, A. C. Unpublished report, MC-145. The  $(4n + 1)$  radioactive series. National Research Council of Canada, 1945.
8. ENGLISH, A. C., CRANSHAW, T. E., DEMERS, P., HARVEY, J. A., HINCKS, E. P., JELLEY, J. V., and MAY, A. N. *Phys. Rev.* 72 : 253. 1947.
9. HAGEMANN, F., KATZIN, L. I., STUDIER, M. H., GHIORSO, A., and SEABORG, G. T. *Phys. Rev.* 72 : 252. 1947.
10. HILL, J. M. Private communication. 1948.
11. ROTBLAT, J. *Proc. Roy. Soc. London, A*, 177 : 260. 1941.



## HEAT TRANSFER WITH SURFACE BOILING<sup>1</sup>

By J. W. KNOWLES

### Abstract

These experiments were undertaken to investigate the transfer of heat from solid surfaces to flowing water. The bulk temperature of the cooling water was below the boiling point, and the surface temperature of the heat transfer tube went to about 100° C. above the boiling point. Water velocities ranged up to 10 ft. sec.<sup>-1</sup> and heat fluxes up to 720 w. cm.<sup>-2</sup>. The non-dimensional heat transfer constant  $a$  in the Dittus and Boelter formula  $(Nu) = a(Re)^{0.8}(Pr)^{0.4}$ , which under normal forced convection has a value of  $2.30 \times 10^{-2}$ , increased to four times the normal value under the surface boiling conditions. It is shown graphically that the constant  $a$  bears a simple relation to the heat flux and the length-diameter ratio for surface temperatures below a certain value. For constant heat flux and volume flow rate, the surface temperature rises with rising bulk liquid temperature until it reaches the certain value of the surface temperature referred to above. The surface temperature then remains constant with further rise in the bulk liquid temperature until conditions become too unstable for measurements.

### Introduction

The main object of this investigation was to study the transfer of heat from a solid surface to flowing water when the temperature of the solid surface was above the boiling point. Information on surface boiling is of general interest owing to its possible bearing on the design of steam engines, and it is of particular importance in the design of atomic reactors where irregularity in the boiling rate might lead to operating difficulties. The data on heat transfer by surface boiling to a moving fluid is meager. In previous experiments (1), the metal surface has been heated by high pressure steam. This leads to difficulties in determining the surface temperature from the properties of the steam, because the variations in the heat transfer, caused by the condensation of the steam on the inside surface, are uncertain. Also, it is difficult to determine the surface temperature by the use of a thermocouple embedded below the metal surface if the metal wall is only slightly thicker than the thermocouple, because the presence of the thermocouple disturbs the heat flow through the wall.

In the following experiment, an electrically heated stainless steel heat transfer tube was used in order to avoid some of these difficulties and to obtain high heat fluxes from moderate power supplies. The outside surface temperature of this tube was calculated from the electrical energy dissipated in the tube and the temperature registered by a thermocouple inside the tube.

### Experimental

A flow diagram of the heat exchange unit is given in Fig. 1. The heat transfer column, Fig. 2, was the only part of the heat exchange unit that was

<sup>1</sup> Manuscript received in original form September 4, 1947, and, as revised, February 25, 1948. Contribution from the Chalk River Laboratory, Division of Atomic Energy Research of the National Research Council of Canada. Issued as N.R.C. No. 1778.

altered during the experiment. Different diameters and lengths of glass and stainless steel tubes were used, as summarized in Table I.

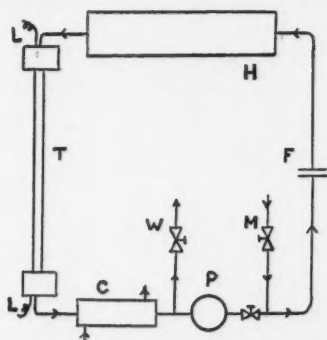


FIG. 1. Flow diagram for heat exchange unit,

- |                                      |                                     |
|--------------------------------------|-------------------------------------|
| <i>L</i> , power leads.              | <i>P</i> , pump.                    |
| <i>T</i> , heat transfer tube.       | <i>M</i> , main inlet (hot).        |
| <i>C</i> , water cooler.             | <i>F</i> , calibrated flowmeter.    |
| <i>W</i> , water pressure regulator. | <i>H</i> , heater coil, 60 kw. max. |

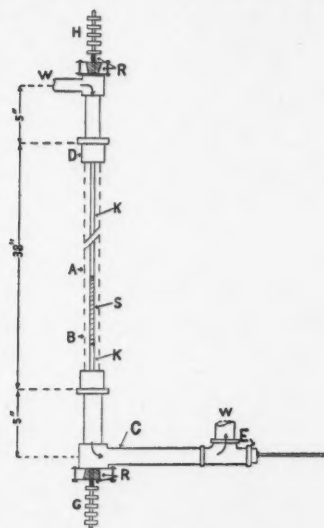


FIG. 2. Heat transfer column,

- |   |  |
|---|--|
| <i>H</i> and <i>G</i> , electric conductors.  | <i>A</i> , glass tube.                     |
| <i>W</i> , water inlet and outlet.  | <i>S</i> , stainless steel heated section. |
| <i>K</i> , 0.25 in. copper conductors.  | <i>E</i> , thermometer and thermocouple.   |
| <i>R</i> , spring to prevent heater rod from buckling when the rod expands through rubber ring. |  |
| <i>B</i> , <i>C</i> , and <i>D</i> , indicate positions discussed in the text.                  |  |

Copper-constantan thermocouples were used for the following temperature measurements. The internal temperature  $T_1$  of the stainless steel tube was measured at 2 cm. above the lower solid copper conductor, Fig. 3. The outside

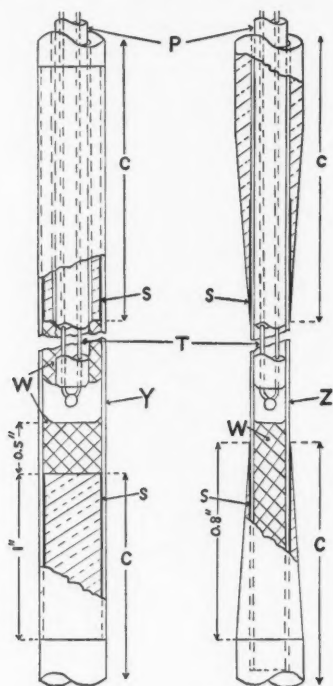


FIG. 3. Heater elements.

*C*, copper tube and copper rod conductors,  
*T*, thermocouples.  
*Y*, stainless steel tube (0.25 in. O.D.).  
*Z*, stainless steel tube (0.12 in. O.D.).

*W*, glass wool.  
*P*, porcelain insulators.  
*S*, solder joints.

surface temperature of the stainless steel tube at this position, also indicated by *B*, Fig. 2, was calculated from the known heat flux and tube temperature  $T_1$ . Drawing a thermocouple up the inside of the heat transfer tube, when it was heated, showed the temperature gradient to be approximately  $0.2^\circ \text{C. in.}^{-1}$ . Thus, any error in the internal temperature  $T_1$  caused by conduction along the thermocouple leads was negligible. To measure the inlet bulk temperature  $T_2$  of the cooling water before it reached the heated section *S*, a thermocouple was soldered to a thin copper strip, which was in turn clamped to the outside of the glass tube at *A*, Fig. 2. To measure the bulk outlet temperature at point *E*, Fig. 2, a thermocouple and a precision thermometer, accurate to  $0.2^\circ \text{C.}$ , were immersed directly in the flowing water. The thermometer

required five minutes longer than the thermocouples to reach equilibrium conditions, and thus was used only for standardization.

The thermocouples were standardized between 30° and 130° C. against the thermometer at *E*, Fig. 2. The temperature of the water circulating in the closed system was varied between 30° and 130° C. by means of the heater, *H*, Fig. 1. During standardization no power was supplied to the heat exchange unit. Temperature readings up to 230° C. were obtained by a linear extrapolation of the thermocouple standardization.

The whole heat transfer column from *D* to *E*, Fig. 2, was insulated with 1 cm. of glass wool and from 2 to 3 cm. of cotton wool packing. Any error due to insulation imperfections was assumed insignificant, as it was present in both the standardization and the actual experiment.

A pressure gauge accurate to 2% registered the pressure at position *C*, Fig. 2. The pressure at *C* was equal, within 1%, to the pressure at *B*, the lowest point on the heated tube where boiling occurred. It was for this point on the heated tube that all heat transfer coefficients were calculated. The pressure at point *C* was held at 26.0 lb. in.<sup>-2</sup> gauge, or 40.6 lb. in.<sup>-2</sup> absolute throughout all the experiments.

When an experimental run was made, the heat flux and the rate of water flow to the heat transfer tube were kept constant. The input bulk water temperature  $T_2$  was increased by decreasing the water flow through the water cooler, *C*, Fig. 1. Equilibrium temperature conditions were considered to have been reached when the inlet bulk temperature  $T_2$  varied by no more than 0.2° C. during the two minute interval required to take all the readings and to repeat the first temperature reading  $T_2$ . At a sufficiently high input water temperature, the cooling water failed to transfer the heat from the hot surface because of heat insulation caused by steam formation. This input temperature is called 'the breakdown point'. Near breakdown, the temperature measurements were accepted if the input temperature was rising no faster than 1° C. in two minutes.

### Accuracy of Measurements

All temperatures were measured to an accuracy of  $\pm 0.5^\circ$  C. Heat flux and flow rates were measured to better than  $\pm 1\%$ . Thus, for the large temperature difference experienced, the heat transfer coefficient  $h$  was accurate to about  $\pm 2\%$ , and was reproducible within this limit. A calculation of the temperature of the cooling water at *E*, Fig. 2, was made for all experiments from a knowledge of the heat input and the flow rate. This calculated temperature agreed with the measured temperature at *E*, Fig. 2, to within 1%.

All the stainless steel heat transfer tubes were highly polished before use and were repolished after one hour of continuous use. The Montreal tap water that was used produced no visible dirt film deposit on these tubes after four hours of continuous moderate boiling in the tube. Under heavy boiling in the tube, the polish disappeared beneath a dirt film in about 15 min., and a

distinct red coating was produced after 30 min. Continuous running of the boiling heat transfer for 24 hr., at a heat flux of  $200 \text{ w. cm.}^{-2}$  and a flow rate of  $99 \text{ gm. sec.}^{-1} \text{ cm.}^{-2}$ , produced a dirt film 0.05 mm. thick, but did not produce any lowering of the heat transferred. At very high boiling rates and at heat fluxes greater than  $200 \text{ w. cm.}^{-2}$ , any dirt film that had formed was pulled almost completely off by the scouring action of the bubbles.

### Description of Surface Boiling

The boiling on the heat transfer tube was very similar to that observed by C. H. Brooks and W. L. Badger (1). When the surface temperature of the stainless steel tube was a few degrees above the boiling point, long chains of bubbles formed at distinct nuclei on the heated surface. The main body of the bubble streams stayed close to the stainless steel tube, and a fine spray of bubbles extended out further into the cooling water. As the surface temperature was increased, the chains of bubbles projected further into the water flow, the fine spray extended to the outside walls, and the central heater tube became obscured by the moving steam bubbles. When the heat flux or the input temperature  $T_2$  was increased sufficiently, the surface boiling became very unstable, and regularly spaced clouds of bubbles travelled down the heat transfer tube. On passing this unstable condition, called the 'breakdown' point, the bubble size would increase suddenly, and if the electric power were not shut off immediately the stainless steel tube would fuse. When using the smaller tube,  $D = 0.47 \text{ cm.}$ , Table I, a volume of steam would be produced that would force the water up and down the transfer tube away from the center of the disturbance, and would stop the water pump. The central stainless steel tube would be violently shaken, and the outer glass tube shattered if the stainless steel tube came into contact with it. With the larger tube,  $D = 1.00 \text{ cm.}$  the cooling water always remained flowing, and no outer glass tubes were broken.

### Correlation of Heat Transfer Data

In order to correlate the results, it was found necessary to distinguish two boiling regions. The basis for this distinction shows itself in the following procedure. If one keeps the heat flux in the heat transfer tube and the mass flow rate constant, and gradually raises the bulk water temperature, the surface temperature of the heat transfer tube also will increase at first. At a certain value of input bulk temperature, at which vigorous boiling is occurring in the heat transfer column, the surface temperature of the heat transfer tube will cease to rise with increasing bulk temperature, as shown in Figs. 9 and 10. This effect of constant surface temperature will extend over a range of from  $5^\circ$  to  $20^\circ \text{ C.}$  of increasing bulk temperature, depending on the heat flux and the flow rate, before the breakdown bulk temperature is reached.

The region in which the surface temperature rises normally with increasing bulk temperature is termed the normal boiling region. The constant surface temperature region is termed the critical boiling region.

TABLE I

LENGTH OF HEATER SURFACE,  $L$ ; HYDRAULIC DIAMETER, DIFFERENCE BETWEEN THE INNER AND OUTER DIAMETER OF THE WATER ANNULUS,  $D$

No.	$L$ , cm.	Area of heated surface, cm.	$D$ , cm.	Area of annulus, cm.	Mass flow rate, gm.sec. <sup>-1</sup> cm. <sup>-2</sup>	$L/D$
1*	30.55	60.3	0.47	0.63	285	64.3
2	30.55	60.3	0.47	0.63	108	64.3
3	30.55	60.3	1.00	1.79	302	30.5
4	30.55	60.3	1.00	1.79	210	16.1
5	76.2	150.8	1.00	1.79	99.0	75.9
6	30.55	60.3	1.00	1.79	99.0	30.4
7	7.62	15.1	1.00	1.79	99.0	7.6
8	7.62	15.1	0.47	0.63	77.0	16.1
9**	29.5	29.4	1.32	2.09	279	22.3
10	29.5	29.4	1.32	2.09	86.1	22.3

\* In Series 1 to 8 the heater tube was  $\frac{1}{8}$  in. or 0.63 cm. diameter.

\*\* In Series 9 and 10 the heater tube was  $\frac{1}{4}$  in. or 0.32 cm. diameter.

The correlation of all results was based on finding variations in  $a$  of the well known Dittus and Boelter relation (2),

$$Nu = a(Re)^{0.8}(Pr)^m,$$

$Re = \frac{(DG)}{\mu}$ , which is the Reynolds dimensionless criterion;

$Pr = \frac{(c\mu)}{K}$ , which is the corresponding Prandl criterion;

$Nu = \frac{(hD)}{K}$ , which is the corresponding Nusselt criterion;

$D$  = the hydraulic diameter of the space through which the water flows, and is equal to the difference between the inner and outer diameters of the water tube in centimeters;

$G$  = the mass flow rate in grams per square centimeter;

$\mu$  = the viscosity of the cooling water, c.g.s.;

$K$  = the thermal conductivity of the cooling water, c.g.s.;

$c$  = the specific heat of the cooling water, c.g.s.;

$h$  = the liquid to surface coefficient of heat transfer, calculated from

$$h = \frac{q}{t_s - t_B}$$

$q$  = the heat flux in watts per square centimeter;

$t_s$  = the surface temperature;

$t_B$  = the bulk temperature.

This equation was found to fit the heat transfer points for normal boiling by choosing  $m = 0.4$ .  $Pr$  and  $Re$  were computed with the arithmetic averages of surface and bulk temperature at  $B$ , Fig. 2, rather than with the bulk tem-

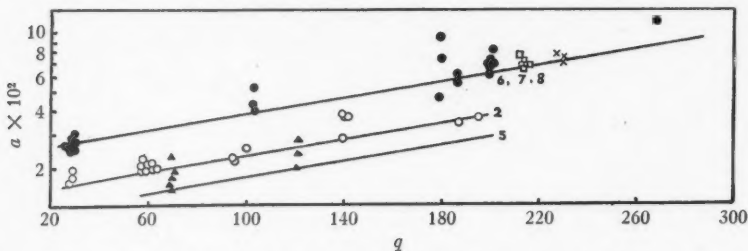


FIG. 4. Log  $a$  versus heat flux  $q$  watts per square centimeter, for low mass flow rates. The numbers refer to Table I, 2—open circles; 5—triangles; 6—solid circles; 7—squares; 8—crosses.

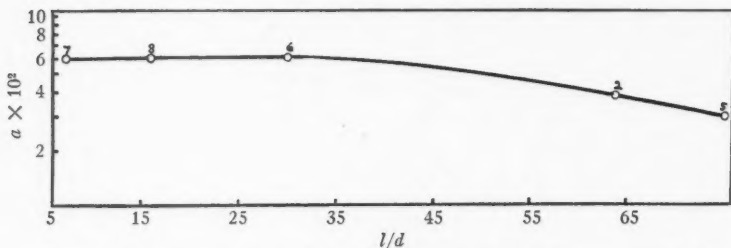


FIG. 5. Log  $a$  versus length/diameter for a heat flux of 200 w. cm.<sup>-2</sup>. Mass flow rates from 77 to 408 gm. sec<sup>-1</sup> cm.<sup>-2</sup>. The numbers refer to Table I.

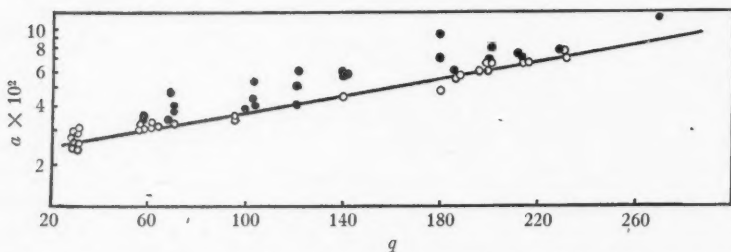


FIG. 6. Log  $a$  versus heat flux  $q$  watts per square centimeter. Before the constant surface temperature is reached, open circles; after the constant surface temperature is reached, solid circles.

perature alone, since better over-all correlation of data was obtained with the former.

Without surface boiling the average value of  $a$  is 0.023. With rapid surface boiling the measured values of  $a$  were much higher than this value. In Fig. 4 the points indicated by any one type of symbol represent the variation of  $a$



with heat flux  $q$  for the length-diameter ratio and flow rate given in Table I. These values of  $a$  include results from the normal boiling and critical boiling regions. Each straight line in Fig. 4 represents the variation of  $a$  with  $q$  for

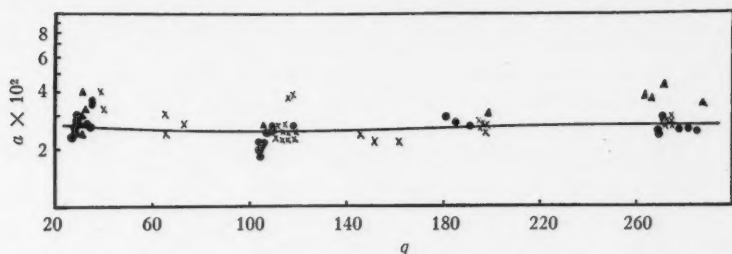


FIG. 7. Log  $a$  versus heat flux  $q$  watts per square centimeter, for high mass flow rate. Table I, No. 4, triangles; No. 3, solid circles; No. 1, crosses.

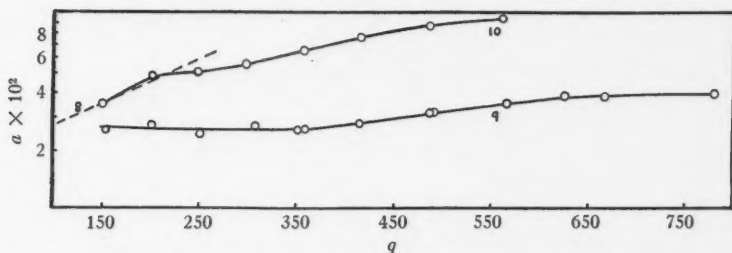


FIG. 8. Log  $a$  versus heat flux  $q$  watts per square centimeter, for high heat fluxes. The numbers refer to Table I.

values of  $a$  in the normal boiling region with a given geometry and flow rate. Values of  $a$  in the critical boiling region with a given geometry and flow rate are always greater than the values of  $a$  for normal boiling.

Reference to Table I shows that as the length-diameter ratio increases, the straight lines of Fig. 4 are shifted parallel to themselves towards lower values of  $a$ . This lowering of  $a$  with increasing length/diameter is represented in Fig. 5 for  $q = 200$  w. cm.<sup>-2</sup>. By multiplying all the values of  $a$  represented by a given symbol in Fig. 4, by a constant factor, the parallel lines in Fig. 4 may be brought into coincidence with line 7, Fig. 4. This is shown in Fig. 6. The line drawn through the open circles in Fig. 6 represents the heat correlation for normal boiling. The experimental points above the line, represented by solid circles, are the value of  $a$  in the critical boiling region.

For high mass flow rates, ( $G = 279$  gm. sec.<sup>-1</sup> cm.<sup>-2</sup>), the effect of surface boiling on heat transfer became noticeable only at heat fluxes above 260 w. cm.<sup>-2</sup>, Fig. 7. The constant surface temperature effect was observed also at these high flow rates, but there was no consistent evidence in the correlation

of points from which to conclude that the highest  $a$  values plotted in Fig. 7 were caused by this effect.

The effect of surface boiling on the heat transfer constant  $a$  at heat fluxes above  $200 \text{ w. cm.}^{-2}$ , is shown in Fig. 8. Curve 10, Fig. 8, is a plot of  $a$  for low mass flow rates, ( $G = 86 \text{ gm. sec.}^{-1} \text{ cm.}^{-2}$ ). Curve 10 was obtained with

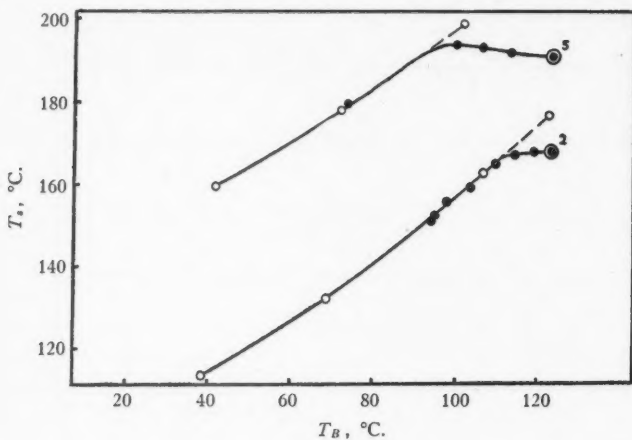


FIG. 9

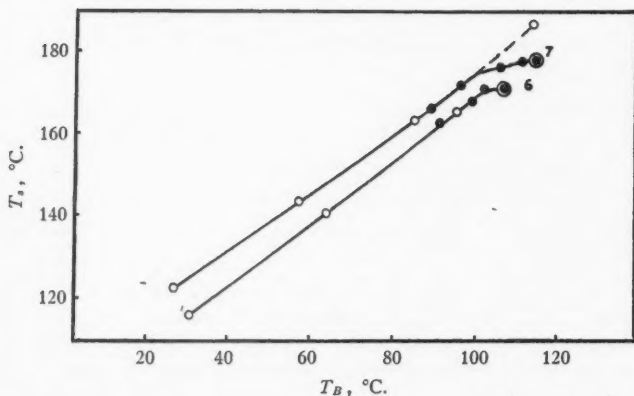


FIG. 10

FIGS. 9 AND 10. Outside surface temperature of stainless steel tube  $T_s$ , °C. versus bulk temperature of cooling water at B, Fig. 2,  $T_B$ , °C. Values calculated from the Dittus and Boelter equation using values of  $a$  from Fig. 4, open circles; experimental values near breakdown, solid circles; experimental values at breakdown, double circles. Curve 5,  $q = 69.3 \text{ w. cm.}^{-2}$ ; Curve 2,  $q = 59.1 \text{ w. cm.}^{-2}$ ; Curve 7,  $q = 214 \text{ w. cm.}^{-2}$ ; Curve 6,  $q = 201 \text{ w. cm.}^{-2}$ . The curve numbers refer to Table I.

apparatus of the same length/diameter ratio as that of Curve 8, but of different heater diameter (see Table I). Curve 8, Fig. 4, replotted as a broken line in the same figure with Curve 10 shows that the agreement is satisfactory.

At low heat fluxes and high flow rates, Curve 9, Fig. 8, and the curve of Fig. 7 agree well, although the results of Fig. 7 were obtained with a heater tube of a different diameter than that of Curve 9, Fig. 8; Table I. Curve 9 shows clearly that for mass flow rates of  $279 \text{ gm. sec.}^{-1} \text{ cm.}^{-2}$ , which correspond to Reynolds numbers of the order of  $1.5 \times 10^5$ , the effect of surface boiling became noticeable only at heat fluxes above  $300 \text{ w. cm.}^{-2}$ .

### Conclusion

All physical properties in the Dittus and Boelter equation depending on the cooling water temperature were taken at the arithmetic average of the surface and bulk water temperatures. Similar calculation, using the bulk temperature instead of the arithmetic average temperature, gave the same general agreement as that shown by the graphs, but the values of  $a$  were higher by from 10% to 20% and showed more scattering when one attempted to correlate results in the manner shown in the graphs.

However when either the bulk or the average temperature is used the experimental data presented can be correlated in a consistent manner by assuming a length-diameter effect, Fig. 5. The lowering of the heat transfer coefficient  $a$  with increasing heated length probably occurred because bubbles produced by the heat transfer did not collapse immediately in the cooling water, and so caused an accumulation of steam when the heated section of the tubes was sufficiently long.

The constant surface temperature effect shown in Figs. 9 and 10 was present in all experimental arrangements, and if further experimental data had been obtained these regions could have been mapped out completely. Qualitatively, for the same heat transfer column dimensions and rate of flow, the surface temperature tended to remain constant over a wider range of bulk temperatures at the higher values of heat fluxes.

The experiments show that, for normal boiling, heat transfer conditions can be correlated with the usual Dittus and Boelter relation if one takes account of the variations of  $a$  with the heat flux and length-diameter ratio. If one uses an irreversible source process for the production of heat, such as the stainless steel heat transfer tube used here, or atomic energy, the critical boiling region has a broad constant temperature range which may serve as a safety indicator between normal boiling and the dangerous breakdown point. Thus, under such conditions, it should be safe to operate in the normal boiling region. With suitable geometry the surface temperature of the stainless steel may be from  $80^\circ$  to  $100^\circ \text{ C.}$  above the boiling point. At high heat fluxes and low flow rates the transfer coefficient can increase by a factor of 4 and still have stable conditions.

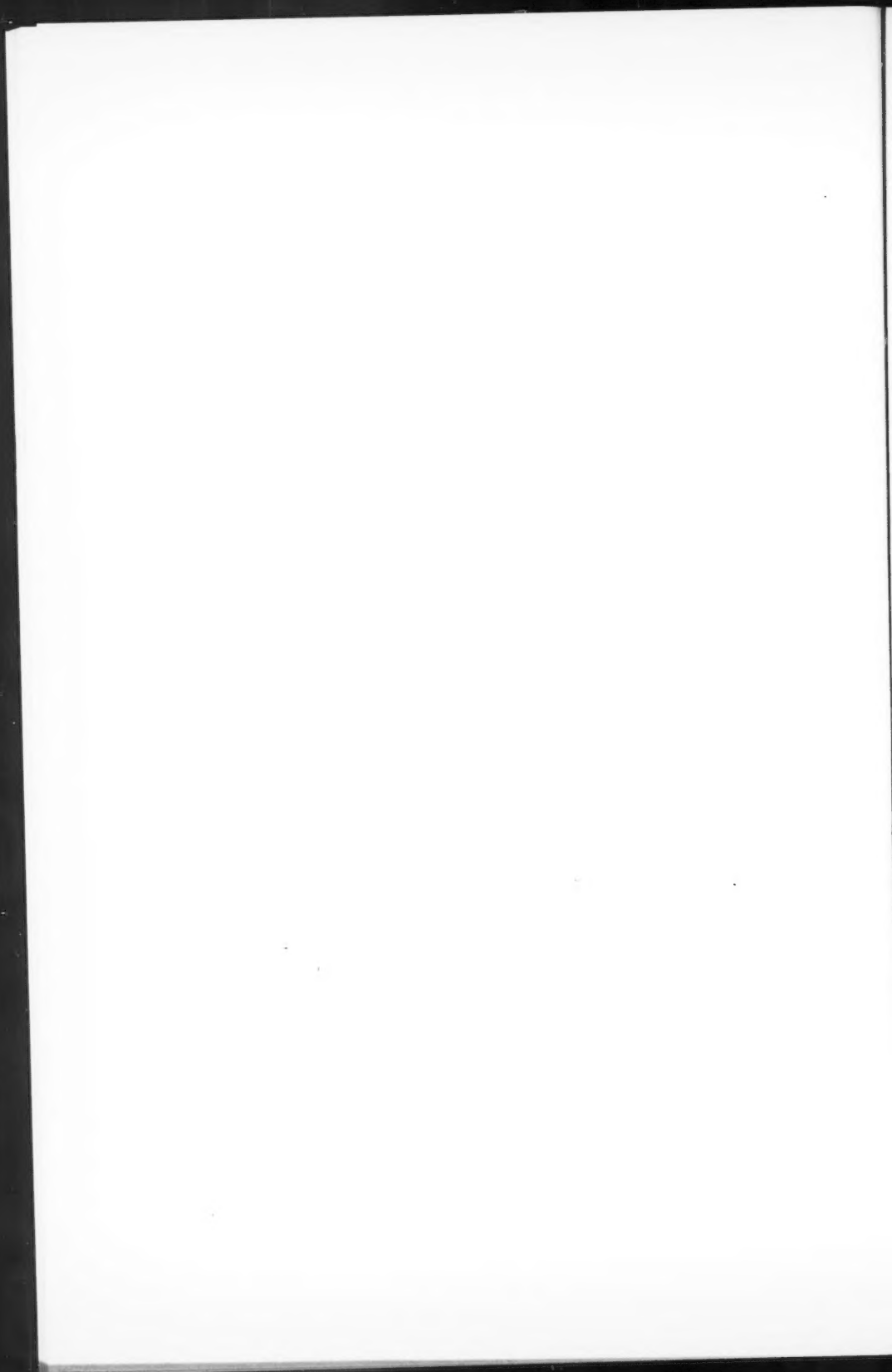
### Acknowledgments

The author wishes to express his gratitude to Dr. S. G. Bauer for his suggestion of the problem and his guidance, and to Dr. W. H. McAdams for his helpful criticism.

### References

1. BROOKS, C. H. and BADGER, W. L. Trans. Am. Inst. Chem. Engrs. 33 : (No. 3) 392. 1937.
2. BOARTS, R. M., BADGER, W. L., and MEISENBURG, S. J. Trans. Am. Inst. Chem. Engrs. 33 : 363. 1937.





## CANADIAN JOURNAL OF RESEARCH

### Notes on the Preparation of Copy

**GENERAL:**—Manuscripts should be typewritten, double spaced, and the **original and one extra copy** submitted. Style, arrangement, spelling, and abbreviations should conform to the usage of this Journal. Names of all simple compounds, rather than their formulae, should be used in the text. Greek letters or unusual signs should be written plainly or explained by marginal notes. Superscripts and subscripts must be legible and carefully placed. Manuscripts should be carefully checked before being submitted, to reduce the need for changes after the type has been set. If authors require changes to be made after the type is set, they will be charged for changes that are considered to be excessive. **All pages, whether text, figures, or tables, should be numbered.**

**ABSTRACT:**—An abstract of not more than about 200 words, indicating the scope of the work and the principal findings, is required.

#### ILLUSTRATIONS:

(i) **Line Drawings:**—All lines should be of sufficient thickness to reproduce well. Drawings should be carefully made with India ink on white drawing paper, blue tracing linen, or co-ordinate paper **ruled in blue only**; any co-ordinate lines that are to appear in the reproduction should be ruled in black ink. Paper ruled in **green, yellow, or red should not be used** unless it is desired to have all the co-ordinate lines show. Lettering and numerals should be neatly done in India ink preferably with a stencil (**do not use typewriting**) and be of such size that they will be legible and not less than one millimeter in height when reproduced in a cut three inches wide. All experimental points should be carefully drawn with instruments. Illustrations need not be more than two or three times the size of the desired reproduction, but the ratio of height to width should conform with that of the type page. **The original drawings and one set of small but clear photographic copies are to be submitted.**

(ii) **Photographs:**—Prints should be made on glossy paper, with strong contrasts; they should be trimmed to remove all extraneous material so that essential features only are shown. Photographs should be submitted **in duplicate**; if they are to be reproduced in groups, one set should be so arranged and mounted on cardboard with rubber cement; the duplicate set should be unmounted.

(iii) **General:**—**The author's name, title of paper, and figure number should be written in the lower left-hand corner (outside the illustration proper) of the sheets on which the illustrations appear.** Captions should not be written on the illustrations, but typed on a separate page of the manuscript. All figures (including each figure of the plates) should be numbered consecutively from 1 up (arabic numerals). **Each figure should be referred to in the text.** If authors desire to alter a cut, they will be charged for the new cut.

**TABLES:**—Titles should be given for all tables, which should be numbered in Roman numerals. Column heads should be brief and textual matter in tables confined to a minimum. **Each table should be referred to in the text.**

**REFERENCES:**—**These should be listed alphabetically by authors' names, numbered in that order, and placed at the end of the paper.** The form of literature citation should be that used in the respective sections of this Journal. **Titles of papers should not be given in references listed in Sections A, B, E, and F, but must be given in references listed in Sections C and D.** The first page only of the references cited in papers appearing in Sections A, B, and E should be given. **All citations should be checked with the original articles.** Each citation should be referred to in the text by means of the key number; in Sections C and D the author's name and the date of publication may be included with the key number if desired.

The *Canadian Journal of Research* conforms in general with the practice outlined of the *Canadian Government Editorial Style Manual*, published by the Department in Public Printing and Stationery, Ottawa.

### Reprints

Fifty reprints of each paper without covers are supplied free. Additional reprints, if required, will be supplied according to a prescribed schedule of charges. On request, covers can be furnished at cost.





